

# **Studies on graphene based nanocomposites for biosensing applications**

**Thesis submitted to the Delhi Technological University  
for the award of the Degree of**

## **DOCTOR OF PHILOSOPHY**

**By**

**Owais Jalil  
(2K16/Ph.D/AC/07)**



**DEPARTMENT OF APPLIED CHEMISTRY  
DELHI TECHNOLOGICAL UNIVERSITY  
BAWANA ROAD, DELHI-110042  
INDIA**

**JULY 2022**

**Copyright ©Delhi Technological University-2022  
All rights reserved.**

**JULY 2022**

# **Studies on graphene based nanocomposites for biosensing applications**

**Thesis submitted to the Delhi Technological University  
for the award of the Degree of**

## **DOCTOR OF PHILOSOPHY**

**By**

**Owais Jalil  
(2K16/Ph.D/AC/07)**



**DEPARTMENT OF APPLIED CHEMISTRY  
DELHI TECHNOLOGICAL UNIVERSITY  
BAWANA ROAD, DELHI-110042  
INDIA**

**JULY 2022**

*Dedicated*  
*To*  
*My Parents*

**JULY 2022**



## **DECLARATION**

I state that this Ph.D thesis titled “**Studies on graphene based nanocomposites for biosensing applications**” was completed by me for the award of degree of Doctor of Philosophy under the supervision of Prof. D.Kumar, Department of Applied Chemistry, Delhi Technological University and Dr. Chandra Mouli Pandey, SGT University, Gurugram, Haryana.

This thesis presents the results of my original research work. Every effort has been made to clearly indicate any contributions made by others with proper citation.

No degree or diploma has ever been awarded to me from this or any other University for the present thesis which I am submitting to the Delhi Technological University.

Place: Delhi

**Owais Jalil**

Date:

Delhi Technological University

## **CERTIFICATE**

This is to certify that the thesis entitled “**Studies on graphene based nanocomposites for biosensing applications**” submitted by **Mr. Owais Jalil** to **Delhi Technological University**, for the award of the degree of “Doctor of Philosophy” is a record of the work carried out by him. Mr. Owais Jalil has worked under our guidance and has fulfilled the requirements for the submission of this thesis.

The results embodied in this thesis have not been submitted to any other university or institute for the award of any degree or diploma as per our knowledge and belief.

**Prof. D. Kumar**  
Professor  
Department of Applied Chemistry  
Delhi Technological University  
Bawana Road, Delhi-110042

**Dr. C.M. Pandey**  
Assistant Professor  
Department of Chemistry  
SGT University Gurugram,  
Haryana- 122505

**Prof. S G Warkar**  
Head, Department of Applied Chemistry  
Delhi Technological University  
Bawana Road, Delhi-110042

## ACKNOWLEDGEMENT

*At the outset, I would like to extend my profound sense of gratitude, indebtedness, and reverence to my supervisors, **Prof. (Dr.) D.Kumar**, Department of Applied Chemistry, Delhi Technological University, Delhi, and **Dr. C. M. Pandey** Assistant Professor for their guidance, constant inspiration, and invaluable suggestions for carrying out this work. Working under kind, motivated, and respected supervisors have been a matter of privilege. Their unwavering support, frequent assistance, and thorough monitoring during the research studies helped me to reach another milestone in my academic career.*

*I wish to convey my sincere thanks to **Dr. P.K Roy** (Scientist F, DRDO), for his constant support and inspiration. I express my sincere gratitude to **Prof. Ram Singh** (Applied Chemistry, DTU) for allowing me to carry out electrochemistry work in his lab and providing the necessary facilities.*

*I would like to express my profound gratitude to **Prof. S G Warker**, Head, Department of Applied Chemistry, Delhi Technological University for helping me during the entire duration of my Ph.D.*

*I also convey my sincere thanks to **Dr. Inamuddin** (Assistant Professor, AMU) and **Mr. Bhim Singh Chandel** (Lecturer, DSEU) for their active support.*

*I was lucky to have a great work atmosphere in the laboratory, which aided my task properly. I must thank **Sakshi Verma** and **Deeksha Thakur** for their constant help in every possible way to carry forward my research work. It gives me a great pleasure to offer my heartfelt gratitude to all of the **faculty members** of the **Department of Applied Chemistry**, DTU for their cooperation and timely help. I am also appreciative of **technical and non-technical staff** for their prompt help and cooperation when needed. I am grateful to my dear former and current labmates for their assistance in completing my research,*

*Dr. AV Ullas, Dr. Nahid Iqbal, Saroj Paneru, Sweety, Divya, and Tanushree. I want to thank my dear friends for their wonderful company and helpful assistance, **Anurag Kaushik, Aamir Khan, Rehan Ghazi, Amrendra Mishra, Himansh Goel, Azeem, and Arsalan.** I want to extend my gratitude to my critics, particularly the **reviewers** who unknowingly assisted in my development as a better researcher.*

*Finally, I want to thank my **family** for their encouragement and support throughout my Ph.D. tenure. I convey my heartfelt thanks and affection to my father, **Mr. Jalil Ahmad Khan,** and mother, **Mrs. Yasmeen Jalil,** for their unending love and encouragement throughout my life. I am grateful to my sister **Sameera** for her helpful advice, care, love, and belief in me throughout my life. I'm also grateful to my wonderful, loving nieces **Manaal, Hania, and Ifra** for their constant encouragement.*

*Owais Jalil*

## **ABSTRACT**

The research work reported in this thesis speaks about the design of a biosensor which provides quantitative information by utilizing a biological recognition element/ biochemical receptor in direct spatial contact with a transducer. As we know that the biosensors are made up of two main parts, namely, the bio-element as well as the sensing element. An enzyme, antibody, DNA, or other bio-element can be used for the detection of a specific analyte. While the transducer section turns the biological signal into an observable electrical signal. Biosensors used in clinical diagnostic and therapeutic applications have a lot of room for innovations employing many multi-disciplinary aspects of science and technology. Recently, a new generation biosensor is designed to assist in combining biological molecules with biocompatible nanotechnology conducting frameworks.

The massive expansion in the world's population and rise in habits increases the risk of developing cancer which has long been regarded as the leading cause of death globally. The number of new cases of cancer rapidly increases day by day. The cell development mechanism in a healthy adult is a steady, consistent process that keeps the ideal amount of cells in a different part of the tissue. However, the cells abnormally divide and expand out of control, leading to the development of cancer, which emerges in most of the cases as a swelling mass known as a malignant tumor. Benign tumors, such as moles and warts, are typically not hazardous/ harmful. Further, in case of malignant tumor, the cells invade neighboring tissue through blood arteries and delivered to nearby organs. They divide and develop again in this region, ultimately producing a new tumor in the affected organ. Metastasis is the process by which cancer spreads to the multiple body organs. Cancer sufferer death rates in poor nations are most likely due to both delayed diagnosis and restricted access to early and conventional treatment. Conventional detection approaches,

such as radiography and physical testing, have been observed to take many hours or, in some circumstances, few weeks to produce the conclusions. However, these traditional procedures are highly expensive, require specialized apparatus, take a long time, and are less sensitive. As a result, there is an urgent need to develop reliable, sensitive, specific, fast, and user-friendly devices for detecting the cancer biomarkers. As a result, the efforts have been made on expanding portable biosensors with relatively high sensitivity and specificity.

Graphene oxide (GO) has recently attracted much attention in biosensor applications. This is owing to its distinct electrical features, high surface area, superior conductivity, excellent charge transfer capability, flexibility of functionalization, and biocompatibility. Furthermore, due to its high electrocatalytic activity, and potential to exhibit direct electron transfer property for particular protein, GO has been actively investigated as a sensitive platform in electrochemical biosensors. The incorporation of nanomaterials such as metal oxides and metal sulfides has sparked considerable attention due to the possibility of tailoring the specific features of each component into a single material. Additional synergistic effects of these materials have influenced the biosensor performance, resulting in the better sensitivity and selectivity. Thus, the present study focuses on the synthesis, characterization, and use of rGO, rGO nanocomposites with  $\text{TiO}_2$  and  $\text{MoS}_2$ , in the development of efficient electrochemical biosensors for the sensitive and selective detection of cancer biomarker (EpCAM). A thin coating of rGO and its nanocomposites was electrophoretically deposited over the ITO coated glass electrode and metallic ions and anti-biomarkers were coupled via the functional groups in GO (-OH and -COOH). Thus, a biosensor with better performance for detecting the cancer biomarkers (EpCAM) in buffer and spiked human serum samples has been designed and found fit and promising for biosensing applications.

# CONTENTS

DECLARATION.....	i
CERTIFICATE.....	ii
ACKNOWLEDGEMENT.....	iii
ABSTRACT.....	v
CONTENTS.....	vii
LIST OF FIGURES.....	x
LIST OF TABLES.....	xv
ABBREVIATIONS.....	xvi

## **1. Introduction & Literature Review**

1.1. Introduction to graphene.....	1
1.2. Derivatives of graphene.....	2
1.2.1. Graphane (hydrogenated graphene).....	2
1.2.2. Fluorographene (fluorinated graphene).....	3
1.2.3. Graph-yne and graph-diyne.....	3
1.2.4. Graphene oxide (oxidized graphene).....	4
1.2.5. Reduced graphene oxide.....	5
1.3. Synthesis of graphene.....	6
1.3.1. Pyrolysis.....	9
1.3.2. Chemical vapour deposition (CVD).....	9
1.3.3. Epitaxial growth on metal.....	10
1.3.4. Liquid-phase exfoliation (LPE).....	12
1.3.5. Wet chemical synthesis.....	12
1.3.6. Micromechanical exfoliation.....	14
1.3.7. Electrochemical synthesis.....	15
1.4. Synthesis of graphene derivatives.....	15
1.4.1. Chemical vapor deposition (CVD).....	16
1.4.2. Arc discharge.....	17
1.4.3. Epitaxial growth (EG).....	18
1.5. Reduction of graphene oxide.....	18
1.6. Graphene based nanocomposite.....	19
1.6.1. Graphene based polymer nanocomposite.....	19
1.6.2. Graphene-metal nanocomposite.....	20
1.6.3. Graphene based hybrid composites.....	21
1.7. Application of graphene.....	22
1.7.1. Energy storage.....	22
1.7.2. Membrane.....	22
1.7.3. Graphene composites at low-temperature environments.....	23
1.7.4. Miscellaneous applications.....	23
1.7.5. Physical sensors.....	24
1.7.6. Biomedical applications of graphene oxide.....	24
1.8. Graphene oxide for biosensing applications.....	25
1.8.1. Biosensors.....	25
1.8.2. Components of a biosensor.....	26
1.8.2.1. Biomolecular recognition elements in biosensors.....	26

1.8.2.2.	Immobilization matrices .....	26
1.8.2.3.	Transducer.....	27
1.9.	Cancer .....	28
1.9.1.	Diagnostic evaluation of cancer.....	30
1.9.1.1.	Imaging test .....	30
1.9.1.2.	Biopsy.....	30
1.9.1.3.	Lab-based test.....	31
1.9.2.	Cancer biomarkers.....	31
1.9.3.	Biosensor for cancer biomarker detection .....	32
1.9.3.1.	Electrochemical immunosensor .....	33
1.9.3.2.	Antibodies .....	34
1.9.3.3.	Graphene oxide for immobilization of antibodies .....	34
1.10.	Research objective .....	35
1.11.	Thesis organization .....	35
1.12.	References .....	39
<b>2. Materials &amp; Experimental Techniques</b>		
2.1.	Introduction.....	52
2.2.	Materials .....	52
2.2.1.	Chemicals.....	52
2.2.2.	Buffers and solutions .....	53
2.3.	Characterization techniques.....	53
2.3.1.	Fourier Transform Infrared (FT-IR) spectroscopy.....	53
2.3.2.	Raman spectroscopy .....	56
2.3.3.	Ultraviolet-Visible (UV-Vis) spectroscopy .....	57
2.3.4.	Thermogravimetric analysis (TGA).....	58
2.3.5.	Differential Scanning Calorimetry (DSC).....	60
2.3.6.	X-ray diffraction (XRD).....	60
2.3.7.	Scanning Electron Microscopy (SEM) .....	62
2.3.8.	Transmission Electron Microscopy (TEM) .....	63
2.3.9.	Zeta potential .....	65
2.3.10.	Electrochemical techniques .....	66
2.3.10.1.	Cyclic Voltammetric (CV) measurements .....	67
2.3.10.2.	Differential Pulse Voltammetry (DPV) .....	68
2.3.10.3.	Electrochemical Impedance Spectroscopic (EIS) .....	68
2.4.	Methods to immobilize antibodies to the GO-based matrix.....	69
2.4.1.	Covalent immobilization .....	69
2.5.	Protocols to estimate various parameters relating to the performance of rGO nanocomposites based Immuno-biosensor.....	70
2.5.1.	Diffusion coefficient and electron transfer rate constant .....	70
2.5.2.	Linear Range, Sensitivity, and Detection Limit .....	70
2.5.3.	Shelf-Life and reproducibility of the bioelectrodes .....	70
2.6.	References .....	72
<b>3. Nanostructured titanium oxide decorated graphene oxide-based electrochemical biosensor for cancer biomarker detection</b>		
3.1.	Introduction.....	74
3.2.	Experimental section .....	74
3.2.1.	Synthesis of GO and TiO <sub>2</sub> nanoparticles.....	74
3.2.2.	Synthesis of rGO@TiO <sub>2</sub> nanocomposite .....	75



3.2.3. Electrophoretic deposition (EPD) of rGO and rGO@TiO <sub>2</sub> nanocomposite.....	76
3.2.4. Fabrication of rGO/ITO and rGO@TiO <sub>2</sub> /ITO based immunosensor .....	76
3.3. Results and discussion.....	77
3.3.1. Structural, morphological and elemental studies .....	77
3.3.2. Electrochemical characterization .....	80
3.3.3. Optimization studies .....	83
3.3.4. Electrochemical biosensing studies.....	84
3.3.5. Electrode studies .....	86
3.3.6. Specificity and serum sample analysis .....	87
3.3.7. Stability and regeneration .....	88
3.4. Conclusions .....	89
3.5. References .....	91
<b>4. Molybdenum disulfide grafted reduced graphene oxide nanohybrid based electrochemical biosensor for cancer biomarker detection</b>	
4.1. Introduction.....	93
4.2. Experimental section.....	93
4.2.1. Synthesis of GO and rGO.....	93
4.2.2. Synthesis, and functionalization of MoS <sub>2</sub> @rGO nanohybrid.....	93
4.2.3. Electrophoretic deposition of MoS <sub>2</sub> @rGO nanohybrid and biosensor fabrication.....	94
4.3. Results and discussion.....	96
4.3.1. Characterization of MoS <sub>2</sub> @rGO nanohybrid.....	96
4.3.2. Microscopic studies.....	97
4.3.3. Electrochemical characterization.....	99
4.3.4. Optimization of biosensing parameters for efficient bioelectrode response.....	101
4.3.5. Electrochemical response studies.....	102
4.3.6. Selectivity, reusability and shelf life studies of the biosensor.....	104
4.3.7. Validation of biosensor with human serum samples.....	105
4.3.8. Reusability and shelf-life.....	106
4.4. Conclusions.....	107
4.5. References.....	108
<b>5. Development of electrochemical biosensors based on TiO<sub>2</sub>/rGO@MoS<sub>2</sub> nanocomposite</b>	
5.1. Introduction.....	110
5.2. Experimental section.....	110
5.2.1. Synthesis, of TiO <sub>2</sub> /MoS <sub>2</sub> @GO nanohybrid.....	110
5.2.2. Fabrication of the bioelectrode .....	111
5.3. Results and discussion.....	112
5.3.1. Characterization of hybrid nanocomposite.....	112
5.3.2. Electrochemical characterization of fabricated electrodes.....	115
5.3.2.1. Electrochemical biosensing response of EpCAM using electrode.....	117
5.3.3. Interference, and shelf-life studies.....	117
5.3.4. Real sample analysis.....	118
5.4. Conclusion.....	119
5.5. References.....	120
<b>6. Conclusions and future prospects .....</b>	<b>122</b>

## List of Figures

**Figure 1.1** The honeycomb structure of the graphene monolayer

**Figure 1.2** Acetylic linkage in graph-yne and graph-diyne

**Figure 1.3** Conversion of GO to rGO

**Figure 1.4** Graphene synthesis approaches

**Figure 1.5** Graphene layer growth on a metal surface

**Figure 1.6** Various components of a biosensor

**Figure 2.1** (a) Schematic of the optical layout of Michelson Interferometer, (b) FTIR spectra of (i) rGO@CP electrode (ii) rGO-TiO<sub>2</sub>@CP electrode.

**Figure 2.2** (a) Schematic representation of Raman spectroscopy (b) Raman spectra of GO

**Figure 2.3.** (a) Schematic of dual-beam UV-Vis spectrophotometer. (b) UV -Vis spectra of rGO-MoS<sub>2</sub>

**Figure 2.4** (a) Schematic representation of thermogravimetric analysis (TGA) (b) TGA thermogram of (i) PEDOT:PSS,(ii) PEDOT:PSS/rGO nanohybrid, (iii) PEDOT:PSS/rGO@TiO<sub>2</sub> nanohybrid.

**Figure 2.5** (a) Schematic working of the DSC apparatus. (b) DSC thermogram of GO

**Figure 2.6** (a)Schematic representation of XRD (b) XRD spectra of GO, rGO, rGO/TiO<sub>2</sub>

**Figure 2.7** (a) Schematic representation of scanning electron microscope (b) SEM image of rGO/TiO<sub>2</sub>/MoS<sub>2</sub>.

**Figure 2.8** (a) A pictorial view of scanning electron microscope (b) TEM image of rGO

**Figure 2.9** (a) Schematic of Zeta potential (b) Zeta potential plot of rGO:TiO<sub>2</sub>:MoS<sub>2</sub> composite

**Figure 2.10** (a) Working scheme of potentiostat (b) Scan rate (10-100 mV/s) studies of GO in PBS (100 mM, pH 7.0, 0.9% NaCl) containing 5 mM [Fe(CN)<sub>6</sub>]<sup>3-/4-</sup>.

**Figure 3.1** Schematic illustration for the (A) synthesis and electrophoretic deposition of rGO@TiO<sub>2</sub> onto the ITO-coated electrode and (B) subsequent biosensor fabrication.

**Figure 3.2.** (A) X-ray diffraction patterns of (i) rGO (ii) rGO@TiO<sub>2</sub> nanocomposite, (iii) GO (inset) (B) XRD spectra of TiO<sub>2</sub> nanoparticles (C) TGA curve for (i) GO (ii) rGO (iii) rGO@TiO<sub>2</sub> nanocomposite (iv) TiO<sub>2</sub> nanoparticles (v) graphite in the temperature range of 25 to 900 °C at 10 °C/min heating rate in a nitrogen environment (D) FTIR spectra of (i) rGO@TiO<sub>2</sub> nanocomposite and (ii) GO in the frequency region of 500 - 4000 cm<sup>-1</sup>.

**Figure 3.3** UV-visible spectra for (A) GO and (B) rGO.

**Figure 3.4** TEM micrographs of (A) GO and (B) rGO@TiO<sub>2</sub> nanocomposite. SEM micrographs of (C) rGO/ITO electrode (D) TiO<sub>2</sub>/ITO electrode (E) rGO@TiO<sub>2</sub>/ITO electrode and (F) anti-EPCAM/ rGO@TiO<sub>2</sub>/ITO electrode.

**Figure 3.5** (A) Nyquist plot for the Faradic impedance for (i) rGO@TiO<sub>2</sub>/ITO (ii) rGO/ITO (iii) anti-EPCAM/ rGO@TiO<sub>2</sub>/ITO electrode, and (iv) EpCAM immobilized on anti-EPCAM/ rGO@TiO<sub>2</sub>/ITO electrode data in PBS solution (pH 7.4) containing 5 mM [Fe(CN)<sub>6</sub>]<sup>3-/4-</sup>, in the frequency range from 10<sup>6</sup> to 10<sup>-2</sup> Hz. Cyclic voltammetric analysis showing the variation of (B) potential with log of scan rate and (C) current with (scan rate)<sup>1/2</sup> from 10-300 mV in case of (i) rGO@TiO<sub>2</sub>/ITO and (ii) rGO/ITO electrode.

**Figure 3.6** (A) Optimization of the antibody concentration (10 to 70 µg•mL<sup>-1</sup>) after immobilization on rGO@TiO<sub>2</sub>/ITO electrodes and (B) Incubation time study of anti-EpCAM/rGO@TiO<sub>2</sub>/ITO electrode. Error bars: SD, n = 3

**Figure 3.7** DPV electrochemical response of (A) anti-EpCAM/rGO@TiO<sub>2</sub>/ITO electrode against EpCAM concentration; the magnified view of oxidation peak current is also shown in the inset, (B) linearity plot with variation in the concentration of EpCAM (0.01-60 ng mL<sup>-1</sup>) (C) control experiment showing the DPV response of (i) anti-EpCAM/rGO@TiO<sub>2</sub>

electrode (ii) rGO@TiO<sub>2</sub>/ITO electrode as a function of EpCAM. (D) Specificity of anti-EpCAM/rGO@TiO<sub>2</sub>/ITO biosensor with IgG proteins and glucose as control. The potential was scanned from -0.4 to 0.8 V with amplitude of 50 mV in PBS solution containing 5 mM [Fe(CN)<sub>6</sub>]<sup>3-/4-</sup> at pH 7. Error bars: SD, n = 3

**Figure 3.8** DPV electrochemical peak response of (i) ITO electrode (ii) anti-EpCAM/rGO@TiO<sub>2</sub>/ITO (iii) rGO/ITO and (iv) rGO@TiO<sub>2</sub>/ITO electrode. The potential sweeping taken from -0.4 to 0.8 V with 50 mV amplitude in PBS solution containing 5 mM [Fe(CN)<sub>6</sub>]<sup>3-/4-</sup> at pH 7.

**Figure 3.9** (A) Investigation of biosensor stability using DPV technique by recording the current response to EpCAM every 5 days upto 35 days. (B) Regenerability of the biosensor for repeated detection of EpCAM over five cycles. Error bars: SD, n = 3

**Figure 4.1** Scheme for (A) MoS<sub>2</sub>@rGO nanohybrid synthesis (B) fabrication of rGO@MoS<sub>2</sub>/ITO based biosensor. (C) XRD curves of (i) MoS<sub>2</sub>, (ii) rGO (iii) MoS<sub>2</sub>@rGO nanohybrid. (D) FTIR spectra of (i) rGO and (ii) MoS<sub>2</sub>@rGO nanohybrid.

**Figure 4.2** (A) FTIR spectra of GO and (B) TGA curve for MoS<sub>2</sub>@rGO nanohybrid.

**Figure 4.3** (A) TEM image of rGO and (B) SEM image of rGO/ITO electrode

**Figure 4.4** TEM micrograph of (A & B) MoS<sub>2</sub>@rGO nanohybrid and SEM micrograph of (C) MoS<sub>2</sub>@rGO/ITO electrode, and (D) anti-EpCAM/ MoS<sub>2</sub>@rGO/ITO electrode.

**Figure 4.5** (A) EIS data of (i) MoS<sub>2</sub>@rGO/ITO (ii) anti-EpCAM/MoS<sub>2</sub>@rGO/ITO (iii) rGO/ITO and (iv) EpCAM treated anti-EpCAM/MoS<sub>2</sub>@rGO/ITO (B) Cyclic voltamogram of MoS<sub>2</sub>@rGO/ITO electrode with scan rate (10-300 mV). Plots of (C) I<sub>pa</sub>, I<sub>pc</sub>, against square root of scan rate and (D) potential against log of scan rate for MoS<sub>2</sub>@rGO/ITO electrode.

**Figure 4.6** Optimization of the (A) anti-EpCAM (10 to 80  $\mu\text{g mL}^{-1}$ ) concentration, (B) incubation time of EpCAM and (C) pH condition for efficient detection of EpCAM.

**Figure 4.7** DPV studies response of (A) anti-EpCAM/MoS<sub>2</sub>@rGO/ITO as a function of EpCAM concentration; inset is the magnified view of oxidation peak current, (B) Calibration plot between the magnitudes of current recorded and EpCAM concentration (0.001-20  $\text{ng mL}^{-1}$ ). (C) Specificity studies of the fabricated biosensor with (i) EpCAM (ii) glucose (iii) NaCl, (iv) IgG (v) EpCAM+other interferents (D) Electrochemical response of the biosensor in (i) buffer sample and (ii) spiked human serum sample

**Figure 4.8** (A) Regeneration studies of the biosensor for EpCAM detection (B) Variation of anti-EpCAM/MoS<sub>2</sub>@rGO/ITO electrode response towards EpCAM over a period of 55 days.

**Figure 5.1** Scheme showing the synthesis and fabrication of TiO<sub>2</sub>/MoS<sub>2</sub>@GO nanohybrid-based biosensor for cancer biomarker detection

**Figure 5.2** (A) XRD pattern of TiO<sub>2</sub>/MoS<sub>2</sub>@GO nanohybrid, (B) Raman spectra of (i) rGO (ii) TiO<sub>2</sub>/MoS<sub>2</sub>@GO nanohybrid, (C) TGA plot for (i) TiO<sub>2</sub>/MoS<sub>2</sub>@GO nanohybrid and (ii) MoS<sub>2</sub>@GO nanohybrid; (D) FTIR spectra of TiO<sub>2</sub>/MoS<sub>2</sub>@GO nanohybrid.

**Figure 5.3** SEM image of (A) MoS<sub>2</sub>@GO nanohybrid; (B) TiO<sub>2</sub>/MoS<sub>2</sub>@GO nanohybrid; (C) EDX of TiO<sub>2</sub>/MoS<sub>2</sub>@GO nanohybrid. SEM image of (D) TiO<sub>2</sub>/MoS<sub>2</sub>@GO/ITO electrode and (E) anti-EpCAM/TiO<sub>2</sub>/MoS<sub>2</sub>@GO/ITO electrode.

**Figure 5.4** (A)  $I_{pa}$ ,  $I_{pc}$ , vs. square root of scan rate plot of (i) TiO<sub>2</sub>/MoS<sub>2</sub>@GO/ITO and (ii) anti-EpCAM/TiO<sub>2</sub>/MoS<sub>2</sub>@GO/ITO electrode (B) Plot of potential with log of scan rate for (i) TiO<sub>2</sub>/MoS<sub>2</sub>@GO/ITO and (ii) anti-EpCAM/TiO<sub>2</sub>/MoS<sub>2</sub>@GO/ITO electrode. (C) DPV studies response of the anti-EpCAM/TiO<sub>2</sub>/MoS<sub>2</sub>@GO/ITO electrode against EpCAM concentration; The magnified view of oxidation peak current is given in inset (D) Calibration plot between the current magnitudes and EpCAM concentration (0.0001-20  $\text{ng mL}^{-1}$ ).

**Figure 5.5** (A) Interference study of the fabricated biosensor (B) Bar graph showing the stability of the biosensors (C) Performance of the biosensor with different concentration of EpCAM spiked serum samples

## **List of Tables**

**Table 1.1** Graphene conformer's physical properties

**Table 3.1** Comparison data showing the anodic peak current obtained for EpCAM antigen concentration in standard and spiked serum samples using anti-EpCAM/rGO@TiO<sub>2</sub>/ITO electrode

**Table 4.1** Recoveries of EpCAM spiked to different samples.

**Table 4.2** Different EpCAM concentrations data found in spiked serum samples

## ABBREVIATIONS

GO	Graphene oxide
EpCAM	Epithelial Cell Adhesion Molecule
CV	Cyclic Voltammetry
EIS	Electrochemical Impedance Spectroscopy
DPV	Differential Pulse Voltammetry
TGA	Thermogravimetric Analysis
DSC	Differential Scanning Calorimetry
EDC	N-ethyl-N'-(3-dimethyl aminopropyl) carbodiimide
NHS	N-hydroxysuccinimide
BSA	Bovine Serum Albumin
PBS	Phosphate Buffer Saline
ITO	Indium Tin Oxide
L-cys	L-cysteine
EPD	Electrophoretic Deposition
XRD	X-ray Diffraction
FT-IR	Fourier Transforms Infrared
TEM	Transmission Electron Microscopy
CPE	Constant Phase Element
RSD	Relative Standard Deviation
SEM	Scanning Electron Microscopy
EDAX	Energy Dispersive x-ray Spectroscopy
FESEM	Field Emission Scanning Electron Microscopy



### 1.1 Introduction to graphene

Graphene was formally postulated in 1986, and some scientific papers on graphene and graphene-like materials have been published [1]. In 2010, Professors Andre Geim and Konstantin Novoselov have got Nobel prize for the discovery of the exfoliation method and an associated investigation of the electronic properties of graphene [2]. Graphene is a zero band gap semiconductor with a tiny overlap between conduction and valence band and it has remarkably high electron mobility of  $200,000 \text{ cm}^2 \text{ V}^{-1} \text{ s}^{-1}$  at room temperature. The  $sp^2$  hybridization is shown by two dimensional (2D) honeycomb network of graphene [3] which is made up of carbon atoms as given in Fig. 1. The 2D graphene is light weight and has excellent electrical, optical and mechanical properties. Due to these extraordinary properties, graphene has been used on large scale for storage, electronic gadgets, catalysis of reactions, and in the fabrication of different types of sensors [4] etc.

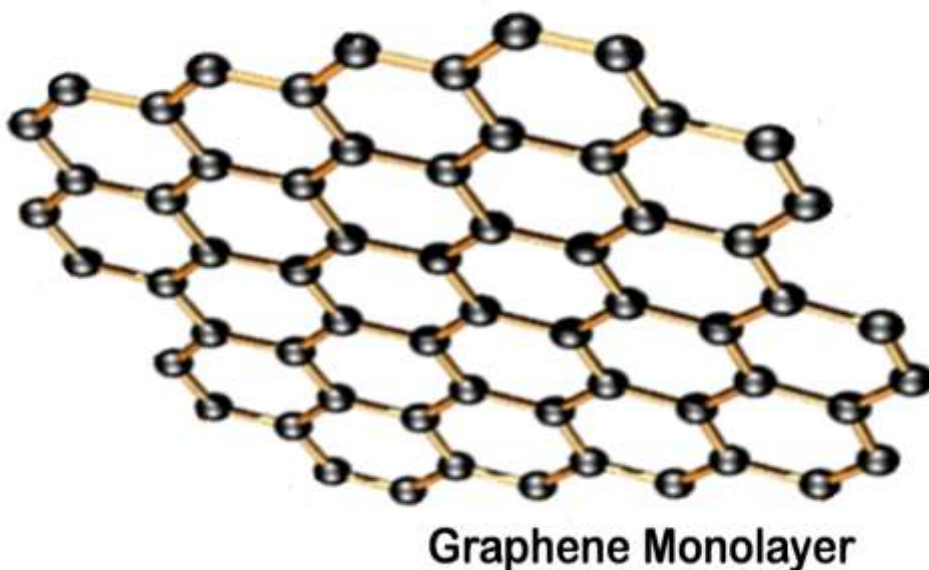


**Figure 1.1** The honeycomb structure of the graphene monolayer

The studies on catalytic properties of graphene and functionalized graphene based nanocomposites are lying on the graphene extended honeycomb network [5]. Graphite is made up of 41 monolayers of graphene spaced between each of them is  $0.3 \times 10^{-9}$  m and bound together by weak attraction (Van der Waals forces). Each carbon atom forming 3 sigma bonds with nearest neighbouring carbon and fourth electron is aligned perpendicular to the monolayer of nonbonding  $2p_z$  orbital makes a conducting sigma bond in the network [6]. Recently, a lot of research work has been carried out to modify the structure of graphene with desired chemical, optical and electrical properties. Graphene based material rises enormous interest by its modifying properties brought by its incorporating different functional groups that lead to its hydrophilicity and facile modification [7].

## **1.2. Derivatives of graphene**

Hydrogenated, fluorinated, and oxidized graphene derivatives, known as graphane, fluorographene, and graphene oxide, are predicted to exhibit fascinating characteristics [8]. Furthermore, the insertion of either acetylenic or diacetylene chains between carbon hexagons produces a single-atom thick layer that has intriguing characteristics like graphene; on preliminary stage named as graphyne and finally called graphdiyne [9].

### **1.2.1. Graphane (hydrogenated graphene)**

The main active element for hydrogenated graphane derivative is CH. It is referred to as graphane which has  $sp^3$  C–C, i.e., sigma bond (saturated) while in graphene C=C, i.e., unsaturated, due to this saturation graphane is tensed [10]. The forms of graphane have been reported, i.e., a “boat-like” and “chair-like” conformer with hydrogen atoms alternating in pairs and with hydrogen atoms alternating on both sides of the carbon atom layer, respectively [11]. The two bond lengths of C–C in boat-type conformer are  $1.52 \times 10^{-10}$  m and  $1.56 \times 10^{-10}$  m, the former corresponds to two covalently bound to hydrogen atoms on opposite ends, while the latter corresponds to those covalently attached to hydrogen atoms along the same side, which are slightly longer than  $1.52 \times 10^{-10}$  m due to H–H repulsion. This predicted C–C bond length of  $1.52 \times 10^{-10}$  m in the chair-type conformer

has resembled diamond saturated bonding and is much higher than that in unsaturated bonding, i.e.,  $1.42 \times 10^{-10}$  m of graphene [12]. The measured binding energy for boat-type graphane is 6.50 eV per atom and 6.56 eV per atom for chair conformer as given in Table 1. This binding energy is considerably greater than that of calculated for other hydrocarbons like benzene and acetylene [13].

**Table 1.1: Graphene conformer's physical properties**

Types of Conformation	Bond length (nm)		Binding energy (eV per atom)
	C-H	C-C	
Boat-type	0.110	0.152 & 0.156	6.50
Chair-type	0.111	0.152	6.56

### 1.2.2. Fluorographene (fluorinated graphene)

Fluorographene has the general formula  $(CF)_n$  and  $(C_2F)_n$ , and it is commonly utilized in superhydrophobic and lithium primary battery materials. The geometry of the fluorographene chair type conformer is puckered. Half of the carbon atoms in  $C_2F$  make covalent bonds with carbon atoms in neighbouring layers, while the other half is covalently bound with fluorine [14]. The structure of completely fluorinated graphene is similar to graphene and it has a chair-like shape [15]. Because, fluorine atoms alternating in pairs on one side of the carbon atom layer generate high repulsion, the boat-type configuration is said to be difficult to develop in fluorographene [16].

### 1.2.3. Graph-yne and graph-diyne

The term graphyne derives from its chemical structure, in which acetylenic connections replace one-third of the carbon-carbon bonds in graphene [17]. The hexagons of carbon are bonded by carbon triple bond carbon ( $-C \equiv C-$ ) also called as acetylic linkage. While, the graph-diyne consists of two acetylenic chains sandwiched by carbon hexagons [18] as shown in Fig. 2.



**Figure 1.2** Acetylic linkage in graph-yne and graph-diyne

By assuming different amounts of acetylenic linkages, graphyne's conductivity was predicted to be significantly lower than grapheme [19]. The mechanical characteristics of the above two structures, grapheme like layers, including graphdiyne were investigated as a function of the number of ( $-C \equiv C-$ ) and different ( $-C \equiv C-$ ) configurations [20].

#### 1.2.4. Graphene oxide (oxidized graphene)

Graphene oxide (GO) is gaining a lot of attention because of its hydrophilicity and ease of modification arising due to the numerous oxygen containing groups [21]. The oxidized form of graphene is referred to as GO. It was discovered long before graphene and was originally produced in 1859 by oxidizing and exfoliating graphite. The  $sp^2$  structure of graphite layers are disturbed during the pre-treatment process, resulting in the formation of many distinct oxygens ( $-o-$ ) containing functional groups such as closed ring oxygen containing carbon (epoxy), acid (carboxyl), and alcoholic (hydroxyl) groups [22, 23]. The graphite interlayer distance increases by oxidation due to incorporation of  $-o-$  containing functional group mostly saturated closed ring. The exfoliation separates the graphite oxide layers, resulting in a solution of homogeneous GO layers. The hydroxy and epoxy groups of GO sheets are found in the basal plane of carbon, whereas at the margin, carboxy groups are present [24]. The chemical heterogeneity of GO sheets is greatly influenced by the amount of oxidation and temperature. A poor electrical conductivity of GO behaves either an insulator or a semi-conductive material depending on the oxidation level. GO sheets have around  $890 \text{ m}^2\text{g}^{-1}$  of specific surface area, with a Young's modulus of  $208 \pm 23 \text{ GPa}$  and fracture strength of around  $120 \text{ MPa}$ . Graphite oxides can have a broad range of chemical compositions, which depends mainly on the initial graphite and synthesis conditions. GO with well-controlled thickness and area has been the subject of several

investigations, as well as their reduction to produce graphene sheets.

### 1.2.5. Reduced graphene oxide

Reduced graphene oxide is a kind of graphene oxide obtained by the removal of oxygen containing groups to make the sheets comparable to pure graphene in terms of characteristics. The characteristics of the sheets vary depending on the degree of oxygen reduction; the more oxygen reduction, the closer it resembles to graphene than graphene oxide. The partially reduced form of GO is reduced graphene oxide (rGO) that has recovered  $\pi$  conjugated system. The structure of rGO resembles graphene with some residual oxygen and structural defects and the conductivity can be compared with the doped conductive polymers. Several techniques such as thermal annealing, chemical reduction, electrochemical and hydrothermal reduction have been reported for the conversion of GO to rGO and their structures are presented in the Fig. 3.

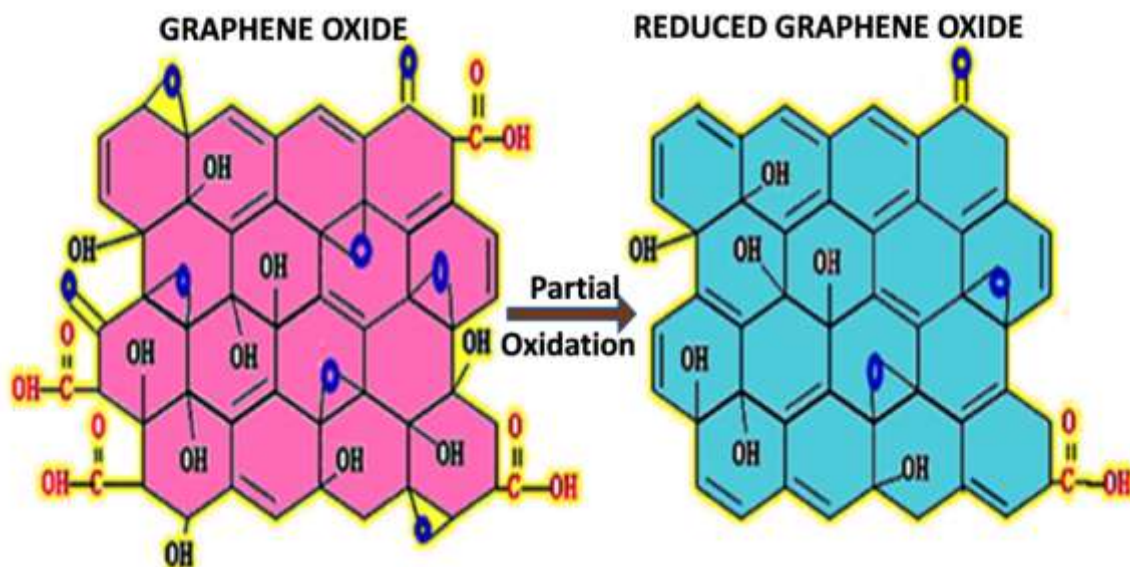


**Figure 1.3** Conversion of GO to rGO

For chemical reduction of GO reducing agents like sodium bromide (NaBr) or organic reducing agents like phenyl hydrazine hydrate or hydroxylamine are commonly employed. Thermal reduction happens at temperatures ranging from 300 to 2000°C in an inert or reducing environment. The different modifications are made by the removal of saturated oxygen functional group from the GO layer and the subsequent restoration of conjugation starts after the reduction [25]. The elevation in electrical conductivity and gain

in mobility are two most important impacts of the GO reduction procedure. During the reduction phase, the surface area of rGO rises as well. When we compare the mechanical strength of rGO sheets in respect of Young's modulus and breaking strength that is 1.0 TPA and 130 GPa, which is quite similar to graphene [26]. The precise process parameters utilized to reduce GO into rGO have a significant impact on the material's quality, influencing how near a structure to flawless graphene may be obtained. If graphene is to be used in massive applications such as biosensing, reduced graphene oxide might be a good choice since it is easier to make in large quantities than flawless single-layer or few-layer graphene. Graphene oxide can be reduced by treating with L-cysteine for 18 h @ 180 °C and hydrazine hydrate at 100 °C for 12 h [27]. Due to its exceptional capacities for interacting with biomolecules, reduced graphene oxide has been highlighted as a biosensing platform with specific benefits [28]. The fact that reduced graphene oxide can have a lot of functional groups makes it difficult to characterize it precisely, but this might be a benefit in some applications, especially biomedical ones because its functionalities can be readily adjusted to improve in an aqueous solution.

### **1.3. Synthesis of graphene**

The methods of synthesis for graphene derivatives are based upon desirable configuration and characteristics of material which includes shape, size and functionalization on the surface of graphene. The yield and quality of modified graphite products depends on how they are being synthesized [29]. Two approaches are generally been used for the synthesis of graphene, i.e., top-down and bottom-up techniques. Various techniques for the synthesis of graphene comes under these two major categories. Under top-down synthesis method, destruction approach is taken into account which leads to production of nano-sized sheets of graphene. Various methods like liquid-phase exfoliation, oxidative exfoliated reduction, mechanical exfoliation and arch discharge are being used for top-down synthesis. These methods are helpful in isolating layered graphite into mono, di, tri or multi-layer graphene. Top-down methods used for synthesis led to formation of better-quality graphene but the

quality of graphene synthesized by these methods depends on the precursor of graphite [30]. The top-down method is easier to develop extremely oxidized form of GO which on reduction not only provides better removed oxygen groups but also provides graphene like conducting material [31]. On the other hand, bottom-up synthesis approach finds challenges in industrial application. It refers to a technique in which graphene and its derivatives are synthesized by utilizing carbonaceous precursor having size in the range of an atom rather than graphite. The methods applied under this category are chemical vapor deposition, epitaxial growth, whole organic synthesis etc. However, bottom-up approaches leads to the formation of high-surface area but the major limitation is that it is quite expensive and requires advance operative arrangements [32]. In 1975, using platinum surface and applying breakdown technique, countable sheet of graphite was produced, until it is not summarized but it was not classified as graphene sheets owing to a limited characterization technique. One more reason to separate a single layer of graphite is a difficult task or may be a lack of importance of monolayer electrical properties.

Ruoff and colleagues attempted to separate tiny graphitic, highly oriented pyrolytic graphite flakes (HOPG) on silicon dioxide ( $\text{SiO}_2$ ) in the late 1990s [33]. Soon after the discovery of graphene in the year 2004, different ways for producing thin graphitic films and very few-layer graphene were explored [34]. Thin sheets of graphene,  $\text{MoS}_2$  (molybdenum disulfide),  $\text{NbSe}_2$  (Niobium diselenide), and BN (Boron nitride) were first separated in the years 2004 and 2005, providing experimental proof of 2D crystals [35]. Moreover, the graphene was initially produced as tiny sheets in order of a few microns with scotch tape by mechanical exfoliation of graphite to achieve the best quality graphene. Graphene has been synthesized using a variety of methods in recent years [36]. The most widely utilized techniques now are bottom-up like chemical vapor deposition, (CVD) and top-down (like mechanical and chemical exfoliation, wet chemical synthesis) as shown in Fig. 4. Unzipping nanotubes and microwave synthesis are two more methods that have been described. Furthermore, cantilever atomic force microscopy (AFM) was

used for mechanical exfoliation generating some layer graphene, with a thickness limitation of  $10 \times 10^{-9}$  to  $30 \times 10^{-9}$  m [37].

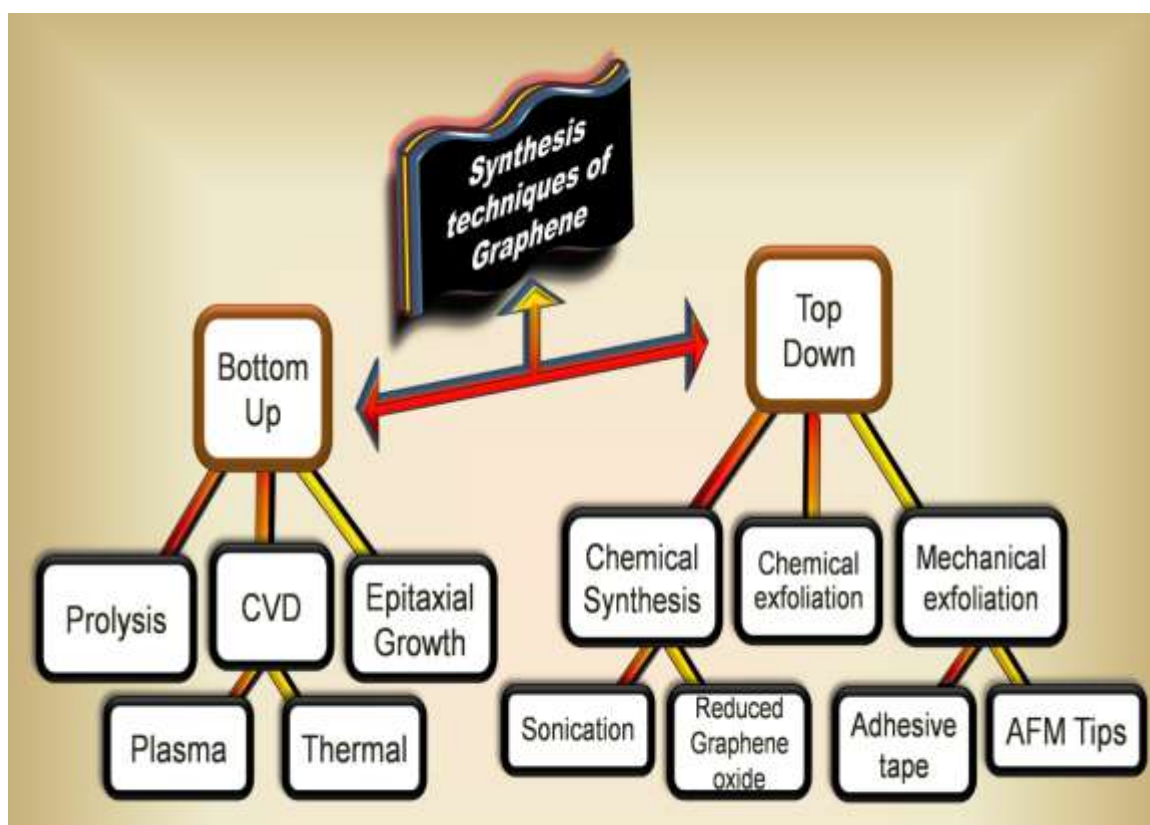


**Figure 1.4** Graphene synthesis approaches

The graphitic dispersed solution is separated by the addition of large basic ions between graphene sheets in a chemical exfoliation method. Chemical synthesis method involves the graphite oxide synthesis followed by its dispersion in a solution to reduce it by using hydrazine. For massive graphene manufacturing, catalytic thermal CVD has shown to be the most important technique, just as it did for carbon nanotube formation. As we know that all synthesis techniques have some disadvantages also that are dependent on the eventual use of graphene [38]. The mechanical exfoliation approach, for example, can produce monolayer to a very few graphenes, although the likelihood of getting a comparable structure using this method is negligible. Again, graphene made from rGO generally results in partial reduction of graphite oxide, which leads to a gradual debasement of electrical characteristics as the degree of reduction increases [39]. Thermal CVD techniques, on the other hand, are better for huge surface appliance manufacturing. Thermally graphitization of graphene on silicon carbide or metal surface is known as



epitaxial graphene [40]. The thermal CVD technique is unique as it produces a homogeneous sheet of graphene.

### **1.3.1. Pyrolysis**

The Greek word pyrolysis is composed of two words 'pyro' meaning heat and 'lysis' meaning separation. Few layered graphene can be synthesized simply on surface of metals. Most common techniques among such process can be performed by thermal disintegration of silicon carbide (SiC). Si usually isolates and leaves carbon in form of few sheets of graphene at high temperature. However, this method does not allow large scale production but allows continuous synthesis of graphene sheets on metal coated SiC surface [41]. Highly pure monolayer of graphene can also be prepared using thermal decomposition of ethane at 727°C.

### **1.3.2. Chemical vapour deposition (CVD)**

CVD method works by mixing molecules of gases (frequently in the form of carrier gases) in a vacuum chamber where the reaction takes place at room temperature. On the substratum surface, gases are mixed with the help of applying heat forming a monolayer onto the surface. After that, the undesired gases are pushed out through the exhaust. Low-pressure chemical vapor deposition (LPCVD) is a CVD technique performed at sub-atmospheric pressures. This low pressure aids in the prevention of undesired reactions and the production of a coating thickness on the substrate with more uniformity. Ultra-high vacuum chemical deposition (UHVCVD) is a CVD technique that takes place at extremely low atmospheric pressures, typically around  $10^{-6}$  Pa [42]. The pyrolytic breakdown of precursors necessitates extremely high temperatures needs the use of metal catalysts to lower down the reaction temperature. The second phase, which involves forming a carbon structure out of isolated carbon atoms, also necessitates a lot of heat (about 2000°C without a catalyst), thus a catalyst is required at this point to lower the temperature required for a reaction to roughly 1000°C [43]. To produce monolayer graphene on a substrate, scientists must first solve the most significant problems with

current techniques [44]. The first important issue is that, while CVD can generate high-quality graphene on a substrate, effective separation or peeling of graphene from the substrate has proven to be a challenge. The reason for this is that the connection between graphene and the substrate on which it is grown is yet not known, making separation difficult without altering the graphene's structure or changing the material's characteristics. Depending on the type of substrate utilized, several approaches are used to accomplish this separation. The production of CVD graphene on a copper (Cu) surface is one approach that has been investigated (Cu is used as a catalyst) [45]. A reaction occurs between both the copper substrate and the graphene throughout CVD, causing a high amount of hydrostatic compression thus binding the graphene to the substrate. Scientists are also investigating the use of poly(methyl methacrylate) (PMMA) as a support polymer to aid graphene transfer to a different substrate [46]. This process involves coating graphene with PMMA and etching the prior substrate. The coated graphene may then be moved to some other substrate without causing damage to the substance. Thermal release tape and polydimethylsiloxane (PDMS) are two more support polymers that have been explored. Another significant challenge is forming a perfectly uniform layer of graphene on a surface. This seems to be hard to achieve because diffusion and convection impact the kinetic transport dynamics of gas, which means that these values fluctuate within the area of a reaction chamber, influencing the chemical reactions on the surface. Also, due to fluid dynamics, by the time the gas reaches the far ends of the surface, the reactants may have been depleted, implying that no reaction will occur. Some scientists claim to have solved the problem by adjusting gas concentrations and integrating spin-coating techniques [47].

### **1.3.3. Epitaxial growth on metal**

It is a renowned technique for the production of a graphene sheet. The name “epitaxy” comes from the “Greek prefix epi, which means upon, and taxis, which means order.” Epitaxial growth occurs when deposition of a single layer on a single crystalline substrate, resulting in an epitaxial layer or sheet. It is a widely used single-crystalline SiC substrate

to make high crystalline graphene. Based on the substratum, hetero and homo-epitaxial growth are practiced. When the same material is used for sheet and substrate, the homo-epitaxial sheet is formed while in case of different materials hetero-epitaxial sheet is formed. Bommel et al. were the first to describe graphite production from both the 6H-SiC (0001) and 6H-SiC (0002) interfaces [48]. The quantum Hall effect (QHE) has been used to create graphene on SiC as a new resistance standard. Even a SiC surface must be thermally graphitized in this procedure, which is very costly. This method, however, has certain disadvantages, such as an increased processing temperature and the complexity of switching to a different substrate [49]. The growth of graphene layer on a metal surface is depicted in Fig. 5.

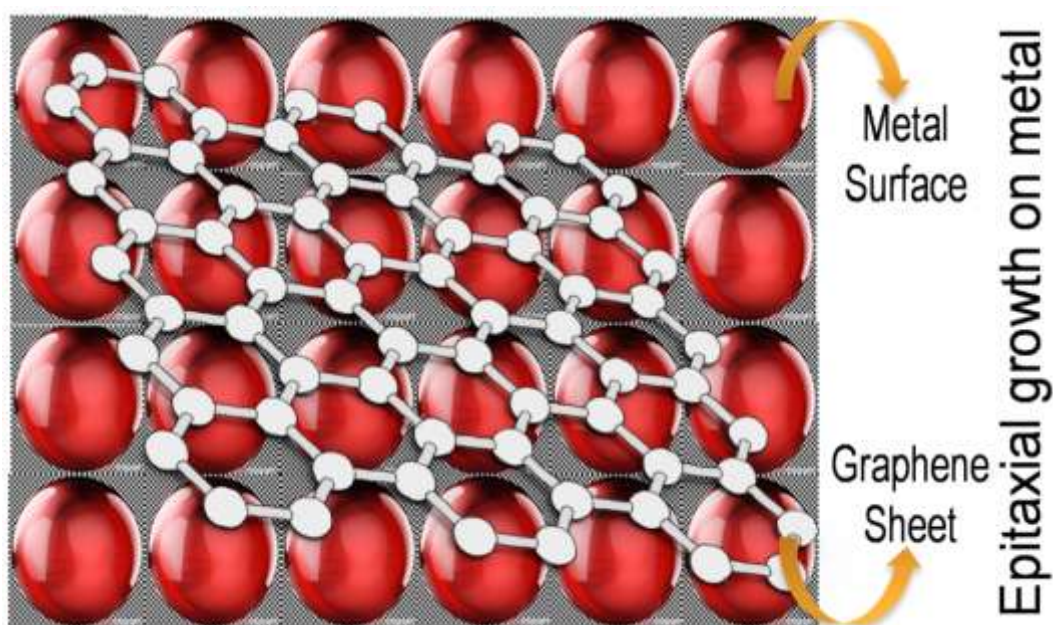


**Figure 1.5** Graphene layer growth on a metal surface

Ex-situ deposition of liquid substrates and liquid phase deposition (LPD) methods are used to produce epitaxial graphene on d-block metal surfaces. The functionality of LPD is highly dependent on the transition metal surface used. The manner, the substrate is given, has little effect on the production of a graphene monolayer in Pt(111), Ir(111), and Rh(111). The development of graphene in Ni(111) is greatly influenced by the synthesis technique used [50]. Considering the exciting recent advances in graphene manufacturing, the second challenge of controlled doping must be overcome before graphene can be used

in any type of electrical device. The second epitaxial growth approach on metal is thermally breakdown on the d-block element plane of different molecules of carbon [51].

#### **1.3.4. Liquid-phase exfoliation (LPE)**

LPE was applied in 2008, and emerged as a successful method for the synthesis of graphene. There are three key steps in this synthesis process. The first step involves dispersion of graphite in appropriate solvent, second is exfoliation and third remains purification so that the exfoliated material can be separated from non-exfoliated material. Several aqueous and non-aqueous solvents have been used for this purpose. Solvent selection mainly refers to the factors like surface tension, solubility parameters and surface energies. The solvents have reference surface energy 70–80 mJ/m<sup>2</sup> and surface tension 40–50 mJ/m<sup>2</sup>. These energies are quite similar to that of graphite, thus this process offers easier exfoliation and minor mixing enthalpy [52].

#### **1.3.5. Wet chemical synthesis**

Graphene's characteristics have led to plenty of ground-breaking achievements. For example, graphene's exceptional charge transfer mobility and other electrical characteristics are thought to mark the start of the post-silicon era. Graphene also has a superior mechanical property and high thermal conductivity. Many uses, including sensors, transparent conductive sheets, and electronic devices, are made possible by these characteristics. However, there is still a need for a viable technique based on flexible wet chemistry [53]. The numerous methods used for obtaining the graphene include mechanical cleavage of graphite, epitaxial growth on different substrates, chemical vapor deposition (CVD) on metal foils. These techniques produce high-quality graphene with minimal errors. Furthermore, the major obstacles are the incorporation of monolayer graphene in multilayer gadgets or adjusting graphene characteristics, or making graphene solutions processable. For more than a decade, scientists have known that graphite may be oxidized to graphite oxide. GO has ambient property for making solution in polar solvents as well as in aqueous medium, providing significant processing advantages while the

graphite isn't soluble [54]. Despite extensive research on the oxidation of GO, it could not be employed as a starting material for graphene synthesis. This is due to persistent defects that cannot be repaired, due to the incomplete separation of carbon atoms of monolayer graphene.

Highly oxidized and extensively damaged areas coexist with  $1 \times 10^{-9}$  m diameter in these graphene precursors. Covalently bound oxygen addends could be removed from GO via thermally, chemically, or a combination of methods, resulting in decreased GO that is nevertheless dominated by defects. The deficient atoms of graphene vanished throughout GO synthesis preclude the regeneration of a lattice of pure graphene, even if heated at  $1100\text{ }^{\circ}\text{C}$  will not recover the honeycomb lattice. Currently discovered that the instability above  $50^{\circ}\text{C}$  resulting  $\text{CO}_2$  removal causes hole flaws. The GO was discovered to be metastable only at ambient temperature. The flaw in GO is being caused by  $\text{CO}_2$  production during the oxidative synthesis. Dimiev et al. showed over one  $\text{CO}_2$  molecule is produced for every 35 carbon atoms, resulting in a persistent flaw that prevents the production of pure graphene monolayer. This indicates the GO production requisite significant or the controlled changes to avoid the hexagonal-sheet structure from rupturing and the creation of  $\text{CO}_2$ . The synthetic process must prevent carbon atom breakage to create graphene of satisfactory grade from GO. For the first time, it is reported that the graphene is made from GO using a synthetic technique that preserves the carbon skeleton to the order of 10 nm [55].

GO is formed via graphite oxidation with potassium permanganate ( $\text{KMnO}_4$ ) by suspending the graphite with sodium nitrate ( $\text{NaNO}_3$ ) in sulphuric acid ( $\text{H}_2\text{SO}_4$ ) at  $0^{\circ}\text{C}$ , according to a standard Hummer's technique. The response usually takes 1 h and the temperature rises to around  $35\text{ }^{\circ}\text{C}$  during this period. Work-up is accomplished by either adding a lot of water or dumping the liquid into the icy water [56]. After ultrasonic treatment, the manganese salts are made soluble by hydrogen peroxide ( $\text{H}_2\text{O}_2$ ) treatment (yellow intermediate form), then washed with deionized water and methanol, collected the

semi-liquid paste, and put in the oven for 6 h at 60 °C. Longer oxidation duration (16 h) at temperature below 10 °C was used in our modified method to develop a novel type of graphene oxide (nGO) to reduce CO<sub>2</sub> production throughout the oxidation and notably during workup [57]. To prevent the heating of conc. sulfuric acid, cold water was supplied constantly over one day to stop the reaction. This is a key distinction from Hummers' approach in that it preserves the carbon structure of nGO on the nano scale. Finally, the GO was separated by utilizing the above mentioned purification and exfoliation techniques at a temperature below 10 °C [58]. Even though the yield of nGO is lower than that of traditionally produced graphene oxide, the process looks to be scalable (cGO). However, the yield of cGO is reduced because the graphite oxide precursor doesn't at all exfoliate fully. After reduction, 1 g of graphite generates 400 mg of nGO and approximately 190 mg of graphene. For comparing to cGO, the yellowish nGO was freeze-dried. Because of the high degree of functionalization, flaws in the carbon lattice are undetectable and the spectral characteristics of nGO and cGO are almost similar, as predicted. To obtain graphene following reduction of nGO, defect concentrations must be below 0.1%, necessitating the use of very sensitive analytical techniques to detect substantial variations between nGO and cGO [59].

### **1.3.6. Micromechanical exfoliation**

Exfoliate a single layer of a graphene sheet by micro mechanically is the prominent and most unusual method and it is identified as first technique of graphene production. It works on the top-down nanotechnology approach. A longitudinal or transverse tension is created on the surface of layered frameworks. The mild attractive force that binds graphene single layer to other layers is called Van der Waals force in which  $1.42 \times 10^{-10}$  m is the distance between each layer [60, 61]. Peeling/exfoliation may be accomplished using some tools, including scotch tape, ultrasonication, electric fields, etc. The original technique of producing graphene was micromechanical cleavage of graphite using adhesive tape to pry apart graphene layers, and it is still frequently employed in academic research and

industrial applications [62]. The adhesive platform allows for direct application of impact to a single graphene sheet to separate them, ideal for producing premium-grade layers. Mechanically exfoliation is the most common method for exploring graphene sheets. Mechanical exfoliation is commonly understood by two fracture approaches. In the first fracture, sonication is perpendicular to the plane of the graphene layer and lateral to the plane in the second fracture approach [63]. Polymethylmethacrylate (PMMA) and polydimethylsiloxane (PDMS) were used to construct the polymer 'sticky tape'. Due to the massive side groups of PMMA, the PDMS is a typical polymer for graphene transfer. The sticky tapes were constructed on top of the lattice at a 0.5 relative density. Polymers were formed up with 100 monomer units, which are likely lower in molecular weight than commercial sticky tape but higher in entanglement length, preserving adhesive characteristics. After that, for peeling out the graphene layer two separate leveled polymer sticky tapes were repositioned to the opposite faces, with a 10 mm starting gap between the polymer and the graphite, but the flat piece of graphite sandwiched between them [64].

### **1.3.7. Electrochemical synthesis**

Electrochemical synthesis of graphene sheets is a one step treatment and can be classified as a sub category of graphite exfoliation [65]. In this case, two high purity graphite rods are used as electrodes. These electrodes are immersed in the electrochemical cell containing ionic liquid and water, subject to the static potential. In these conditions, the anode is corroding to a black precipitate gradually appearing in the reactor. The stable graphene dispersion is obtained on the completion of electrolysis. It is directly filtered to form a graphene paper, washed and then dried to get bulk powders of graphene.

### **1.4. Synthesis of graphene derivatives**

By the time, chemistry of graphite oxide has advanced much through energies of scientists worldwide, particularly when it became a known capable candidate. Graphene oxide (GO) a derivative of graphene was found to become the most perceptible result of the graphene research worldwide offering commercialization prospects and large-scale production.

Initially at the time of production of graphene, several solvent based methods have been applied to oxidize graphite. In 1859, Brodie was first to use mixture of two solvents like potassium chlorate ( $\text{KClO}_3$ ) and nitric acid ( $\text{HNO}_3$ ) and he was successful to extract graphene oxide. However, the method was less popular because time taken in such process was long and the solvents used were hazardous. Staudenmaier has also cast-off the similar solvents and extracted GO successfully. He adjusted the acid constituent via adding  $\text{H}_2\text{SO}_4$ , interpreting the method with reckless reaction completion under one single-vessel and thus better-quality of yield was obtained. Later, Hummer synthesized GO by using concentrated sulphuric acid ( $\text{H}_2\text{SO}_4$ ), sodium nitrate ( $\text{NaNO}_3$ ) and potassium permanganate ( $\text{KMnO}_4$ ) as solvent. Later, Hummer modified the method, known as modified Hummers' method which is the most widely used method for synthesis of GO at present, in which  $\text{H}_2\text{SO}_4$  and phosphoric acid ( $\text{H}_3\text{PO}_4$ ) have been used in (3:1) along with potassium permanganate as oxidizing agent. Many solvents have been used to examine the effect of solvent on graphene synthesis. To one side from solvent selection, the variation of sonication also turns out to be vital for graphene exfoliation to produce single-layer graphene. Ultrasound was used chiefly to exfoliate graphite in an appropriate solvent [66]. Though LPE is a widely common method of graphene synthesis, still sonication can lead to some flaws can be shaped on the edge and basal planes. Sonication time is also one of the important factors in exfoliation since concentration of graphene depends on this situation. Other factor may be centrifugal force which results in comparatively thin graphene flakes. On the other hand, optimization of temperature and sonication can be a factor in order to reduce imperfections in graphene by using LPE.

#### **1.4.1. Chemical vapor deposition (CVD)**

CVD is a large-scale bottom-up synthesis method used for the manufacturing of superior quality exfoliated graphene. In this method, molecules of gas combine with substrate on a surface in a quartz reaction chamber in the presence of definite pressure, temperature and rate of gas flow. Variety of substrates has been used to support production of graphene



such as nickel, copper, iron etc. The carbon sources generally used are methane, ethyne etc.[67]. Generally, two CVD procedures are used to stimulate carbon sources, i.e., thermal CVD (T-CVD) and plasma enhanced CVD (PE-CVD). The former requires vacuum tube, vacuum pump, vacuum gauge, heating furnace and mass flow controller to regulate carbon material and the gas source while in later plasma technique; power source is microwave, radio frequency or direct current that leads to breakdown of gas source at low temperature and pressure which results in the development of graphene films on the metal substrate. Sometimes, gaseous hydrocarbons and certain liquid hydrocarbon precursors such as pentane or hexane are also used [68].

Till now numerous metallic (Cu, Ni, Pd, Ru etc.) substrates have been used for deposition of graphene in CVD but the most commonly used substrates are Cu and Ni because these not only offers uniform and enlarged surface area but also comparatively cheaper and can be easily extracted without affecting graphene chemically.

#### **1.4.2. Arc discharge**

The first method, in general has been used to produce carbon nanotubes (CNT) and fullerene and later applied to graphene. An electric current is used to produce the plasma at very high temperature for the extraction of graphene. After completion of discharge, the produced soot is collected underneath ambient situations. This method was found to be useful but it was fairly expensive due to pre-requisite vacuum equipment. So as to reduce the cost of synthesis, researchers succeeded in developing graphene via this method in air medium. For air medium, maintenance of extremely high pressure of air was carried out which resulted into graphene sheets with thickness of range ~100–200 nm which is comparable to that produced in H<sub>2</sub> atmosphere. Besides, one of the inexpensive processes of synthesis under this category was found to be performed in water as medium from petroleum asphalt as raw material. This is an exceptional method as it requires no metal catalyst and low cost, high quality, time saving and simple [69].

### **1.4.3. Epitaxial growth (EG)**

Epitaxial growth is one more alternative method for the synthesis of graphene. Depending on the substrate, it may be either homo-epitaxial, i.e., when deposited material homogenize with substrate material or hetero-epitaxial when two materials turn out to be different. This process emerges in 1893 by Edward Goodrich Acheson, who produced Si-C by annealing carbon substrate at high temperature. It was observed that when Si-C was heated at around 4000 °C, pure crystalline graphite is obtained. This finding was re-used lately in 1990 when development of fullerene and nanotubes was taken into account [70]. A single-crystal of Si-C was heated and detected that a mono or few layers graphene is shaped at the temperature 1000 °C. Graphene was observed to get deposited rapidly on the C-face in comparison to the Si-face. Investigators observed that the other conditions are also responsible for the separation of graphene on Si-C surface, thus giving rise to a formation of isolated single layer of graphene. Usually, the superior quality and large-scale graphene can be manufactured by epitaxial growth on Si-C and it is currently in highly demand for electronic applications such as high frequency electronics, radiation equipment and light emitting devices. At room temperature, epitaxial graphene can act as an insulator due to an appreciable band gap between layers of graphene and Si-C material. However, the high cost of production of epitaxial Si-C graphene and inhomogeneity are two major limitations of this method. It was observed that Si-face offers better uniformity to the formation of graphene layers [71].

### **1.5. Reduction of graphene oxide**

The properties of GO can be improved by developing one more derivative of GO, i.e., reduced graphene oxide. Reducing GO has been a vital process for improving the properties of GO. On reduction, its electrical conductivity enhances significantly. On large scale, chemical reduction of graphene has been found to be most relevant method. Under this process, GO is exfoliated at first so as to get separated into GO sheets with the help of appropriate reducing agent. Numerous reducing agents such as hydrazine monohydrate

[72], sodium borohydride, glucose, pyrrole, ascorbic acid and several compounds containing sulfur have been used. The process of reduction of GO eliminates major volume of oxygen containing functional groups thereby increasing conductivity of GO. To decrease the harmful effects of these chemical, eco-friendly methods are being adopted from few years. However, the quality of product decreases on using eco-friendly reducing agents. An electrochemical process has been used for reduction of GO, under a three-electrode set up containing GO suspension as electrolyte. The reduced product obtained via electrochemical process had improved functional groups and better electrical properties [73]. It has been observed that the reduction processed for upto 72 h give rise to significantly better reduced GO [74]. Exposure of UV light on GO is another method to reduce GO. On the other hand, a thermal reduction can also be effective as per the literature report.

## **1.6. Graphene based nanocomposite**

Graphene is the most promising material for using in the nanocomposite production due to its outstanding mechanical, electrical, and thermal properties. There are several parameters which affect the properties of the nanocomposites. Nowadays, a vast amount of research has been conducted to improve the various properties of graphene based nanocomposites [75]. However, pristine graphene is not used for the fabrication of nanocomposite which is extremely difficult, so its derivatives like GO and rGO are being used generally.

### **1.6.1. Graphene based polymer nanocomposite**

Graphene based polymer nanocomposites are made by different techniques by reinforcing the graphene in the polymer matrix and used for numerous applications. However, the homogeneous dispersion of graphene in matrix is helpful to improve the properties of nanocomposites. In case of in-situ polymerization technique, a good dispersion of graphene nanofiller to the matrix is obtained and strong bonding between matrix and filler material is achieved [76]. Wang et al. used in-situ polymerization process to synthesize graphene oxide/polyamide composite. Nevertheless, during the polymerization process,

viscosity increases which reduces the loading fraction that eventually affects the production of nanocomposite [77].

Another, widely used graphene based thermoplastic nanocomposite production method is melt mixing generally used in the industries. Guan et al. also suggested some approaches for making nanocomposites which showed potential applications for developing the energy storage devices, electromagnetic interference shielding, oil/water separation, and sensors [78]. Salimikia et al. have synthesized polyaniline/GO nanocomposite using electrospinning technique and this nanocomposite was successfully used as a biosensor to detect the nicotine [79]. Moreover, Farajvand et al. prepared the graphene oxide/polyaniline nanocomposite by chemical method. This nanocomposite was also developed to be a potential biosensing material [80].

It was observed that the addition of a very small amount of graphene to the polymer matrix significantly increases the tensile strength, young's modulus as well as toughness [81]. Stankovich et al. have studied the molecular level dispersion of single graphene polymer composite and observed tremendous improvement of stiffness, fracture toughness and thermal conductivity of the composite [82]. Likewise, Papageorgiou et al. noticed that the addition of graphene filler does not reduce the breaking strain of the polymer composite even the agglomeration of the fillers occurs during the elongation of the nanocomposite [83]. A better dispersion [84] of the filler was reported and the composite displayed very high electrical conductivity. Yu et al. also synthesized a novel composite which showed the special structural arrangement and therefore it was highly electrically conductive and used as electrochemical capacitance [85].

### **1.6.2. Graphene-metal nanocomposite**

In metal matrix composites (MMCs), graphene was first introduced with aluminum (Al) by Bartolucci et al. in the year 2011 [86]. They used powder metallurgy technique but properties of the nanocomposite were not upto the mark. However, Wang et al. explored flake powder metallurgy technique using graphene nanosheets (GNSs) and observed

improvement in the mechanical properties. Li et al. used the hot press technique and reported the enhancement in elastic modulus and hardness significantly. Due to the easy control of the rGO content and the simplicity of the fabrication, this process becomes suitable for large-scale production [87].

Copper, nickel, magnesium and iron were also used in place of aluminum for making graphene-metal composite. Chen et al. have fabricated the magnesium-graphene composite and results obtained were found to be encouraging [88]. Rashad et al. have explored a novel semi-powder metallurgy followed by hot extrusion for the development of magnesium-graphene composites. The ductility of the composite remains at the acceptable level [89]. These scientists were looking for the synergistic effect of CNTs and graphene on mechanical properties of pure. Their results of mechanical property improvements supported graphene's compatibility as reinforcement in the magnesium matrix [90].

### **1.6.3. Graphene based hybrid composites**

The graphene based nanocomposites were developed by using hybrid nanofillers which improve the properties of nanocomposites. An agglomeration of graphene was also overcome by these hybrid fillers. The production cost of hybrid nanocomposite can be relatively cheaper as a very small amount of graphene is being used with carbon fiber (CF) and glass fiber (GF) [91]. The mechanical properties of carbon nanotube (CNT) and graphene nanoplatelets (GNP) reinforced hybrid polymer composite was investigated [92]. The functionalized CNTs and GNPs hybrid fillers based nanocomposites demonstrated an improved mechanical properties and thermal conductivity in comparison to unfunctionalized reinforcements.

Lin et al. have prepared the hybrid nanocomposite by adding the silica ( $\text{SiO}_2$ ) and rGO to styrene-butadiene rubber matrix. This hybrid nanocomposite exhibited tremendous improvement in the properties like tensile strength and modulus strength and suggested as an alternative material for green tire applications and high-performance rubber products [93]. Once the particulate reinforcements were replaced by fiber reinforcements, the hybrid

composite displayed almost three times increment of tensile modulus than that of the pristine material [94]. The graphene reinforced epoxy demonstrated higher fatigue life as compared to the CNT reinforcement due to the high surface area, the delay caused by separation layer in the graphene reinforced composite increases the fatigue life [95]. The hybrid composite made of epoxy laminates, fiber reinforcements along with the graphene also exhibited low impact damage [96].

### **1.7. Application of graphene**

The graphene based nanocomposites are very useful because of their extraordinary multifunctional properties. These nanocomposites are being used in various applications such as energy storage, membrane separation technology, supercapacitors and sensors etc. A few important applications are being discussed in the present thesis as reported in the following sections.

#### **1.7.1. Energy storage**

The literature reveals that the graphene is widely used in the devices to produce the renewable energy. A novel structural design was developed by fabricating a hierarchical graphene foam through a simple one-step plasma-enhanced chemical vapor deposition (PECVD) method [97]. This graphene foam was used to convert the solar energy to electrical energy in solar systems. Other than the solar system, graphene has been used in other electrical devices [98]. The graphene based metal oxide hybrids are also used in the supercapacitors and batteries. Further improvement in performance was reported when graphene based materials have been introduced as a 3D skeleton to develop anode. These newly developed graphene anodes show good electrical conductivity and high porosity structure therefore, excellent performance of lithium-ion batteries can be achieved [99].

#### **1.7.2. Membrane**

Graphene membrane having nanopores is a potential candidate in the membrane separation technology. Sint et al. study showed that the nanoporous graphene monolayers may be used for desalination and energy storage applications. Cohen-Tanugi et al. also

investigated the desalination of water through these membranes and reported the water permeability as 66 L/cm<sup>2</sup>. This value is 2–3 times higher than the conventional reverse osmosis membranes [100].

### **1.7.3. Graphene composites at low temperature environments**

Nowadays, the engineering industries especially the automotive and aerospace are mainly focusing on the lightweight materials to reduce the overall weight of the product. Hence, the fiber reinforced polymer (FRP) composites have found the significant interests in industrial sector and space applications. Thermosetting resins are commonly used as a matrix for carbon fiber reinforced polymer (CFRP) as they are chemically inert and thermally stable and possess moderate mechanical and electrical properties [101]. Hung et al. have coated the GO on the fabrics by using electrophoretic deposition method to enhance the Young's modulus and ultimate tensile strength of the composites. Wu et al. revealed that the graphene nanoplatelets (GNPs) act as a bridging filler to mitigate the crack surfaces to prevent the crack propagation in Al<sub>2</sub>O<sub>3</sub>. Maximum fracture toughness of GNP/Al<sub>2</sub>O<sub>3</sub> was measured by only using 1.0 vol% GNPs [102].

### **1.7.4. Miscellaneous applications**

The graphene materials have also been used in other applications such as contaminant sensing and water treatment etc. Graphene-based sorbent and photocatalytic materials are used for environmental refinement [103]. Cho et al. have developed LED lamp by using graphene reinforced polyamide nanocomposites. On using a titanate coupling agent for reducing the air voids in graphene sheets, the load transfer between the polymer and graphene increases the thermal conductivity of the composite which is suitable to develop the LED lamp [104]. Further, graphene materials are also useful in developing paints that involve conductive ink, antistatic, electromagnetic interference shielding, and gas barrier [105]. The gas sensors were fabricated by graphene composites exhibit the better sensitivity than single-walled carbon nanotube (SWCNT) based sensors in detecting hazardous gases and toxic elements and therefore demonstrates its promise to use in the

future generation flexible and stretchable sensors for wearable technology [106].

### **1.7.5. Physical sensors**

The outstanding properties of graphene make it exceptionally popular to develop different kinds of sensors for the detection of tiny analytes like hydrogen, ethanol, methanol, isopropanol, gaseous ammonia, nitrogen dioxide, methane, water, and hydrogen cyanide etc. However, the oxygenated functional groups make GO nanosheets useful in biosensors. In biosensors, graphene is used as impedance material, electron transfer material and for transferring phonon/photons [107]. The temperature sensing is another area of research where graphene based materials is used. High quality graphene is the key for this type of sensors [108].

### **1.7.6. Biomedical applications of graphene oxide**

The biomedical application is another fascinating area where GO is being used. The research on biological applications of graphene and its derivatives is much attractive worldwide due to many fascinating properties. The graphene oxide (GO), prepared by oxidation of graphite under acidic conditions offers several advantages over pure graphene due to the high dispersibility in aqueous media, which is essential for the biological applications. The low cost, scalable production and facile biological/chemical functionalization are also important advantages of GO over pure graphene. The use of graphene oxide (GO) as an efficient nanocarrier was first reported by Dai et al. for drug delivery and later it is explored to other biomedical applications. These include biological sensing, imaging, and biocompatible scaffold for cell culture etc. Sun et al. first reported the suitability of GO as a nano-carrier for drug delivery in 2008 [109]. Nowadays, the potential of GO for the delivery of cancer treatments and anti-inflammatory drugs have been explored [110]. Wang et al. reported an interfacial interaction between graphene surface and DNA and used for the DNA tethering process. This bio-interface interaction of DNA-graphene becomes useful to detect DNA using a field effect transistor (FET) [111]. Graphene has displayed the biocompatibility with mammalian cells to be useful as a



scaffold structure in tissue engineering with desired mechanical strength to support the growth of bone cells, i.e., osteoblasts for engineering bone tissue. Graphene also shows the application in drug and gene delivery [112].

## **1.8. Graphene oxide for biosensing applications**

### **1.8.1. Biosensors**

Since the dawn of time, mankind has been performing bioanalysis by using the sensory nerve cells of various body parts like nose to detect scents or tongue to taste a variety of foods due to the enzymatic reactions. Although, the canaries used in coal mines could qualify as the first biosensor. The feasibility of biosensing was first demonstrated by Leland C. Clark in the mid 1960s when he has measured glucose concentration in a solution known as Clark oxygen electrode. Since then, hundreds of biosensors have been developed around the world. Over the years, scientists have developed new means of chemical analysis using bioreceptors from biological organisms having the high selectivity of these biological recognition systems. The biorecognition elements along with different transductions have created the rapid bioanalysis and the technology was named as biosensors. Scientists have contributed to the development of reliable and robust biosensing devices for various applications in medical/clinical analysis, veterinary, agriculture, food quality, environmental analysis and bioterrorism prevention fields etc.

Biosensor is a device which is used for the detection of analyte or chemical substances on combining with a biological component with a physicochemical detector. These analytical devices having biological sensing or bio-recognition element which is attached with a transducer that produce an electronic signal. Selectivity and specificity are very important features of the device depending on the immobilized biological recognition element attached to a suitable transducer. The device detects, records and gives information of a physiological change or process. It has specific biochemical reaction to detect chemical compound in a biological sample or analyt.

### 1.8.2. Components of a biosensor

Biosensor has three major components as (i) a bio-recognition element such as enzyme, DNA, antibody etc. for recognition of an analyte also known as bio-receptor, (ii) an immobilization matrix such as conducting polymers, nanomaterials [113], sol-gel films [114], and self-assembled monolayers [115] which are being used for the immobilization of a biomolecule and (iii) a transducer unit for conversion of biochemical reaction product into a recognizable signal as shown in Fig. 6. Bio-receptor and transducer together may also be referred as a biosensor membrane.

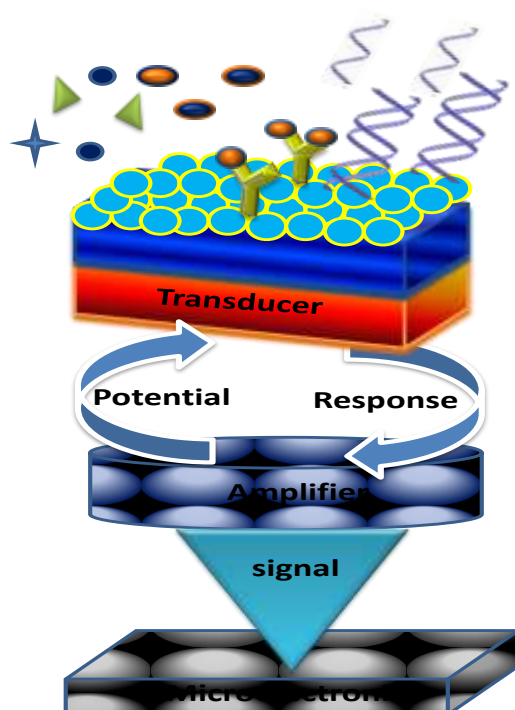


**Figure 1.6** Various components of a biosensor

#### 1.8.2.1. Biomolecular recognition elements in biosensors

The biomolecular recognition element also known as bioreceptor is a biomolecule or a molecular assembly which is capable to recognize a target molecule/substrate, i.e., an analyte. The bioreceptors commonly used are antibodies, enzymes, DNA or whole cells etc. The specificity of the bioreceptor molecule makes the biosensor specific.

#### 1.8.2.2. Immobilization matrices

A matrix can be utilized for immobilization or integration of desired biomolecules at a

transducer surface and efficiently maintain the functionality of the biomolecules and at the same time provides accessibility towards the target analyte and an intimate contact with the transducer surface. The chemical properties of a desired solid support are helpful to decide the method of immobilization and operational stability of a biosensor. For a preferred immobilizing matrix, it should be resistant to a wide range of physiological pH, temperature, ionic strength and chemical composition. Among the various immobilizing matrices, carbon nanomaterials (particularly functionalized CNTs and graphene) receiving a great deal of attention owing to their exceptional optical and electronic properties [116]. Their large surface area, high thermal and mechanical stability, abundant functional groups, biocompatibility and the capability towards the direct electron transfer of proteins make them ideal candidate for the fabrication of a biosensor. The desired biomolecules can be immobilized on the surface of CNMs both covalently and non-covalently.

The physical and catalytic properties of graphene make it ideal for sensing applications. Graphene due to its large specific surface area, excellent conductivity, ease of surface functionalization and faster electron transfer kinetics, has recently been explored for application in electrochemical biosensors. The large surface area of graphene facilitates large amounts of defects and thus, electroactive sites. The oxygen containing groups present on the graphene sheets are mainly responsible for the faster electron transfer kinetics. Since, the most atoms of graphene sheets are exposed to the surface, slight changes in the charge environment due to the adsorption of biomolecules provide significant changes in their electrical properties which helps in fabrication of more sensitive biosensors [117, 118].

### **1.8.2.3. Transducer**

In a biosensor device, the transducer is an element which converts one form of energy into the other form. In other words, the role of the transducer is to convert the bio-recognition event or biochemical interactions outcome into a measurable electronic signal. This

process of energy conversion is known as signalisation. The main types of transducers are electrochemical, piezoelectric, optical, electrical, thermal and magnetic etc. Mostly, the transducers produce either optical or electrical signals which are directly proportional to the amount of analyte-bioreceptor interactions. Electrochemical biosensors measure change in electric distribution and have been widely used in biosensor fabrication as they show excellent selectivity, sensitivity, stability, reproducibility, and quick maintenance with minimum cost.

### **1.9. Cancer**

All living things are made up of different types of cells like blood cells, liver cells, brain cells etc. The cells in a normal adult only grow and divide slowly in a programmed manner so that the number of cells in each tissue remains the same. An abnormal and uncontrolled cell growth due to the accumulation of specific genetic and epigenetic defects, both environmental and hereditary in origin is undesired and resulting in a disease called as cancer. Such undesired and unregulated cell growth leads to the formation of a tumor mass that over the time becomes independent of normal homeostatic checks. These tumors can grow and interfere with the digestive, nervous, and circulatory systems and release hormones that alter the body function. Tumor cells become resistant to apoptosis and other antigrowth defense mechanisms within the body. Tumors formed in one spot and if demonstrate limited growth are generally considered to be benign. As the cancer progresses, a cancerous cell moves throughout in the body using the blood or lymphatic systems and then destroying healthy tissue called an invasion process. This cell manages to divide and grow, making new blood vessels to feed itself in a process called angiogenesis and metastasize to other body organs and systems and eventually becomes incurable [119]. Cancers begin when one or more genes in a cell experience a mutation that makes the cell more likely to divide abnormally. The modified cell and its descendants grow and divide oftenly is called as hyperplasia. One of these cells again experiences another mutation which further increases its tendency to divide. Thus, the cell's descendants divide

excessively and look abnormal and this condition is called as dysplasia. Such mutations may continue with the passes of time and developing the tumor very abnormal in growth and appearance. If the tumor formed still contained within its tissue of origin is called as in-situ cancer. While, if cells experience additional mutations which allow the tumor to invade neighbouring tissues and shed cells into the blood or lymph, this tumor is known as malignant. Moreover, the escaped cells may develop new tumors (metastases) at other locations in the body. So far, several different types of cancers have been reported that include Sarcoma, Lymphoma, Carcinoma, Leukemia, Melanoma, Brain, Multiple Myeloma, Spinal cord tumors, Neuroendocrine, Germ cell, and Carcinoid tumors among many [120]. The names and types of cancer are based on their origination from the tissues or organ where these cancers are developed. As per the need of time, an accurate and reliable detection of these tumor markers is essential for early detection, which may significantly improve the effective treatment and survival of the patients. There are more than 100 types of cancer, viz., oral cancer, breast cancer, lung cancer, liver cancer, gallbladder cancer, pancreatic cancer, prostate cancer, bone cancer, retinoblastoma, colorectal cancer, oesophageal cancer, kaposi sarcoma, leukemia, melanoma, skin cancer etc. The types of cancer are usually named after the organs or tissues where these cancers develop in the body.

According to the GLOBOCAN 2012 estimates, there were about 14.1 million new cancer cases, 8.2 million cancer deaths reported and 32.6 million people living with cancer disease (within 5 years of diagnosis) worldwide in 2012. Among all these, about 57% (8 million) of new cancer cases, 65% (5.3 million) of the cancer deaths and 48% (15.6 million) of the 5 year prevalent cancer cases found in the under developed countries like India. It is revealed that the high mortality rates of cancer patients in developing countries is most likely due to the combination of both; the delay in diagnosis and a limited access to timely and standard treatments.

### **1.9.1. Diagnostic evaluation of cancer**

With high morbidity and mortality, cancer has become a big health threat or problem around the world [121]. Both the pathology as well as medical imaging are two main techniques used in tumor clinical diagnostics. Pathological diagnosis technology mainly includes tissue biopsies, serological indicators (e.g., CEA and PSA) test and molecular pathology test (e.g., FISH, RT-PCR and NGS)[122]. While, the medical imaging methods like ultrasonic testing, X-ray imaging, CT, MRI, PETCT and endoscopy etc. have been used for the clinical applications.

#### **1.9.1.1. Imaging test**

For the primary investigation of cancer, imaging test is being carried out to see what is going on inside the body. Imaging test gives us a picture of the areas inside the body where the tumour is present. This imaging test sends certain form of energy (X-rays, sound waves, magnetic field etc.) through the body and our body tissues change the energy pattern to make an image which is investigated for cancer. Diagnostic imaging can be divided into two broad categories depending on very precise anatomical details and functional or molecular images. The first method includes imaging techniques like CT scan and MRI, which provide exquisite details on lesion location, size of the cancer, morphology and structural changes around tissues. However, they provide only limited informations about the functioning of tumours. While the second method includes PET and SPECT, which gives in site into the tumour physiology down to the molecular level, but the anatomical details of the tumour is still a limitation to this technique. The imaging data usually lag behind the tumor progression for medical imaging approach. It also lacks effective biomarkers for early diagnosis in serological indicators test and therefore needs further clinical examinations. Sometimes, both the methods are integrated for the characterization of tumours in all stages.

#### **1.9.1.2. Biopsy**

Biopsy is the most common technique for diagnosing the cancer. In biopsy a sample of

tissue is removed from the body, which is analyzed by a pathologist under a microscope to look for the possibility of cancer. The pathology reports play a major role in diagnosing and deciding the possible treatment for cancer. Though, the tissue biopsy is recognized as the current gold standard for tumor diagnosis, however it has disadvantages also. These disadvantages are found due to the severe clinical complications resulting in sampling and the result bias caused by tumor heterogeneity. It is very difficult to obtain tissues in some cases especially from the terminal cancer patients. Therefore, it is very necessary to search new biomarkers which have high specificity and sensitivity for tumor diagnosis. These can be used for the dynamically and timely monitoring of tumor progression.

### **1.9.1.3. Lab-based test**

The high and low concentration of certain substance, i.e., biomarker in the body can be a symptom of cancer. Moreover, the lab tests of blood, urine, or other body fluids reveal the changes in these substances are helpful for the doctors to make a diagnosis easier. The samples data may show the cancer cells, proteins or other substances generated by the cancer. The blood tests also give an idea of well functioning of the organs and these data are deviated from the standard value, if they've been affected by cancer. However, such abnormal lab results or data are not a sure sign of cancer, therefore more lab tests involve blood testing or tissue samples for tumor markers. These markers are the substances produced by cancer cells or by other cells of the body in response to cancer. Mostly, the tumour markers are made by normal and cancer cells which are being produced at a much higher levels in cancer patients.

### **1.9.2. Cancer biomarkers**

Biomarkers play an important role in cancer research. Further research in this field offers a hope for new biomarkers for faster diagnosis and better survival rate. An increased validation and applications of currently known biomarkers may improve diagnostics and therapeutics for all cancer types. According to the National Cancer Institute (NCI), a biomarker is “a biological molecule found in blood, other body fluids, or tissues that is a

sign of a normal or abnormal process, or of a condition or disease” such as cancer. Biomarkers are helpful to differentiate an affected person/ patient from a healthy person. The alterations may be found due to the number of factors such as germ line or somatic mutations, transcriptional changes, and post-translational modifications etc. There is a variety of biomarkers which include proteins (e.g., an enzyme or receptor), nucleic acids (e.g., a micro RNA or other non-coding RNA), antibodies, and peptides etc. A biomarker may also be a collection of alterations like gene expression, proteomic, and metabolomic signatures etc. These biomarkers can be detected in the fluid circulation (blood, serum, or plasma) or excretions or secretions (stool, urine, sputum, or nipple discharge), and therefore easily assessed non-invasively and serially. If, it is tissue-derived then requires either biopsy or special imaging for evaluation. Moreover, the genetic biomarkers can be inherited and detected as sequence variations in germ line DNA isolated from whole blood, sputum, or buccal cells. These biomarkers may be identified and used to determine an individual's risk of cancer development.

### **1.9.3. Biosensor for cancer biomarker detection**

The biosensors have been used worldwide in the detection of biomarkers as the most reliable, fast, and precise analytical methods during the last decade. To detect cancer biomarkers, the biosensors utilize various biorecognition elements such as antibodies, enzymes, deoxyribonucleic acid (DNA), ribonucleic acid (RNA), cancer cells, nucleic acid probes or other specific biomolecules which are immobilized on a transducer surface [123]. The transducer transforms the biological signals into the measurable signals either electrical or optical which are obtained during the interaction between target biomarker and biorecognition molecules. The biomarkers detection processes are mainly focusing on the tracing of proteins on the surface of tumor cells membrane and/or cancer associated microRNA. Although several alternative methods were reported for such biomarker diagnosis, an electrochemical method is preferred because of its moderate cost, rapid response, ease of operation, readily quantifiable, possibility of miniaturization as



well as high sensitivity and selectivity with lower detection limit [123]. These electrochemical biosensors are consisting three important components, namely, biorecognition element, signal transducer, and three electrodes based electrochemical systems. In these biosensors, a change in electrical signal causes due to the electrochemical reactions with target components at the electrode surface is monitored and then recorded. There is a set of biorecognition elements to detect cancer biomarkers such as antibodies, enzymes, and synthetic molecules such as aptamers, DNA fragments, peptides, etc. [124]. The biosensors are mainly classified into immunosensors, aptasensors, enzymatic biosensors, and genobiosensors (nucleic acid biosensors) depending on the use of specific biorecognition elements.

#### **1.9.3.1. Electrochemical immunosensor**

The immunosensors are the biosensors based on affinity in which an immunochemical reaction is coupled to a transducer. These immunosensors are very important analytical tools designed to detect the binding event between antibodies (Abs) and antigens (Ags) without any need of separation and washing etc. The fundamental basis of all immunosensors is the specificity of the molecular recognition of antigens by antibodies to form a stable complex [125]. Immunosensors are classified as direct and indirect immunosensors. Among the four types of immunosensors, i.e., electrochemical (amperometric, potentiometric, capacitive or impedance), optical (fluorescence, luminescence, refractive index), microgravimetric and thermometric devices, electrochemical immunosensors have recently aroused much interest for the detection of desired proteins, biomarkers, biological toxins and bio-warfare agents in critical situations, e.g., food, environment, pharmaceutical chemistry and clinical diagnostics [126]. Electrochemical immunosensors employ either antibodies or their complementary binding partners as biorecognition elements in combination with electrochemical transducers and determine the level of analyte by changes of potential, current, capacitance, conductance, or impedance caused by the immune-reactions [126]. The selection of a matrix for the

immobilization of Abs is extremely important wherein, the desired Abs should be immobilized with desired orientation to obtain a sensitive, compact and stable immunosensor platform.

### **1.9.3.2. Antibodies**

The most common bioreceptor used in biosensors are antibodies and on the basis of their elective properties and the synthesis protocol they are classified as polyclonal, monoclonal or recombinant [127]. An antigen and an antigen-specific Ab interaction is similar to a lock and key fit model which is found to be the best approach. These interactions of specific Ab and its unique antigen is highly stereo-selective which form the three dimensional (3D) structures. The 3D configuration and the diversity inherent in individual Ab helps to develop an Ab which can recognize and bind to any one of a large variety of molecular shapes. This unique property of antibodies and their ability to recognize molecular structures allows one to develop antibodies that specifically bind to chemicals, biomolecules, microorganisms, etc [128].

The antibodies can be covalently modified in many ways which suits the purpose of particular assay. The immunological methods are being used to tag enzymes, biotin, fluorophores and radioactive isotopes to Ab which thus provides higher detection signal in biological assays [129]. The labelling of the antibodies can be made in two different ways. Firstly, the direct method in which a labelled Ab directly reacts with the antigen of interest. While the second method is an indirect method in which two steps are involved, firstly an unlabeled primary Ab (first layer) reacts with the antigen, and a labelled secondary Ab (second layer) which reacts with the primary Ab [130].

### **1.9.3.3 Graphene oxide for immobilization of antibodies**

The GO permits the penetration and adsorption of  $\text{TiO}_2$  into the surface of GO due to its porous nature resulting in the large surface area, better electron mobility along with many active sites available for immobilization of biomolecules on the electrode surface. Keeping this aspects in view, the efforts were been made to synthesize  $\text{rGO@TiO}_2$  nanocomposite.

Further, rGO@TiO<sub>2</sub> was used as a sensing platform for the determination of epithelial cell adhesion molecule (EpCAM) by using covalently immobilized anti-EpCAM antibodies.

### **1.10 Research objective**

Based on the literature survey and research gaps, a systematic work plan was carried out to fabricate an electrochemical biosensor based on nanocomposites. The integration of GO with nanomaterials such as metal oxide and metal sulfides have gained much interest due to the possibility to tailor the individual property of each component into an end use material. The synergistic effects of these materials tune the performance of the biosensor resulting in enhanced sensitivity and selectivity. Among the metal oxides, TiO<sub>2</sub> nanoparticles have attracted very much attention of the researchers due to its large specific surface area, high uniformity, and excellent electrochemical properties. Moreover, the porous nature of GO allows the penetration and adsorption of TiO<sub>2</sub> which facilitates more active sites for immobilization of biomolecules on the electrode surface. Further, an extremely large surface area and remarkable conducting behaviour of GO in addition to a high isoelectric point of TiO<sub>2</sub> give a new way to utilize their nanocomposite for the fabrication of biosensors. In addition to the TiO<sub>2</sub>, transition metal dichalcogenides like MoS<sub>2</sub> are being also explored due to their tunable band gap, enhanced electrical, optical and thermal properties etc. Thus, the aim has been achieved by following the steps like synthesis, functionalization and characterization of nanostructured TiO<sub>2</sub> and MoS<sub>2</sub>. The deposition of these nanomaterials was carried out onto the conducting electrode surface via electrochemical deposition/electrophoretic deposition techniques followed by immobilization of antibody. The response studies of these fabricated immunoelectrodes were investigated in detail. All these experimental studies are being reported in the present thesis.

### **1.11 Thesis organization**

The present thesis deals with the preparation, characterization and application of rGO, rGO nanocomposite with TiO<sub>2</sub> and MoS<sub>2</sub>, in the fabrication of efficient electrochemical

biosensors for sensitive and specific detection of cancer biomarkers like EpCAM in buffer samples and spiked human serum samples. **The research work of this thesis is divided into six chapters and organized as follows.**

**Chapter 1** highlights the detailed description of GO in terms of their synthetic strategies, characteristic properties and applications, with a special emphasis in biosensors. Further, the preparation and application of GO and its nanocomposites as an immobilizing matrix for biosensor applications have been discussed. It presents an overview of the various techniques available for cancer detection till date. Besides this, efforts have been made to give a descriptive literature review on cancer detection, mainly using electrochemical immunosensor. Salient features of antibodies used to fabricate electrochemical immunosensor for cancer biomarker detection have been incorporated.

**Chapter 2** provides details of the materials and various experimental techniques such as UV-visible spectroscopy, FTIR spectroscopy, Raman spectroscopy, X-ray diffraction, X-ray photoelectron spectroscopy, atomic force microscopy, scanning electron microscopy and transmission electron microscopy that have been used to characterize GO, rGO nanocomposite modified electrodes and immunoelectrodes. Electrochemical techniques including cyclic voltammetry (CV) and electrochemical impedance spectroscopy (EIS) are used to characterize the rGO nanohybrid based electrodes and immunoelectrodes. CV technique has been used to study the electrochemical response of different rGO nanohybrid immuno-biosensor as a function of EpCAM concentration. Attempts have also been made to describe the procedures and protocols used to estimate various parameters related to the performance of the rGO nanohybrid-based immuno-biosensor for cancer biomarker detection.

**Chapter 3** describes the results of the studies related to the fabrication of a sensitive, label-free and efficient electrochemical immunosensor for an early detection of epithelial cell adhesion molecules (EpCAM, tumor biomarker) by using reduced graphene oxide (rGO) titanium oxide (TiO<sub>2</sub>) nanocomposite. The hydrothermally synthesized rGO@TiO<sub>2</sub>

nanocomposite has been electrophoretically deposited on an indium tin oxide (ITO) coated glass substrate. The fabricated rGO@TiO<sub>2</sub>/ITO electrode has shown better electron transfer kinetics with an electron transfer rate constant of  $1.93 \times 10^{-7} \text{ cm s}^{-1}$  and a diffusion coefficient of  $1.07 \times 10^{-12} \text{ cm}^2 \text{ s}^{-1}$ . Further, the rGO@TiO<sub>2</sub>/ITO electrodes were used for the covalent immobilization of monoclonal EpCAM antibodies. This fabricated biosensor achieves the label-free detection of EpCAM cancer biomarkers by differential pulse voltammetry with high sensitivity ( $3.24 \mu\text{A mL ng}^{-1} \text{ cm}^{-2}$ ) and low detection limit ( $0.006 \text{ ng mL}^{-1}$ ). In addition, the fabricated biosensor showed good selectivity, reproducibility, and has the potential to be used for the early detection of cancer biomarkers.

**Chapter 4** describes the results of the studies related to the fabrication of an ultrasensitive, electrochemical biosensor where molybdenum disulfide grafted reduced graphene oxide (MoS<sub>2</sub>@rGO) nanohybrid has been used as a sensing platform. The biomolecular-assisted synthetic method has been used to synthesize MoS<sub>2</sub>@rGO nanohybrid. Further, the epithelial cell adhesion molecule antibodies (anti-EpCAM) have been covalently immobilized on the MoS<sub>2</sub>@rGO/ITO electrodes for the detection of EpCAM. Our electrochemical results confirm that anti-EpCAM/MoS<sub>2</sub>@rGO/ITO based biosensor can detect EpCAM in the concentration range of  $0.001\text{-}20 \text{ ng mL}^{-1}$  with a detection limit of  $44.22 \text{ fg mL}^{-1}$ . This excellent performance of the biosensor is attributed due to the efficient immobilization of antibodies on the MoS<sub>2</sub>@rGO surface resulting in the high specificity for EpCAM. This biosensor has shown the good selectivity, reproducibility, and stability. The successful detection of EpCAM antigen in spiked samples like human saliva, serum and urine etc. enables this platform as an alternate method for early determination of the cancer biomarkers.

In **Chapter 5**, results pertaining to the development of electrochemical biosensors based on TiO<sub>2</sub>/rGO@MoS<sub>2</sub> nanocomposite have been described. Different ratios of TiO<sub>2</sub> nanoparticles were used to synthesize the TiO<sub>2</sub>/rGO@MoS<sub>2</sub> nanocomposite. The TiO<sub>2</sub>/rGO@MoS<sub>2</sub> nanocomposite was electrophoretically deposited onto ITO coated glass

substrate to fabricate an ultrasensitive label-free electrochemical immunosensor for the determination of EpCAM cancer biomarkers. Different spectroscopic and morphological techniques reveal the successful deposition of nanocomposite and immobilization of monoclonal anti-EpCAM. Electrochemical investigations indicate that the deposition of  $\text{TiO}_2/\text{rGO}@\text{MoS}_2$  nanocomposite onto ITO electrode provides a relatively larger surface area and excellent charge transfer rate. The biosensing response of the electrode shows linearity within the concentration range of  $0.0001\text{-}20\text{ ng mL}^{-1}$  and a detection limit of  $0.0001\text{ ng mL}^{-1}$ . The biosensor was found to be highly stable and reproducible and successfully validated for the determination of EpCAM antigen in spiked serum samples.

The **Chapter 6** is a brief summary of the studies related to applications of rGO nanocomposites based biosensor for cancer biomarker detection. Further, this chapter highlights the futuristic prospects and the scope of rGO nanocomposite based biosensor for other biomedical applications.

## 1.12 References

- [1] M Kivala, D Wu, X Feng, C Li, K Müllen, Cyclodehydrogenation in the synthesis of graphene-type molecules, *Synthesis of Polymers: New Structures and Methods*, (2012) 373-420.
- [2] D-H Baek, J Kim, MoS<sub>2</sub> gas sensor functionalized by Pd for the detection of hydrogen, *Sensors and Actuators B: Chemical*, 250(2017) 686-91.
- [3] CI Idumah, A Hassan, Emerging trends in graphene carbon based polymer nanocomposites and applications, *Reviews in Chemical Engineering*, 32(2016) 223-64.
- [4] L Ng, G Hu, R Howe, X Zhu, Z Yang, CG Jones, et al., *Printing of Graphene and Related 2D Materials*: Springer; 2018.
- [5] D Chen, L Tang, J Li, Graphene-based materials in electrochemistry, *Chemical Society Reviews*, 39(2010) 3157-80.
- [6] K Novoselov, oA Mishchenko, oA Carvalho, AC Neto, 2D materials and Van der Waals heterostructures, *Science*, 353(2016).
- [7] Q Tang, Z Zhou, Z Chen, Graphene-related nanomaterials: tuning properties by functionalization, *Nanoscale*, 5(2013) 4541-83.
- [8] G Liu, W Jin, N Xu, Graphene-based membranes, *Chemical Society Reviews*, 44(2015) 5016-30.
- [9] J Zhou, J Li, Z Liu, J Zhang, Exploring Approaches for the Synthesis of Few-Layered Graphdiyne, *Advanced Materials*, 31(2019) 1803758.
- [10] FM de Vasconcelos, AG Souza Filho, V Meunier, EC Girão, Electronic properties of tetragraphene nanoribbons, *Physical Review Materials*, 3(2019) 066002.
- [11] E Marinho, PA da Silva Autreto, Me-graphane: tailoring the structural and electronic properties of Me-graphane via hydrogenation, *Physical Chemistry Chemical Physics*, 23(2021) 9483-91.
- [12] AI Podlivaev, LA Openov, Elementary defects in graphane, *JETP Letters*, 106(2017) 110-5.

- [13] TK Lee, J Lee, SK Kwak, Prediction of Selective Formation of Chair-and Boat-Type Hydrogenated Graphene via Birch Reduction, *Chemistry of Materials*, 31(2019) 4584-90.
- [14] N Sharma, M Dubois, K Guérin, V Pischedda, S Radescu, Fluorinated (Nano) Carbons: CF<sub>x</sub> Electrodes and CF<sub>x</sub>-Based Batteries, *Energy Technology*, 9(2021) 2000605.
- [15] D Silva, S Azevedo, J Kaschny, Structural and electronic properties of fluorinated boron nitride monolayers, *The European Physical Journal B*, 94(2021) 1-11.
- [16] BJ Walder, TM Alam, Modes of Disorder in Poly(carbon monofluoride), *Journal of the American Chemical Society*, 143(2021) 11714-33.
- [17] X Gao, H Liu, D Wang, J Zhang, Graphdiyne: synthesis, properties, and applications, *Chemical Society Reviews*, 48(2019) 908-36.
- [18] H Huang, W Feng, Y Chen, Two-dimensional biomaterials: material science, biological effect and biomedical engineering applications, *Chemical Society Reviews*, (2021).
- [19] J Kang, Z Wei, J Li, Graphyne and its family: recent theoretical advances, *ACS applied materials & interfaces*, 11(2018) 2692-706.
- [20] T Hussain, M Sajjad, D Singh, H Bae, H Lee, JA Larsson, et al., Sensing of volatile organic compounds on two-dimensional nitrogenated holey graphene, graphdiyne, and their heterostructure, *Carbon*, 163(2020) 213-23.
- [21] M Adeel, M Bilal, T Rasheed, A Sharma, HM Iqbal, Graphene and graphene oxide: Functionalization and nano-bio-catalytic system for enzyme immobilization and biotechnological perspective, *International journal of biological macromolecules*, 120(2018) 1430-40.
- [22] DW Johnson, BP Dobson, KS Coleman, A manufacturing perspective on graphene dispersions, *Current Opinion in Colloid & Interface Science*, 20(2015) 367-82.
- [23] DA Brownson, DK Kampouris, CE Banks, Graphene electrochemistry: fundamental concepts through to prominent applications, *Chemical Society Reviews*, 41(2012) 6944-76.



- [24] M Yang, Y Liu, T Fan, D Zhang, Metal-graphene interfaces in epitaxial and bulk systems: A review, *Progress in Materials Science*, 110(2020) 100652.
- [25] S Pei, H-M Cheng, The reduction of graphene oxide, *Carbon*, 50(2012) 3210-28.
- [26] JW Suk, RD Piner, J An, RS Ruoff, Mechanical properties of monolayer graphene oxide, *ACS nano*, 4(2010) 6557-64.
- [27] M Aunkor, I Mahbubul, R Saidur, H Metselaar, The green reduction of graphene oxide, *Rsc Advances*, 6(2016) 27807-28.
- [28] O Jalil, CM Pandey, D Kumar, Electrochemical biosensor for the epithelial cancer biomarker EpCAM based on reduced graphene oxide modified with nanostructured titanium dioxide, *Microchimica Acta*, 187(2020) 1-9.
- [29] P Avouris, C Dimitrakopoulos, Graphene: synthesis and applications, *Materials today*, 15(2012) 86-97.
- [30] R Ikram, BM Jan, W Ahmad, Advances in synthesis of graphene derivatives using industrial wastes precursors; prospects and challenges, *Journal of Materials Research and Technology*, 9(2020) 15924-51.
- [31] T Mahmoudi, Y Wang, Y-B Hahn, Graphene and its derivatives for solar cells application, *Nano Energy*, 47(2018) 51-65.
- [32] A Kouloumpis, K Spyrou, K Dimos, V Georgakilas, P Rudolf, D Gournis, A bottom-up approach for the synthesis of highly ordered fullerene-intercalated graphene hybrids, *Frontiers in Materials*, 2(2015) 10.
- [33] D Jariwala, A Srivastava, PM Ajayan, Graphene synthesis and band gap opening, *Journal of nanoscience and nanotechnology*, 11(2011) 6621-41.
- [34] MJ Allen, VC Tung, RB Kaner, Honeycomb carbon: a review of graphene, *Chemical reviews*, 110(2010) 132-45.
- [35] AB Kaul, Two-dimensional layered materials: Structure, properties, and prospects for device applications, *Journal of Materials Research*, 29(2014) 348-61.
- [36] M Cai, D Thorpe, DH Adamson, HC Schniepp, Methods of graphite exfoliation,

Journal of Materials Chemistry, 22(2012) 24992-5002.

[37] W Choi, I Lahiri, R Seelaboyina, YS Kang, Synthesis of graphene and its applications: a review, *Critical Reviews in Solid State and Materials Sciences*, 35(2010) 52-71.

[38] T Kuila, S Bose, AK Mishra, P Khanra, NH Kim, JH Lee, Chemical functionalization of graphene and its applications, *Progress in Materials Science*, 57(2012) 1061-105.

[39] X Huang, X Qi, F Boey, H Zhang, Graphene-based composites, *Chemical Society Reviews*, 41(2012) 666-86.

[40] S Ray, Applications of graphene and graphene-oxide based nanomaterials: William Andrew; 2015.

[41] H Zhang, F Ding, H Li, F Qu, H Meng, H Gu, Controlled synthesis of monolayer graphene with a high quality by pyrolysis of silicon carbide, *Materials Letters*, 244(2019) 171-4.

[42] HO Pierson, Handbook of chemical vapor deposition: principles, technology and applications: William Andrew; 1999.

[43] K Bazaka, MV Jacob, K Ostrikov, Sustainable life cycles of natural-precursor-derived nanocarbons, *Chemical reviews*, 116(2016) 163-214.

[44] Z-Y Juang, C-Y Wu, C-W Lo, W-Y Chen, C-F Huang, J-C Hwang, et al., Synthesis of graphene on silicon carbide substrates at low temperature, *Carbon*, 47(2009) 2026-31.

[45] L Banszerus, M Schmitz, S Engels, J Dauber, M Oellers, F Haupt, et al., Ultrahigh-mobility graphene devices from chemical vapor deposition on reusable copper, *Science advances*, 1(2015) e1500222.

[46] V Singh, D Joung, L Zhai, S Das, SI Khondaker, S Seal, Graphene based materials: past, present and future, *Progress in materials science*, 56(2011) 1178-271.

[47] J Kang, D Shin, S Bae, BH Hong, Graphene transfer: key for applications, *Nanoscale*, 4(2012) 5527-37.

[48] GR Yazdi, T Iakimov, R Yakimova, Epitaxial graphene on SiC: a review of growth

and characterization, *Crystals*, 6(2016) 53.

[49] Y Hu, M Ruan, Z Guo, R Dong, J Palmer, J Hankinson, et al., Structured epitaxial graphene: growth and properties, *Journal of Physics D: Applied Physics*, 45(2012) 154010.

[50] CJ Shearer, D Eder, 5. Synthesis strategies of nanocarbon hybrids, *Nanocarbon-Inorganic Hybrids*, De Gruyter 2014, pp. 125-70.

[51] A Cabrero-Vilatela, RS Weatherup, P Braeuninger-Weimer, S Caneva, S Hofmann, Towards a general growth model for graphene CVD on transition metal catalysts, *Nanoscale*, 8(2016) 2149-58.

[52] Y Xu, H Cao, Y Xue, B Li, W Cai, Liquid-phase exfoliation of graphene: an overview on exfoliation media, techniques, and challenges, *Nanomaterials*, 8(2018) 942.

[53] KS Novoselov, V Fal, L Colombo, P Gellert, M Schwab, K Kim, A roadmap for graphene, *nature*, 490(2012) 192-200.

[54] R Kumar, S Sahoo, E Joanni, RK Singh, WK Tan, KK Kar, et al., Recent progress in the synthesis of graphene and derived materials for next generation electrodes of high performance lithium ion batteries, *Progress in Energy and Combustion Science*, 75(2019) 100786.

[55] W-W Liu, S-P Chai, AR Mohamed, U Hashim, Synthesis and characterization of graphene and carbon nanotubes: A review on the past and recent developments, *Journal of Industrial and Engineering Chemistry*, 20(2014) 1171-85.

[56] W Gao, *Graphite oxide: Structure, reduction and applications* 2012.

[57] P Brisebois, M Siaj, Harvesting graphene oxide—years 1859 to 2019: a review of its structure, synthesis, properties and exfoliation, *Journal of Materials Chemistry C*, 8(2020) 1517-47.

[58] RK Mishra, Y Shalom, VB Kumar, JH Luong, A Gedanken, E Banin, Surfactant-free synthesis of a water-soluble PEGylated nanographeneoxide/metal-oxide nanocomposite as engineered antimicrobial weaponry, *Journal of Materials Chemistry B*, 4(2016) 6706-15.

[59] M Filice, JA Marchal, F Gamiz, Biosensors based on two-dimensional materials, *2D*

Materials for Nanophotonics, Elsevier 2021, pp. 245-312.

[60] MSA Bhuyan, MN Uddin, MM Islam, FA Bipasha, SS Hossain, Synthesis of graphene, *International Nano Letters*, 6(2016) 65-83.

[61] X-Y Wang, A Narita, K Müllen, Precision synthesis versus bulk-scale fabrication of graphenes, *Nature Reviews Chemistry*, 2(2017) 1-10.

[62] CM Pandey, BD Malhotra, 3. Nanomaterial-based Biosensors, *Biosensors*, De Gruyter 2019, pp. 37-62.

[63] RC Sinclair, JL Suter, PV Coveney, Micromechanical exfoliation of graphene on the atomistic scale, *Physical Chemistry Chemical Physics*, 21(2019) 5716-22.

[64] J Huang, M Yang, H Zhang, J Zhu, Solvent-free fabrication of robust superhydrophobic powder coatings, *ACS Applied Materials & Interfaces*, 13(2020) 1323-32.

[65] BV Chikkaveeraiah, AA Bhirde, NY Morgan, HS Eden, X Chen, Electrochemical immunosensors for detection of cancer protein biomarkers, *ACS nano*, 6(2012) 6546-61.

[66] AT Smith, AM LaChance, S Zeng, B Liu, L Sun, Synthesis, properties, and applications of graphene oxide/reduced graphene oxide and their nanocomposites, *Nano Materials Science*, 1(2019) 31-47.

[67] F Qing, Y Hou, R Stehle, X Li, Chemical vapor deposition synthesis of graphene films, *APL Materials*, 7(2019) 020903.

[68] S-H Chan, S-H Chen, W-T Lin, M-C Li, Y-C Lin, C-C Kuo, Low-temperature synthesis of graphene on Cu using plasma-assisted thermal chemical vapor deposition, *Nanoscale research letters*, 8(2013) 1-5.

[69] X Wu, Y Liu, H Yang, Z Shi, Large-scale synthesis of high-quality graphene sheets by an improved alternating current arc-discharge method, *RSC advances*, 6(2016) 93119-24.

[70] X Yu, C Hwang, CM Jozwiak, A Köhl, AK Schmid, A Lanzara, New synthesis method for the growth of epitaxial graphene, *Journal of Electron Spectroscopy and Related*

Phenomena, 184(2011) 100-6.

[71] H Huang, S Chen, A Wee, W Chen, Epitaxial growth of graphene on silicon carbide (SiC), Graphene, Elsevier 2014, pp. 177-98.

[72] S Park, RS Ruoff, Chemical methods for the production of graphenes, Nature nanotechnology, 4(2009) 217-24.

[73] N Singh, P Siwatch, J Kaushal, J Sharma, SK Tripathi, One-step green synthesis of reduced graphene oxide by electrochemical etching of carbon rods and effect of different bias voltages on the quality, Journal of Solid State Chemistry, 291(2020) 121537.

[74] B Xue, Y Zou, Y Yang, A UV-light induced photochemical method for graphene oxide reduction, Journal of Materials Science, 52(2017) 12742-50.

[75] A Ravi, MP Kumar, M Rekha, MS Santosh, C Srivastava, Graphene based nanocomposites: Synthesis, properties and application as electrochemical sensors, Comprehensive analytical chemistry, Elsevier 2020, pp. 1-20.

[76] JR Potts, DR Dreyer, CW Bielawski, RS Ruoff, Graphene-based polymer nanocomposites, Polymer, 52(2011) 5-25.

[77] J-Y Wang, S-Y Yang, Y-L Huang, H-W Tien, W-K Chin, C-CM Ma, Preparation and properties of graphene oxide/polyimide composite films with low dielectric constant and ultrahigh strength via in situ polymerization, Journal of Materials Chemistry, 21(2011) 13569-75.

[78] L-Z Guan, L Zhao, Y-J Wan, L-C Tang, Three-dimensional graphene-based polymer nanocomposites: preparation, properties and applications, Nanoscale, 10(2018) 14788-811.

[79] I Salimikia, R Heydari, F Yazdankhah, Polyaniline/graphene oxide nanocomposite as a sorbent for extraction and determination of nicotine using headspace solid-phase microextraction and gas chromatography–flame ionization detector, Journal of the Iranian Chemical Society, 15(2018) 1593-601.

[80] M Farajvand, K Farajzadeh, G Faghani, Synthesis of graphene oxide/polyaniline nanocomposite for measuring cadmium (II) by solid phase extraction combined with

dispersive liquid-liquid microextraction, *Materials Research Express*, 5(2018) 075017.

[81] DG Papageorgiou, IA Kinloch, RJ Young, Mechanical properties of graphene and graphene-based nanocomposites, *Progress in Materials Science*, 90(2017) 75-127.

[82] D Stankovich, Dikin, GHB Dommett, KM Kohlhaas, EJ Zimney, EA Stach, RD Piner, ST Nguyen, and RS Ruoff, *Nature*, 442(2006) 282.

[83] DG Papageorgiou, L Tzounis, GZ Papageorgiou, DN Bikiaris, K Chrissafis,  $\beta$ -nucleated propylene-ethylene random copolymer filled with multi-walled carbon nanotubes: Mechanical, thermal and rheological properties, *Polymer*, 55(2014) 3758-69.

[84] W Chee, H Lim, N Huang, I Harrison, Nanocomposites of graphene/polymers: a review, *Rsc Advances*, 5(2015) 68014-51.

[85] T Yu, P Zhu, Y Xiong, H Chen, S Kang, H Luo, et al., Synthesis of microspherical polyaniline/graphene composites and their application in supercapacitors, *Electrochimica Acta*, 222(2016) 12-9.

[86] SF Bartolucci, J Paras, MA Rafiee, J Rafiee, S Lee, D Kapoor, et al., Graphene-aluminum nanocomposites, *Materials Science and Engineering: A*, 528(2011) 7933-7.

[87] Z Li, G Fan, Z Tan, Q Guo, D Xiong, Y Su, et al., Uniform dispersion of graphene oxide in aluminum powder by direct electrostatic adsorption for fabrication of graphene/aluminum composites, *Nanotechnology*, 25(2014) 325601.

[88] L-Y Chen, H Konishi, A Fehrenbacher, C Ma, J-Q Xu, H Choi, et al., Novel nanoprocessing route for bulk graphene nanoplatelets reinforced metal matrix nanocomposites, *Scripta Materialia*, 67(2012) 29-32.

[89] M Rashad, F Pan, A Tang, Y Lu, M Asif, S Hussain, et al., Effect of graphene nanoplatelets (GNPs) addition on strength and ductility of magnesium-titanium alloys, *Journal of Magnesium and alloys*, 1(2013) 242-8.

[90] S Rikhtehgaran, A Lohrasebi, Water desalination by a designed nanofilter of graphene-charged carbon nanotube: A molecular dynamics study, *Desalination*, 365(2015) 176-81.

- [91] M Ramezani, M Alibolandi, M Nejabat, F Charbgo, SM Taghdisi, K Abnous, Graphene-based hybrid nanomaterials for biomedical applications, *Biomedical applications of graphene and 2D nanomaterials*, (2019) 119-41.
- [92] S-Y Yang, W-N Lin, Y-L Huang, H-W Tien, J-Y Wang, C-CM Ma, et al., Synergetic effects of graphene platelets and carbon nanotubes on the mechanical and thermal properties of epoxy composites, *Carbon*, 49(2011) 793-803.
- [93] Y Lin, S Liu, J Peng, L Liu, The filler–rubber interface and reinforcement in styrene butadiene rubber composites with graphene/silica hybrids: A quantitative correlation with the constrained region, *Composites Part A: Applied Science and Manufacturing*, 86(2016) 19-30.
- [94] DG Papageorgiou, IA Kinloch, RJ Young, Hybrid multifunctional graphene/glass-fibre polypropylene composites, *Composites Science and Technology*, 137(2016) 44-51.
- [95] J Knoll, BT Riecken, N Kosmann, S Chandrasekaran, K Schulte, B Fiedler, The effect of carbon nanoparticles on the fatigue performance of carbon fibre reinforced epoxy, *Composites Part A: Applied Science and Manufacturing*, 67(2014) 233-40.
- [96] E Mannov, H Schmutzler, S Chandrasekaran, C Viets, S Buschhorn, F Tölle, et al., Improvement of compressive strength after impact in fibre reinforced polymer composites by matrix modification with thermally reduced graphene oxide, *Composites Science and Technology*, 87(2013) 36-41.
- [97] H Ren, M Tang, B Guan, K Wang, J Yang, F Wang, et al., Hierarchical graphene foam for efficient omnidirectional solar–thermal energy conversion, *Advanced Materials*, 29(2017) 1702590.
- [98] W Lv, Z Li, Y Deng, Q-H Yang, F Kang, Graphene-based materials for electrochemical energy storage devices: opportunities and challenges, *Energy Storage Materials*, 2(2016) 107-38.
- [99] N Mahmood, C Zhang, H Yin, Y Hou, Graphene-based nanocomposites for energy storage and conversion in lithium batteries, supercapacitors and fuel cells, *Journal of*

Materials Chemistry A, 2(2014) 15-32.

[100] D Cohen-Tanugi, JC Grossman, Mechanical strength of nanoporous graphene as a desalination membrane, Nano letters, 14(2014) 6171-8.

[101] P-y Hung, K-t Lau, B Fox, N Hameed, B Jia, JH Lee, Effect of graphene oxide concentration on the flexural properties of CFRP at low temperature, Carbon, 152(2019) 556-64.

[102] Y Wu, L Huang, X Huang, X Guo, D Liu, D Zheng, et al., A room-temperature liquid metal-based self-healing anode for lithium-ion batteries with an ultra-long cycle life, Energy & Environmental Science, 10(2017) 1854-61.

[103] J Albero, D Mateo, H García, Graphene-based materials as efficient photocatalysts for water splitting, Molecules, 24(2019) 906.

[104] E-C Cho, J-H Huang, C-P Li, C-W Chang-Jian, K-C Lee, Y-S Hsiao, et al., Graphene-based thermoplastic composites and their application for LED thermal management, Carbon, 102(2016) 66-73.

[105] A Koutsioukis, V Georgakilas, V Belessi, R Zboril, Highly conductive water-based polymer/graphene nanocomposites for printed electronics, Chemistry—A European Journal, 23(2017) 8268-74.

[106] Y-R Liou, HY Lin, TL Shen, SY Cai, YH Wu, YM Liao, et al., Integration of nanoscale and macroscale graphene heterostructures for flexible and multilevel nonvolatile photoelectronic memory, ACS Applied Nano Materials, 3(2019) 608-16.

[107] SK Hazra, S Basu, Graphene-oxide nano composites for chemical sensor applications, C, 2(2016) 12.

[108] A Pandikumar, GTS How, TP See, FS Omar, S Jayabal, KZ Kamali, et al., Graphene and its nanocomposite material based electrochemical sensor platform for dopamine, Rsc Advances, 4(2014) 63296-323.

[109] X Sun, Z Liu, K Welsher, JT Robinson, A Goodwin, S Zaric, et al., Nano-graphene oxide for cellular imaging and drug delivery, Nano research, 1(2008) 203-12.



- [110] M Silva, NM Alves, MC Paiva, Graphene-polymer nanocomposites for biomedical applications, *Polymers for Advanced Technologies*, 29(2018) 687-700.
- [111] Y Wang, Z Li, J Wang, J Li, Y Lin, Graphene and graphene oxide: biofunctionalization and applications in biotechnology, *Trends in biotechnology*, 29(2011) 205-12.
- [112] S Patra, SK Swain, Graphene-based nanocomposites for biomedical engineering application, *Green Biocomposites for Biomedical Engineering*, Elsevier 2021, pp. 197-224.
- [113] M Šeruga, I Novak, L Jakobek, Determination of polyphenols content and antioxidant activity of some red wines by differential pulse voltammetry, HPLC and spectrophotometric methods, *Food Chemistry*, 124(2011) 1208-16.
- [114] X Fuku, F Iftikar, E Hess, E Iwuoha, P Baker, Cytochrome c biosensor for determination of trace levels of cyanide and arsenic compounds, *Analytica chimica acta*, 730(2012) 49-59.
- [115] B-Y Chang, S-M Park, Electrochemical impedance spectroscopy, *Annual Review of Analytical Chemistry*, 3(2010) 207.
- [116] S Kumar, CM Pandey, A Hatamie, A Simchi, M Willander, BD Malhotra, Nanomaterial-modified conducting paper: fabrication, properties, and emerging biomedical applications, *Global Challenges*, 3(2019) 1900041.
- [117] G Balkourani, T Damartzis, A Brouzgou, P Tsiakaras, Cost effective synthesis of graphene nanomaterials for non-enzymatic electrochemical sensors for glucose: a comprehensive review, *Sensors*, 22(2022) 355.
- [118] RS Tade, SN Nangare, PO Patil, Fundamental aspects of graphene and its biosensing applications, *Functional Composites and Structures*, 3(2021) 012001.
- [119] Y Song, CP Rampley, X Chen, F Du, IP Thompson, WE Huang, Application of bacterial whole-cell biosensors in health, *Handbook of Cell Biosensors*, (2022) 945-61.
- [120] J Patel, Introduction of Modified Fused Coumarin and Screening of Biological

Activity against Breast Cancer Cell Lines, *Adv Appl Sci Res*, 12(2021) 13.

[121] M Coccia, Pandemic prevention: lessons from COVID-19, *Encyclopedia*, 1(2021) 36.

[122] N Mukherjee, N Chatterjee, K Manna, KD Saha, Types of cancer diagnostics, the current achievements, and challenges, *Biosensor Based Advanced Cancer Diagnostics*, (2022) 27-45.

[123] M Hasan, M Ahommed, M Daizy, M Bacchu, M Ali, M Al-Mamun, et al., Recent development in electrochemical biosensors for cancer biomarkers detection, *Biosensors and Bioelectronics: X*, 8(2021) 100075.

[124] A Khanmohammadi, A Jalili Ghazizadeh, P Hashemi, A Afkhami, F Arduini, H Bagheri, An overview to electrochemical biosensors and sensors for the detection of environmental contaminants, *Journal of the Iranian Chemical Society*, 17(2020) 2429-47.

[125] X Sun, Q Zhao, C Zha, J Zhang, Z Zhou, H Dong, et al., Competitive Electrochemical Immunosensor for Detection of Capsaicinoids in Edible Vegetable Oil Based on Computer Aided Molecular Modeling, *Journal of The Electrochemical Society*, 169(2022) 057502.

[126] AA Ansari, BD Malhotra, Current progress in organic–inorganic hetero-nano-interfaces based electrochemical biosensors for healthcare monitoring, *Coordination Chemistry Reviews*, 452(2022) 214282.

[127] BD Malhotra, *Biosensors: fundamentals and applications: Smithers rapra*; 2017.

[128] ST Kumar, S Jagannath, C Francois, H Vanderstichele, E Stoops, HA Lashuel, How specific are the conformation-specific  $\alpha$ -synuclein antibodies? Characterization and validation of 16  $\alpha$ -synuclein conformation-specific antibodies using well-characterized preparations of  $\alpha$ -synuclein monomers, fibrils and oligomers with distinct structures and morphology, *Neurobiology of disease*, 146(2020) 105086.

[129] A Hagan, T Zuchner, Lanthanide-based time-resolved luminescence immunoassays, *Analytical and bioanalytical chemistry*, 400(2011) 2847-64.

[130] P Jackson, D Blythe, Immunohistochemical techniques, Theory and practice of histological techniques, 7(2008) 381-426.

# CHAPTER 2

## *Materials & Experimental Techniques*

---

### 2.1. Introduction

This chapter describes the materials used for the fabrication of GO and its nanocomposites-based biosensors for cancer biomarker detection employing the electrochemical technique. Further, various analytical techniques were employed for the characterization of the GO, rGO, rGO@TiO<sub>2</sub>, rGO@MoS<sub>2</sub> and different GO-modified electrodes. Besides this, the various techniques utilized to characterize these GO-based composites have also been discussed. The selection of suitable cancer biomarkers and their specific monoclonal antibodies to study the selectivity and specificity of the fabricated biosensors have also been briefly explained. Attempts have also been made to describe the procedures and protocols used to estimate various parameters related to the performance of GO-based nanocomposite for cancer biomarker detection.

### 2.2. MATERIALS

Details of the materials utilized while pursuing different experiments are as follows:

#### 2.2.1. Chemicals

(G) Graphite <20 μm CAS:7782-42-5, {(NH<sub>4</sub>)<sub>6</sub>Mo<sub>7</sub>O<sub>24</sub>·4H<sub>2</sub>O} ammonium molybdate ≥99.0% CAS: 12054-85-2 Fisher Scientific, (H<sub>2</sub>SO<sub>4</sub>) concentrated sulfuric acid ~ 98% CAS: 7664-93-9 Fisher Scientific, (HCl) hydrochloric acid ~ 36.46% CAS: 7647-01-0 Fisher Scientific, (H<sub>2</sub>O<sub>2</sub>) hydrogen peroxide ~ 30% CAS: 7722-84-1 Central drug house, (NaNO<sub>3</sub>) sodium nitrate ~ 99% CAS: 7631-99-4 Fisher, (KMnO<sub>4</sub>) potassium permanganate ≥99% CAS: 7722-64-7, (Mg(NO<sub>3</sub>)<sub>2</sub>·6H<sub>2</sub>O) magnesium nitrate hexahydrate ~ 99% CAS: 13446-18-9, (L-cys) L-cysteine ~ 97% CAS: 52-90-4, (TBOT) tetrabutyltitanate ~ 97% CAS:5593-70-4, C<sub>4</sub>H<sub>10</sub>O<sub>3</sub> diethylene glycol ~ 99% CAS: 111-46-6, (EDC) N-ethyl-N'-(3-dimethyl aminopropyl) carbodiimide CAS: 25952-53-8, (BSA) bovine serum albumin ≥98% pH=7 CAS: 9048-46-8, (Anti-BSA) monoclonal anti bovine

serum SKU: B2901, (NHS) N-hydroxy succinimide ~ 98% CAS: 6066-82-6, (ITO) indium tin oxide, coated glass purchased from Technistro. All other solvents and reagents of analytical grade were purchased from Sigma-Aldrich with monoclonal antibodies (anti-EpCAM) and antigen (EpCAM). All materials were synthesized with deionized (DI) water (Mill-Q, Millipore, 18.2 M $\Omega$  cm). The glasswares, voils were purchased from borosil and autoclaved before use.

### **2.2.2. Buffers and solutions**

- Tris–EDTA buffer (TE), pH 8 (10 mM Tris–HCl and 1 mM EDTA)
- 100 mM Phosphate buffer saline (PBS), pH 7.4, 0.9% sodium chloride (NaCl)
- 5 mM [Fe(CN)<sub>6</sub>]<sup>3-/4-</sup> in PBS solution as redox indicator
- PBS buffer containing 0.1% sodium azide
- PBS buffer containing 50% glycerol solution

### **2.3. Characterization techniques**

This thesis includes the work related to (1) preparation of GO, rGO, and rGO@TiO<sub>2</sub> and rGO@MoS<sub>2</sub> nanocomposites followed by their film fabrication onto ITO coated glass plates and (2) immobilization of monoclonal antibodies (anti-EpCAM) onto rGO nanocomposites based electrodes to explore their applications for cancer biomarker detection. At various stages of preparation, these fabricated electrodes/bioelectrodes have been characterized by using various techniques like Fourier transform infrared (FT-IR) spectroscopy, Raman spectroscopy, UV-Visible (UV-Vis) spectroscopy, Scanning electron microscopy (SEM), Transmission electron microscopy (TEM), X-ray diffraction (XRD), Atomic force microscopy (AFM), Electrochemical techniques such as Cyclic voltammetry (CV), Differential pulse voltammetry (DPV), and Electrochemical impedance spectroscopy (EIS).

#### **2.3.1 Fourier Transform Infrared (FT-IR) spectroscopy**

The interaction of electromagnetic radiation with a chemical system is the fundamental basis of infrared spectroscopy. The molecules absorb electromagnetic radiation from the

light beam and produce various spectral lines. The spectrum is essentially determined by the chemical bonds that exist between the atoms of a molecule. The spectrum can be caused by vibration, rotation, or their combination. The frequency of such movements occurs in the electromagnetic spectrum's infrared region [1]. As a result, IR spectroscopy is employed to investigate the information on chemical bonding in the substance. The IR spectrum contains all the information about the analyzed sample's "functional groups, chemical bonds, stoichiometry, and so on, and may thus be referred to as the material's molecular finger print". This is a non-destructive approach that may be used to investigate any sort of sample. The approach is quick, sensitive, and simple to use, and it allows for convenient qualitative and quantitative examination of the spectra. All FT-IR spectrometers are based on the Michelson interferometer where a beam-splitter divides the beam into two parts as shown in Fig. 2.1. An infrared spectrometer is made up of three key components: (a) the source, which is a filament (a silicon carbide element) that is kept at red or white heat by an electric current.

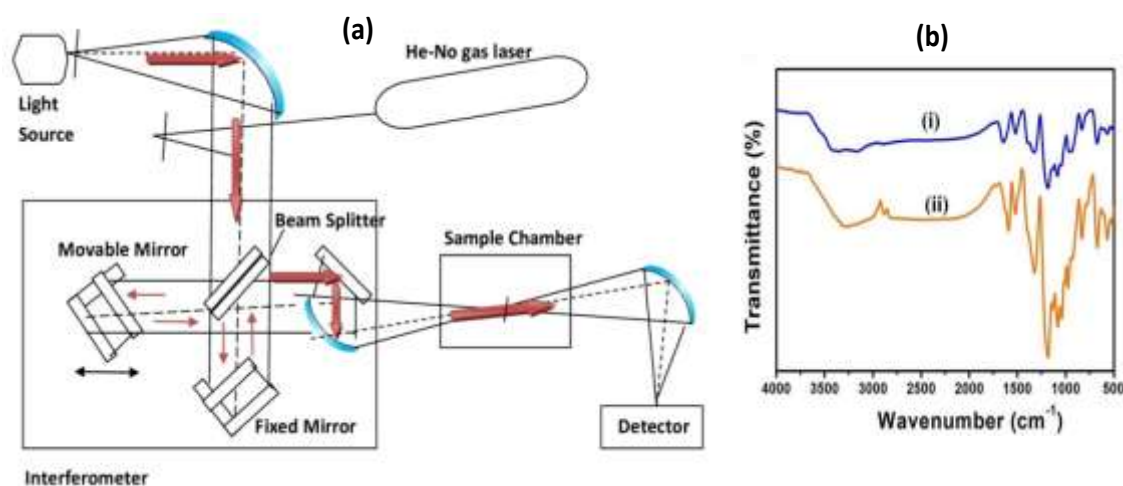


**Figure 2.1** (a) Schematic of the optical layout of Michelson Interferometer (b) FTIR spectra of (i) rGO@CP electrode (ii) rGO-TiO<sub>2</sub>@CP electrode.

Michelson interferometer is the most frequent interferometer used in FTIR spectroscopy. The IR radiation is either transmitted or reflected when it reaches to the beam-splitter. The 50% intensity of the radiation beam will hit either a stationary or moving mirror and it is

reflected back to the beam splitter where the beam interaction might take place. When the radiation reaches the detector, it fluctuates due to the movement of the moving mirror. The fluctuation might be destructive or constructive depending on the distance of the moving mirror. (c) Detector: two types of detectors are commonly employed, "one that detects the radiation's heating impact and the other that relies on photoconductivity". In both the cases, the stronger the impact (temperature or conductivity rise) at a specific frequency, the higher the sample's transmittance (and lower its absorbance) at that frequency in an FTIR spectrometer, an interferogram is recorded first in the absence of a sample and then in the presence of a sample to trace the spectrum. The computer performs Fourier transforms on the recorded data, and the ratio of sample and background data is displayed as a transmittance spectrum. The Fourier transform offers several advantages over dispersive measurements, including the ability (i) to record the whole spectrum throughout the entire frequency range at once, whereas with "dispersive IR, the grating must be changed because one grating cannot be effective across the entire range". (ii) When compared to dispersive IR, recording FTIR spectra takes less time. (iii) In a Fourier transform system, because parallel beams are used and focusing is required at the sample and detector, there is no need for a slit, and all of the source energy passes through the instrument only, allowing for the use of less noisy amplifiers, whereas in a dispersive system, noisy amplifiers are required. (iv) Resolving power that remains constant over the whole spectrum. (v) Accurate frequency measurement owing to an exact knowledge of the laser's frequency [2].

**Fig. 2.1(b)** shows a typical FT-IR spectrum of (i) rGO@CP electrode (ii) rGO-TiO<sub>2</sub>@CP electrode, which shows the presence of various oxygenated functional groups. In the present thesis, the FT-IR technique has been used to investigate the presence of various functional groups of GO (**Chapter-III**) and its nanocomposites with TiO<sub>2</sub> (**Chapter-IV**) and MoS<sub>2</sub> (**Chapter-V**). FT-IR analysis reveals the presence of carboxylic acid groups in rGO that has been utilized for covalent immobilization of antibodies. FT-IR spectrum of

the desired sample has been recorded by Perkin Elmer Instrument; Model Spectrum BXII (**Fig. 2.1**). The FT-IR spectrum of each sample is recorded over 64 scans with  $1\text{cm}^{-1}$  resolution. The pellets ( $\sim 1\text{cm}$  diameter) of solid samples have been prepared by mixing it with KBr.

### **2.3.2 Raman spectroscopy**

The phenomena of Raman spectroscopy are based on the inelastic scattering called as Raman effect. The effect of light on molecular vibrations allows chemical compound identification of the material. In Raman spectroscopy, a strong laser beam radiation of a definite frequency is passed through a transparent substance. The dispersed light is transmitted via a filter “after the laser light has irradiated the material”, to get rid of any light from the excitation laser. The light is then focused onto a grating (which distributes the inelastic regions like a prism and according to wavelength). These beams are then directed to a charge-coupled device sensor, which produces a spectrum based on the intensity (**Fig. 2.2**). Numerous “bands or signals” can be seen in the Raman spectrum because several molecules, as well as substances, have their own set of characteristics. They reveal info on the substance's chemical components, as well as crystallinity, polymorphism, temperature and pressure changes [3]. The D/G intensity ratio and variations in the  $\text{sp}^2$  hybridization pattern were investigated using Raman spectra to describe the produced graphene oxide (GO), reduced graphene oxide (rGO), GO nanocomposite with  $\text{TiO}_2$  and  $\text{MoS}_2$  as reported in Chapter V.



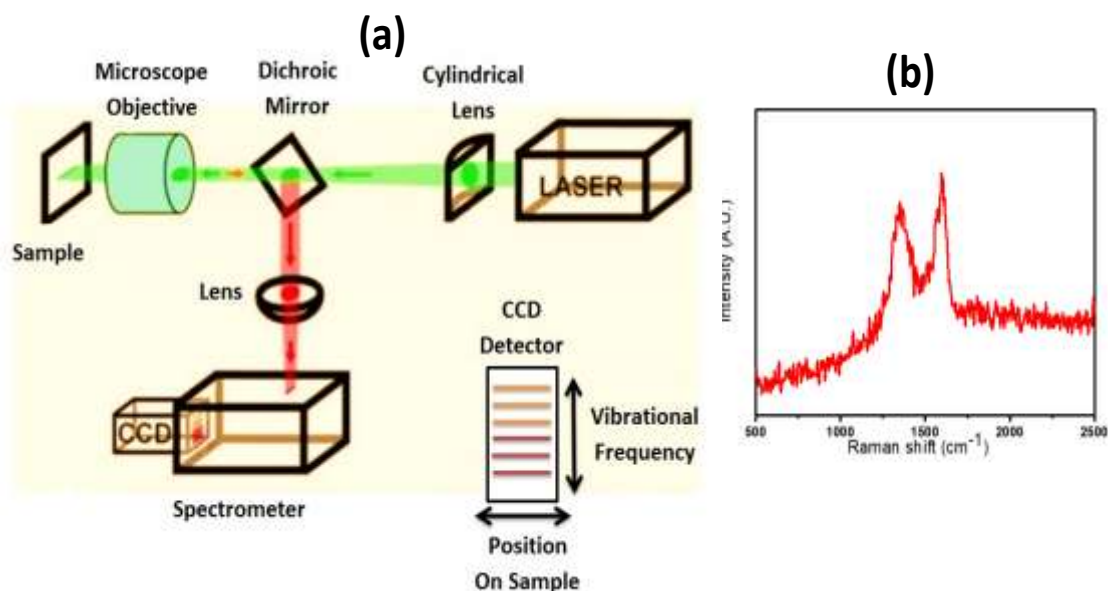


**Figure 2.2** (a) Schematic representation of Raman spectroscopy (b) Raman spectra of GO

The study was carried out using an Ar (argon-ion) and 514 nm, 50 mW (laser). The experiment was conducted at room temperature with a micro-Raman spectrometer (range of 100-3500  $\text{cm}^{-1}$ ). The D band comprises  $\text{sp}^3$  carbon atoms or defects in graphene sheets, whereas the G band is made up of in-plane vibrations of  $\text{sp}^2$  carbon atoms;  $I_d/I_g$  (Peak intensity) increases when the GO is reduced. For example, GO with an  $I_d/I_g$  of 0.8 can be transformed to rGO with an  $I_d/I_g$  of 1.0 or higher. On reduction of GO to rGO, the intensity ratio of the D to G band ( $I_d/I_g$ ) increases due to the removal of oxygen functionalities and the formation of defects inside layers.

### 2.3.3 Ultraviolet-Visible (UV-Vis) spectroscopy

UV-vis spectroscopy is used to analyze electron exchanges between orbitals or bands of atoms, ions, and molecules. The sample absorbs a portion of the incident light in the UV-Vis spectrometer, while the remaining light passes to the detector as depicted in **Fig. 2.3**. The transmitted radiation is then converted to an electrical signal, which is amplified before it goes to the detector [4]. UV-Vis spectroscopy has been utilized for the optical characterization of GO, rGO and rGO@TiO<sub>2</sub> nanocomposite. UV-Vis analysis of GO, rGO has been described in **Chapter-III**. In **Chapter-IV**, UV-Vis studies have been conducted to reveal the transformation of GO to rGO. The optical studies have been carried out using a

UV–Vis spectrophotometer (Model160A, Shimadzu) (Fig. 2.3).

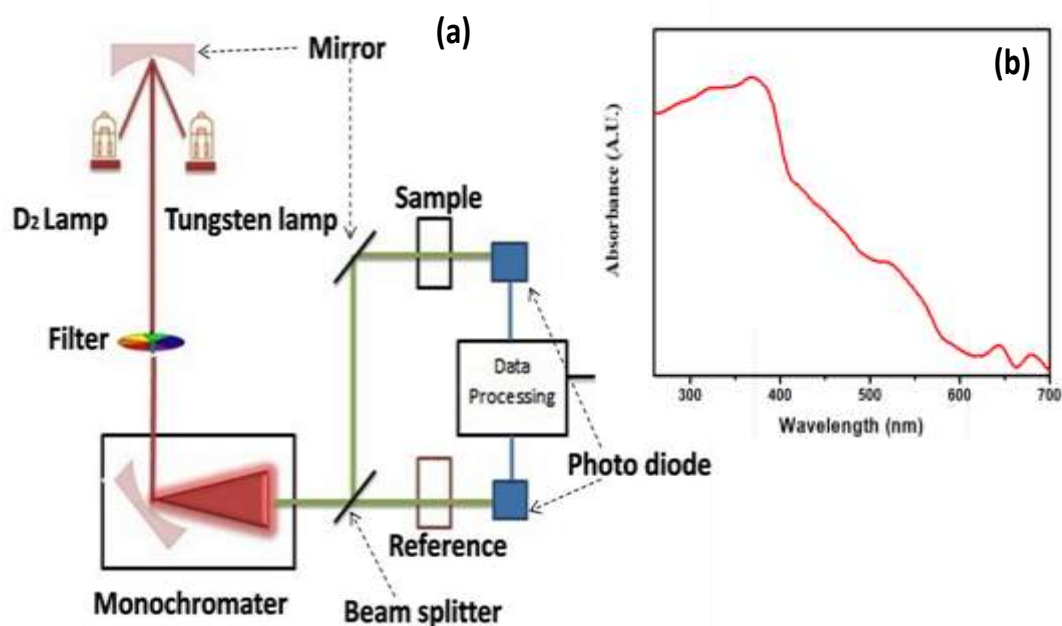


**Figure 2.3** (a) Schematic of dual-beam UV-Vis spectrophotometer (b) UV -Vis spectra of rGO-MoS<sub>2</sub>

Some of the precautions must be taken before handling the instrument, i.e., touching the optical assembly with bare hands is not recommended. To avoid unpredictable readings, the optical surface of cuvettes should not be handled with fingers. To eliminate solvent interference, a background spectrum should be collected prior to sample analysis. Before using the instrument, double-check the calibration status and make sure it's up to date.

### 2.3.4 Thermogravimetric analysis (TGA)

Gravimetric analysis is a field derived from the process of isolating and weighing an element or a particular compound in the purest form, possibly has been characterized as quantitative analysis by weight. Thermogravimetry (TG) is a method in which the mass of a sample is measured versus time or temperature, while the sample's temperature in a controlled environment is regulated. It should be noted that this approach is also known as thermogravimetric analysis (TGA). The equipment has a broad isothermal zone, which allows for the great temperature repeatability. Aside from these accelerated furnace cooling facilities, which use water from the tap and integrated forced air. The nitrogen (N<sub>2</sub>) gas was purged to maintain a consistent inert atmosphere in TGA. The balance is protected

by this purge gas, which shields it from the reactive sample purge gas as well as the components emitted by the sample. The change in weight of the sample is measured using a microbalance [5]. A separated pipeline for purge gas and cooling with full schematic representation is shown in **Fig. 2.4**.

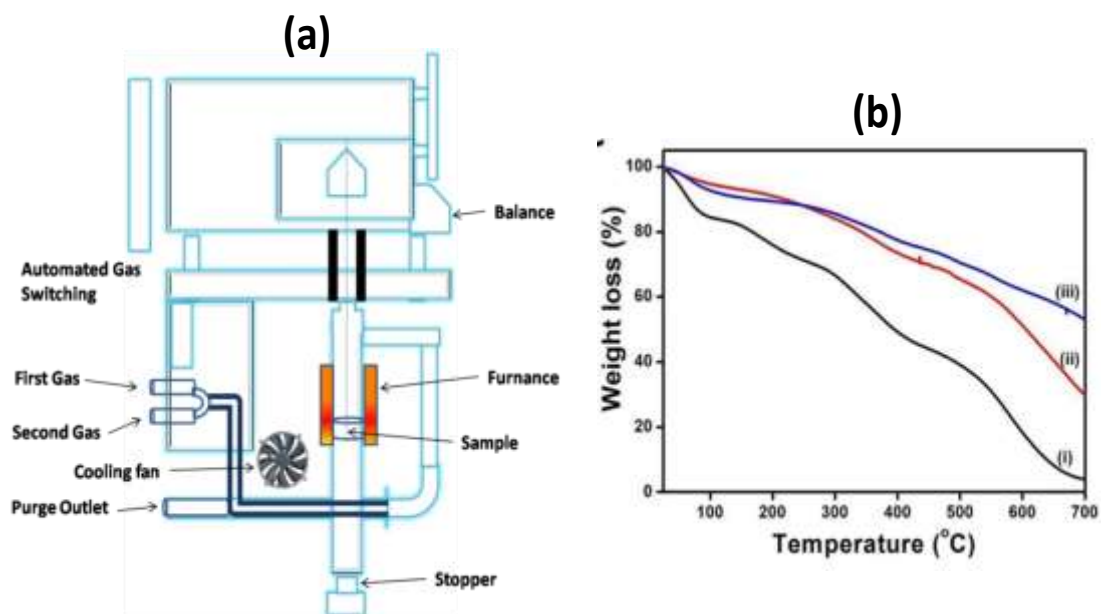


**Figure 2.4** (a) Schematic representation of thermogravimetric analysis (TGA) (b) TGA thermogram of (i) PEDOT:PSS (ii) PEDOT:PSS/rGO nanohybrid and (iii) PEDOT:PSS/rGO@TiO<sub>2</sub> nanohybrid

The method is only relevant to transitions involving the absorption or evolution of gases from a condensed phase material. The vast majority of TG devices are set up for vacuum and/or changing atmospheres. The TG-related balances are extremely sensitive. The temperature of decomposition and the weight loss associated with it are provided by TG. Dehydration (absorbed or crystal water), thermal breakdown, and/or thermal stability of materials, among other things, are studied by using TGA.

### 2.3.5 Differential Scanning Calorimetry (DSC)

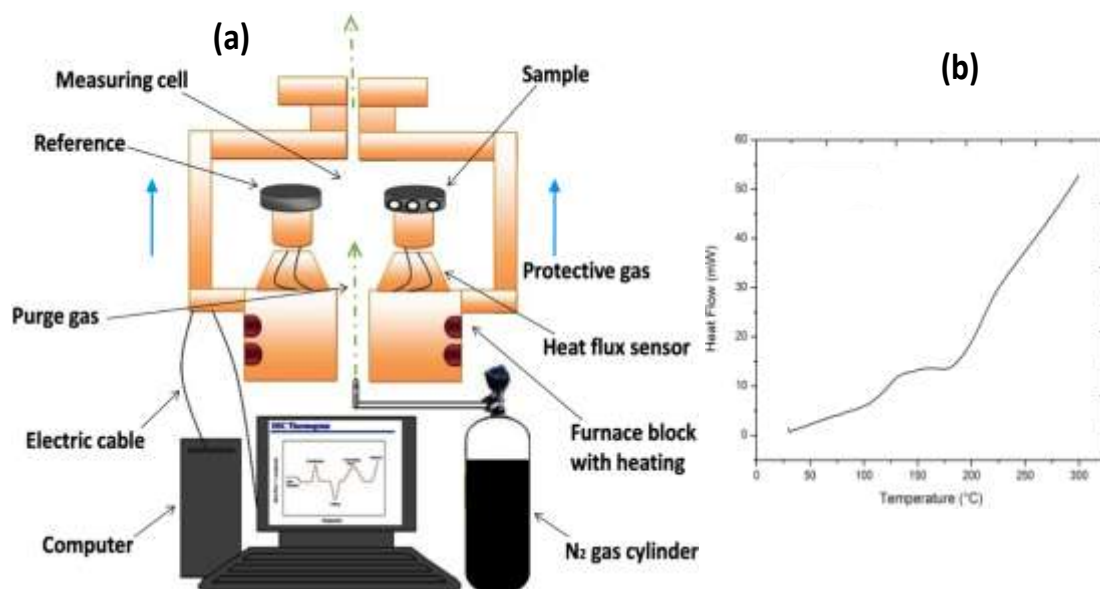


**Figure 2.5.** (a) Schematic working of the DSC apparatus (b) DSC thermogram of GO

The DSC monitors the temperatures and heat flows that occur as a result of a material's thermal transitions. Heat capacity at various temperatures, glass transition parameters, phase shifts (melting, crystallization), product stability, and cure kinetics are all properties studied using DSC technique. For GO, and rGO@TiO<sub>2</sub>, rGO@MoS<sub>2</sub> nanocomposite, the glass-transition temperatures were measured using a DSC Q20 Modulate (TA Instruments, -80°C up to 400 °C). The DSC scans were recorded using roughly 2 mg of samples at a ramp rate (heating rate) of 10 °C/min, in the temperature range 40 to 300 °C. A detailed schematic presentation of the DSC machine is shown in **Fig. 2.5** [6].

### 2.3.6 X-ray diffraction (XRD)

X-ray diffraction technique is generally used for the identification of unknown crystalline sample to determine its chemical composition and phase identification. This technique is used to analyze the crystalline size (grain size), crystallographic structure and probable orientation in polycrystalline or powder solid sample. This may also be used to analyze the heterogeneous solid mixture to determine the relative abundance of crystalline compound. When coupled with lattice refinement technique such as relative refinement it can provide the structural information of unknown sample.

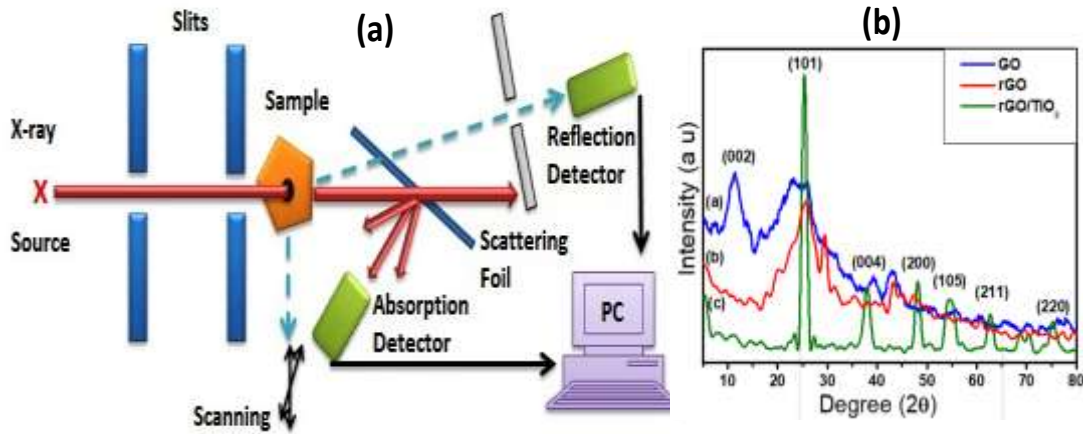


**Figure 2.6** (a) Schematic representation of XRD (b) XRD spectra of GO, rGO, rGO/TiO<sub>2</sub>

XRD patterns are recorded by using X-ray diffractometer. The peak broadening data were obtained by measuring an average of peak broadening in five most strong diffraction peaks. Here, the mean size of the nanoparticles may be determined from the peak broadening in the X-ray diffraction pattern with the help of Debye-Scherrer equation. In addition, the particle size of nanoparticles and encapsulated nanoparticles by the conducting polymers is calculated according to the Debye-Scherrer equation (Eq. 2.1) [7, 8].

$$D = \frac{0.9\lambda}{\beta \cos\theta} \quad (2.1)$$

Where  $D$  is the average crystallite size (Å),  $\lambda$  is the wavelength of X-rays (Cu K $\alpha$ :  $\lambda = 1.5418$  Å),  $\theta$  is the Bragg's diffraction angle, and  $\beta$  is the full width at half maximum (FWHM; in radians) [7, 8]. An X-ray diffractometer (Bruker, model D8) has been used to analyze the crystalline phase and size of the nanomaterials (Fig. 2.6). The scanning rate of 0.01°/step with the integration time of 8 sec/step has been utilized with an X-ray radiation source with a wavelength of 1.54 Å, an aperture slit with a width of 0.1 mm. The powdered samples were employed in the experiment. XRD studies have been used to identify the formation of GO, rGO, TiO<sub>2</sub> (**Chapter III**) and the composite of rGO with MoS<sub>2</sub> (**Chapter IV**).

### 2.3.7 Scanning Electron Microscopy (SEM)

The scanning electron microscope (SEM) is one of the most powerful equipment for examining and analyzing the morphology [9]. The SEM microscope generates a large number of signals at the surface of solid objects by using a high energy electrons beam. The signals produced by scattered electrons give the details of a sample such as the exterior texture (morphology), crystalline structure, and orientation of the sample. In most of the applications, the data have been collected across a certain region of the surface of sample. A two-dimensional (2D) picture displaying spatial changes of such attributes is created.

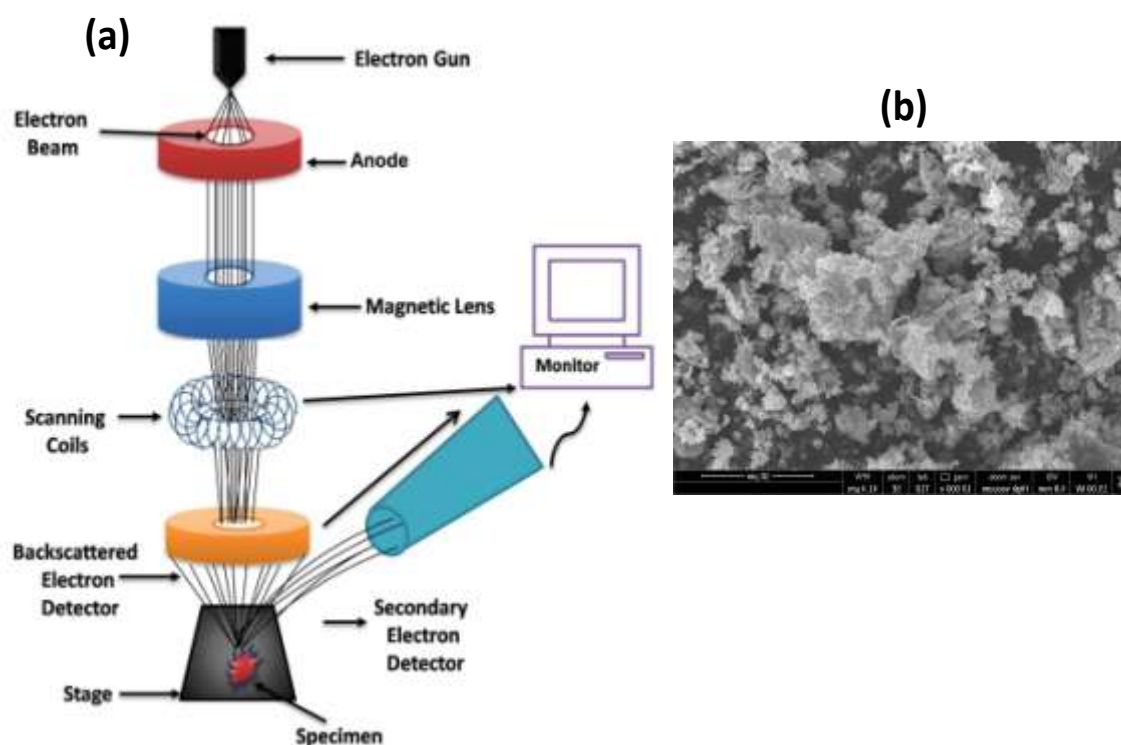


**Figure 2.7.** (a) Schematic representation of scanning electron microscope (b) SEM image of rGO/TiO<sub>2</sub>/MoS<sub>2</sub>

The diffracted electron is used to identify the crystal structure and orientation and the image produced by SEM is possible due to the secondary electron signal [10]. The scheme of SEM is shown in **Fig. 2.7**. To overcome low sample conductance in SEM, a few layers of broad gold coating must be deposited before analysis to improve the resolution. In the present work, SEM was used to examine the morphology of nanoparticles such as GO,

rGO, TiO<sub>2</sub> (Chapter III), MoS<sub>2</sub>, rGO@MoS<sub>2</sub>, as well as the fabricated electrode surface, before and after enzyme immobilization.

### **2.3.8 Transmission Electron Microscopy (TEM)**

Transmission Electron Microscopy (TEM) technique utilizes the energetic electrons to give the morphological, compositional and crystallographic informations of the samples under investigation. The high voltage electron beam is applied to the specimen and transmission of the unscattered electrons is monitored, which is inversely proportional to the specimen thickness. Thicker parts allow lesser number of electrons to transmit and thus will appear darker on hitting the fluorescent screen, when compared to the thinner counterparts of the same specimen. The obtained final image is displayed in real time on the computer monitor [11]. In general, the TEM offers the two modes, i.e., image and diffraction for studying a desired specimen. The image mode contrast must be induced in order to produce the image for analysis. While in the diffraction mode, the pattern of the diffracted electrons is obtained from the electron illuminated sample. When the electron beam is incident on the sample, the scattering events occur as all the illuminated parts of the sample act as the scattering sources. Interference causes coherently scattered beams when Bragg's law is being fulfilled. These coherently scattered beams are recorded in the form of a spot. It provides the information about the crystalline and crystal orientation.

A carbon coated copper TEM grid was used to mount the samples. After transferring the film onto a carbon coated copper grid, a 200 kV accelerating voltage is utilized to analyze the rGO layer arrangement on TiO<sub>2</sub>/MoS<sub>2</sub> hierarchical structures. The solvent for TEM analysis should be chosen in such a way that it will not harm the grid or interfere with the sample. The electron beam's energy must be adjusted to the sample's requirements.



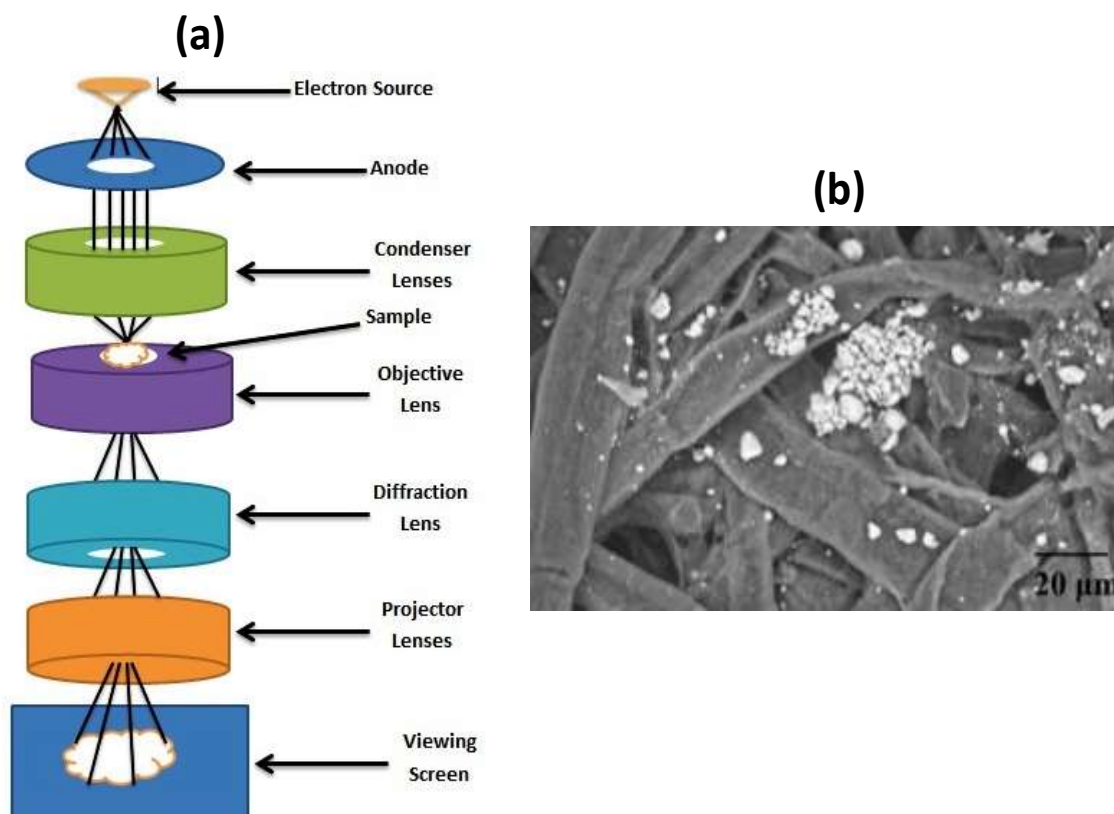


**Figure 2.8** (a) A pictorial view of scanning electron microscope (b) TEM image of rGO

TEM has a wide magnification range and diffract in a single sample. A TEM has three primary components such as a lighting system, a specimen stage, and an imaging system. An electron gun as well as two or more condenser lenses to concentrate the electrons onto the specimen, makes up the lighting system. The design and operation of lighting system determine the diameter of the electron beam on specimen as well as the intensity level in the picture of TEM. The specimen is held in a stationary or moved stage because the spatial resolution of the TEM picture is determined by the mechanical stability of this stage, it is critical. At least three lenses are used in the imaging system to generate a diffraction pattern (or magnified picture) of the sample on a “fluorescent screen, photographic film, or an electronic camera system's monitor screen”. The magnification of the TEM picture is determined by this imaging system's functioning, whereas the spatial resolution of the microscope is often determined by its design [12]. The middle lens is focused on the image plane of the objective lens, and electron rays are supposed to go straight down the microscope (parallel to the optic axis) before reaching the specimen. These rays are transmitted and diffracted by the specimen and merged on the viewing



screen to generate a picture. The schematic diagram of TEM is shown in Fig. 2.8.

### 2.3.9 Zeta potential

The electrical potential at a sliding plane is known as zeta potential. This sliding plane is the interface which divides the fluid (mobile) from the fluid that is still connected to the surface.

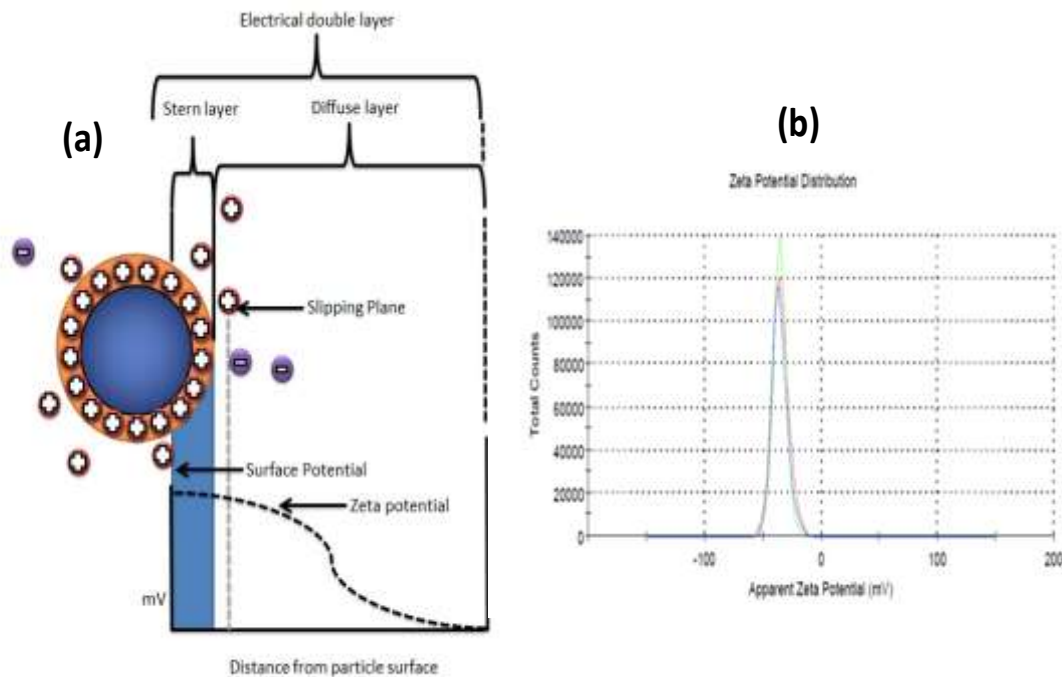


**Figure 2.9** (a) Schematic of Zeta potential (b) Zeta potential plot of rGO:TiO<sub>2</sub>:MoS<sub>2</sub> composite

The scientific terminology for electrokinetic potential in colloidal dispersions is the zeta potential. It is an electric potential at interfacial double layer (DL) on the site of sliding plane relative to a point in the bulk fluid distant from interface, according to theory. The zeta potential may also be defined as the change in potential between dispersion medium and stationary layer of fluid which is linked to the dispersed particles/nanoparticles. It is created by the total electrical charge present inside the region defined by the sliding plane which is affected by its position as well. It is often used to quantify the charge amount. However, the zeta potential is not identical to the electric surface potential in the DL, because these are defined at distinct locations. The pH is the most critical factor influencing zeta potential. Particles having zeta potentials,  $> +30$  mV or  $> -30$  mV are

typically regarded as stable as shown in **Fig. 2.9**. The zeta potential is a useful and easily measured indication of colloidal dispersion stability [13]. The zeta potential reflects the degree of electrostatic repulsion in the dispersion between nearby identical charged particles. A higher value of zeta potential promotes the stability to the molecules/particles of sufficient size because the solution or dispersion will resist the aggregation. Whenever the potential value is low, the forces of attraction can overcome the repulsion and the dispersion to break off resulting to agglomerate. The colloids having a negative or positive high zeta potential are found to be electrically stable whereas these may agglomerate in case of low zeta potential.

### 2.3.10 Electrochemical techniques

Electrochemistry is an analytical technique used to measure the potential, charge or current to determine the concentration or chemical reactivity of an analyte. The electrochemical techniques deal with the processes taking place in a system on the application of electric potential. In most of the electrochemical techniques, there is a cell assembly which contains three electrodes such as working electrode (WE), the reference electrode (RE) and the counter (or auxiliary) electrode (CE). These electrodes are well connected to an instrument, namely, a potentiostat which controls the potential of the working electrode and it measures the corresponding current response. In this type of electrochemical study, the potential is applied to the working electrode and the current response is plotted against time. While in other case, the potential is changed linearly and the resulting current is plotted versus the potential applied. In the electrolytic solution, the equilibrium concentrations of both the reduced and oxidised forms of a redox system are directly linked to the potential ( $E$ ) as per the Nernst's equation (**Eq. 2.2**).

$$E = E_o + \frac{RT}{nF} \ln \frac{C_{oxi}}{C_{red}} \quad (2.2)$$

Where  $E_o$  is the equilibrium,  $F$  the Faraday's constant,  $T$  an absolute temperature,  $C_{oxi}$  and  $C_{red}$  are the concentrations of oxidation and reduction domains. In accordance to the

Nernst's equation, the redox system present at electrode adjust their concentration ratios, if the potential is applied to the working electrode. The signal transduction and electrochemical performance (CV and DPV) of sensors have been studied using **Autolab (EcoChemie, Netherlands) Potentiostat/Galvanostat** with Ag/AgCl (saturated with KCl,  $E = +0.197$  V) as the RE and platinum (Pt) as the CE. An accurately determined and maintained potential is produced by a potentiostat by employing DC power source and drawing small currents at constant voltage into the system.

### 2.3.10.1. Cyclic Voltammetric (CV) measurements

CV is one of the most oftenly used electro-analytical methods for characterizing the electrochemical behavior of electrochemically active species. The working electrode potential is swept with time in a CV studies [14]. After reaching the set point, the working electrode potential is swept in the opposite direction and returned to its starting value. These potential cycles can be swept as required to generate a cyclic voltammetry graph. Cyclic voltammetry is applied to get the informations of electrochemical reactions between the electroactive species bearing a known reduction-oxidation potential. Since the counter electrode conducts the electricity from signal source to the working electrode, the current is monitored at the working electrode against a constant reference electrode potential during the potential scans. In order to provide ions to the electrodes, the electrolytic solution is used during the redox process.

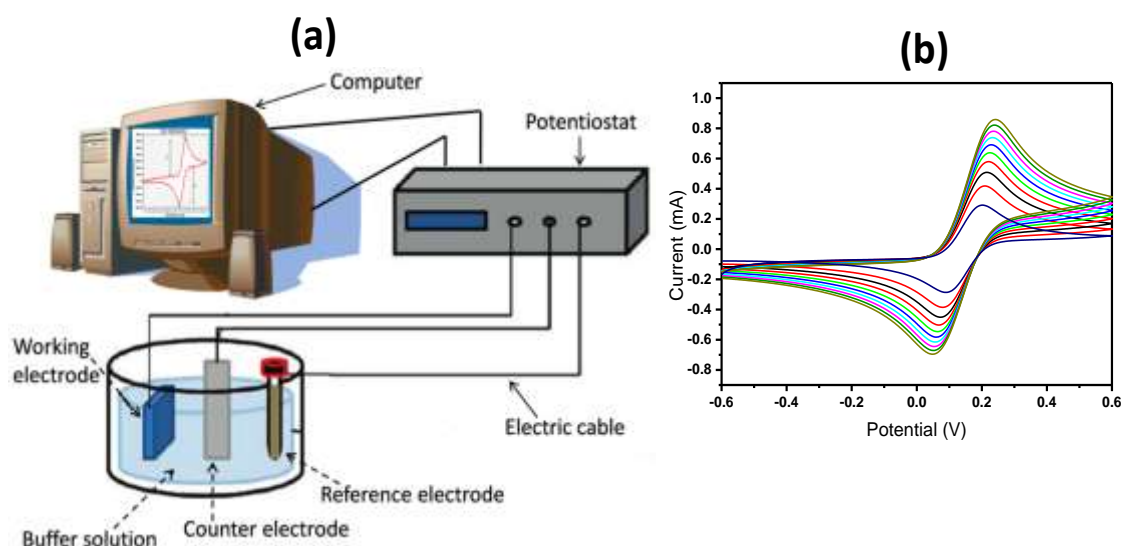


**Figure 2.10** (a) Working scheme of potentiostat (b) Scan rate (10-100 mV/s) studies of GO in PBS (100 mM, pH 7.0, 0.9% NaCl) containing 5 mM  $[\text{Fe}(\text{CN})_6]^{3-/4-}$

### 2.3.10.2. Differential Pulse Voltammetry (DPV)

The DPV provides superior detection limits, if compared to CV and it allows the resolution of more closely spaced electrode processes. Here, the potential versus time program is applied to the electrode with a linearly increasing ramp. The series of small amplitude pulses are superimposed onto ramped voltage and then resulting current is measured between the ramped baseline voltage and the pulse voltage. The current is measured at two points for each pulse. The first point is just before the pulse application while the second point lies at the pulse end. Moreover, these points are selected in such a way to let the non-faradaic (charging) current to decay. The difference between the current measurements at these points for each pulse is recorded against the base potential. The improved detection limit of DPV over CV and other voltammetric methods is due to superior discrimination against charging current and impurity Faradic currents [15].

### 2.3.10.3 Electrochemical Impedance Spectroscopic (EIS) measurements

EIS is a non-destructive technique for analyzing electrical characteristics of materials and conducting electrode interfaces [16]. The capacity of a circuit element to resist the passage of electrical current is defined by the Ohm's law. In most of the cases, an electrochemical impedance is determined by providing the AC voltage to an electrochemical cell and detecting the current flowing through it. It is expected that a sinusoidal potential excitation was used. An AC signal is produced in response to this potential. In order to get a pseudo-linear response of the electrochemical cell, electrochemical impedance is generally measured using a minor excitation signal. The matching current in a linear system with an applied sinusoidal potential is similar sinusoidal at the same frequency with a phase shift. In a linear system, the current response is sinusoidal. By modeling the impedance data in terms of  $R_s$  (solution resistance),  $R_{ct}$  (charge transfer resistance), and  $C_{dl}$  (double layer capacitance), is used to derive physically significant features of the electrochemical system

also include  $Z_w$  (Warburg element), which is used to display the cell's diffusion or mass transport impedance [17]. The Nyquist plot is used to illustrate the equivalent circuit model EIS data for electrochemical cells. The imaginary impedance that corresponds to the capacitive and inductive properties of the electrochemical cell is shown in a complex plane or Nyquist plot. During the charge transfer at the interface, the mass transports of the reactant and product take on roles in measuring the electron transfer rate which depends on the consumption of the oxidants and reductants release around the electrode surface. The mass transport of the reactants and the products gives another class of impedance ( $Z_w$ ) which is explored by the electroanalytical chemists due to the presence of peak current in a voltammogram or current plateau in a polarogram.

## **2.4 Methods to immobilize antibodies to the GO based matrix**

While immobilizing an antibody molecule to the matrix, it is important to choose an appropriate method for its attachment to prevent its denaturation. Thus, the chemical nature or reactive groups in the binding site of an antibody should not be influenced. Different methods can be utilized to immobilize the desired antibody molecules onto GO based matrix are discussed below.

### **2.4.1 Covalent immobilization**

Covalent immobilization is the most intensely explored immobilization technique. In this technique, the covalent bonding takes place between the biomolecule and a support matrix. This method is applicable for the matrices which contains the nucleophilic functional groups, such as  $-NH_2$ ,  $-SH$ ,  $-OH$  etc., capable of covalent coupling or being activated to give such groups which can be utilized to bind with the biomolecule. In this case of covalent immobilization, the binding force between an enzyme and matrix is very strong so that no leakage of enzymes may occur even in the presence of substrate or high ionic strength solution. Considering the presence of  $-COOH$  groups in the synthesized GO based matrix with strong and selective nature of this immobilization method, we have employed EDC-NHS protocol to covalently immobilize antibodies (anti-EpCAM) onto the

GO modified matrix (**Chapter III, IV&V**). This immobilization method involves the formation of amide linkage between NH<sub>2</sub> group of aminated antibodies and COOH group of GO using EDC (0.4M) as a coupling agent and NHS (0.1 M) as an activator.

## **2.5 Protocols to estimate various parameters relating to the performance of rGO nanocomposites based Immuno-biosensor**

### **2.5.1. Diffusion coefficient and electron transfer rate constant**

The peak current for a reversible redox process (at 25°C), is given by **Randles-Sevcik equation (Eq. 2.3)** as given below.

$$I_p = 2.69 \times 10^5 n^{3/2} ACD^{1/2} \nu^{1/2} \quad 2.3$$

Where,  $n$  is the number of electrons,  $A$  is the electrode area (cm<sup>2</sup>),  $C$  is the concentration (molcm<sup>-3</sup>),  $D$  is the diffusion coefficient (cm<sup>2</sup>s<sup>-1</sup>), and  $\nu$  is the scan rate (Vs<sup>-1</sup>). As per the equation, the current is directly proportional to the concentration which increases with an increase in square root of the scan rate. Thus, the diffusion coefficient of redox species can easily be obtained by using Randles-Sevcik equation.

### **2.5.2. Linear detection range, sensitivity and detection limit**

The range of concentration over which current response varies proportionally as a function of analyte concentration is called linear detection range of the biosensor. In this work, the linear range has been determined by CV/EIS techniques (**Chapter III-V**). The sensitivity has been estimated from the slope of the linearity curve. Further, the limit of detection (LOD) has been determined by using **Eq. 2.4**.

$$LOD = 3\sigma/m \quad 2.4$$

Where  $m$  is the slope and  $\sigma_b$  is the standard deviation of the linearity curve.

### **2.5.3. Shelf-life and reproducibility of the bioelectrodes**

The lifetime of biosensor has been decided by some parameters such as shelf-life and reproducibility. The shelf-life refers to the duration for which the sensor is considered to be suitable for use and it can retain its activity. While the reproducibility is a measure of the scatter or drift in a series of observations over a period of time. The material utilized,

morphology of the fabricated film and biomolecule immobilization method are important factors which affect the stability of bioelectrode. The shelf-life is calculated by measuring the current response of the bioelectrodes at regular intervals of time while the reproducibility records the number of times the bioelectrode can be utilized.

## 2. 6. References

- [1]. Segneanu, A.E., et al., *Organic compounds FT-IR spectroscopy*. Vol. 145. 2012: InTech Rijeka, Croatia.
- [2]. Bell, R., *Introductory Fourier transform spectroscopy*. 2012: Elsevier.
- [3]. Tuschel, D., *Raman spectroscopy and polymorphism*. *Spectroscopy*, 2019. **34**(3): p. 10-21.
- [4]. Raghavan, R. and J.C. Joseph, *Spectroscopic Methods of Analysis: Ultraviolet and Visible Spectrophotometry*. *Cosmic rays*, 2013. **1020**(10): p. 12.
- [5]. Saadatkah, N., et al., *Experimental methods in chemical engineering: thermogravimetric analysis—TGA*. *The Canadian Journal of Chemical Engineering*, 2020. **98**(1): p. 34-43.
- [6]. Kuo, S.W. and F.C. Chang, *Miscibility behavior and specific interaction of phenolic resin with poly (acetoxystyrene) blends*. *Macromolecular Chemistry and Physics*, 2002. **203**(5-6): p. 868-878.
- [7]. Epp, J., *X-ray diffraction (XRD) techniques for materials characterization*, in *Materials characterization using nondestructive evaluation (NDE) methods*. 2016, Elsevier. p. 81-124.
- [8]. Rajender, G. and P. Giri, *Strain induced phase formation, microstructural evolution and bandgap narrowing in strained TiO<sub>2</sub> nanocrystals grown by ball milling*. *Journal of Alloys and Compounds*, 2016. **676**: p. 591-600.
- [9]. Zhou, W., et al., *Fundamentals of scanning electron microscopy (SEM)*, in *Scanning microscopy for nanotechnology*. 2006, Springer. p. 1-40.
- [10]. Goldstein, J.I., et al., *Scanning electron microscopy and X-ray microanalysis*. 2017: Springer.
- [11]. Shah, M. *Electron Microscopy: A versatile tool in nanoworld*. in *Materials Science Forum*. 2013. Trans Tech Publ.



- [12]. Shi, B., *Transmission electron microscope*. Young Scientists Journal, 2016(18): p. 33.
- [13]. Pochapski, D.J., et al., *Zeta potential and colloidal stability predictions for inorganic nanoparticle dispersions: Effects of experimental conditions and electrokinetic models on the interpretation of results*. Langmuir, 2021. **37**(45): p. 13379-13389.
- [14]. Elgrishi, N., et al., *A practical beginner's guide to cyclic voltammetry*. Journal of chemical education, 2018. **95**(2): p. 197-206.
- [15]. Aikens, D.A., *Electrochemical methods, fundamentals and applications*. Journal of Chemical Education, 1983. **60**(1): p. A25.
- [16]. Zhang, N., M.A. Halali, and C.-F. de Lannoy, *Detection of fouling on electrically conductive membranes by electrical impedance spectroscopy*. Separation and Purification Technology, 2020. **242**: p. 116823.
- [17]. Schmid, A.U. and K.P. Birke, *Potential of Capacitive Effects in Lithium-ion Cells*, in *MODERN BATTERY ENGINEERING: A Comprehensive Introduction*. 2019, World Scientific. p. 187-222.

## *CHAPTER 3*

### *Nanostructured titanium oxide decorated graphene oxide-based electrochemical biosensor for cancer biomarker detection*

---

#### **3.1. Introduction**

In this chapter, a sensitive, label-free and efficient electrochemical immunosensor for early detection of epithelial cell adhesion molecules (EpCAM, tumor biomarker) antigen has been reported. The titanium oxide (TiO<sub>2</sub>) nanoparticles decorated with reduced graphene oxide (rGO) nanocomposite has been used in this immunosensor. The rGO@TiO<sub>2</sub> nanocomposite has been synthesized hydrothermally and then it was deposited electrophoretically on an indium tin oxide (ITO) coated glass plate. The deposition was confirmed by analyzing this using spectroscopic, microscopic, and electrochemical techniques etc. This fabricated biosensor showed the good selectivity and reproducibility and can potentially be used for the early detection of cancer biomarkers.

The details of nanostructured titanium oxide decorated graphene oxide based electrochemical biosensor for epithelial cancer biomarker EpCAM detection are presented in the following sections.

#### **3.2. Experimental section**

##### **3.2.1. Synthesis of GO and TiO<sub>2</sub> nanoparticles**

The graphene oxide (GO) has been synthesized from graphite by using modified Hummer's method. 1 g of sodium nitrate (NaNO<sub>3</sub>) and 2 g of graphite were mixed with concentrated H<sub>2</sub>SO<sub>4</sub> (50 mL) under constant stirring. Then 6 g potassium permanganate (KMnO<sub>4</sub>) was added to the solution after 2 h and temperature of the solution was also maintained below 20°C. This mixture was further stirred for another 24 h at 35 °C, followed by the dilution of using water (500 mL) under vigorous stirring. The suspension so obtained was further treated with hydrogen peroxide (H<sub>2</sub>O<sub>2</sub>) solution (10 ml; 30%) to check the completion of the reaction with KMnO<sub>4</sub>. The mixture so formed was filtered after washing with hydrochloric acid (HCl), followed by H<sub>2</sub>O, and then dried. The

synthesized GO was dispersed in DI water ( $0.1 \text{ mg mL}^{-1}$ ) and sonicated before its further use [1].

15 mL of tetrabutyltitanate (TBOT) was added slowly to 1500 mL of DI water under vigorous stirring for 3 h to synthesize the  $\text{TiO}_2$  nanoparticles. A gel precipitate was formed when it was kept for 24 h for aging. The gel precipitate so formed was filtered and then washed with DI water. The gel precipitate was dried at  $80 \text{ }^\circ\text{C}$  for 10 h and finely powdered and calcined at  $500 \text{ }^\circ\text{C}$  for 3 h [2].

### 3.2.2. Synthesis of $\text{rGO@TiO}_2$ nanocomposite

10 mg GO and 1.5 m mol TBOT both were added to the diethylene glycol (30 mL) and stirred for 12 h at room temperature. This mixture was added drop wise to 180 mL of acetone followed by a slow addition of DI water. This mixture was again stirred for 2 h which resulted in the formation of  $\text{GO@TiO}_2$  that was centrifuged at 15,000 rpm and then washed with water/ethanol [2].

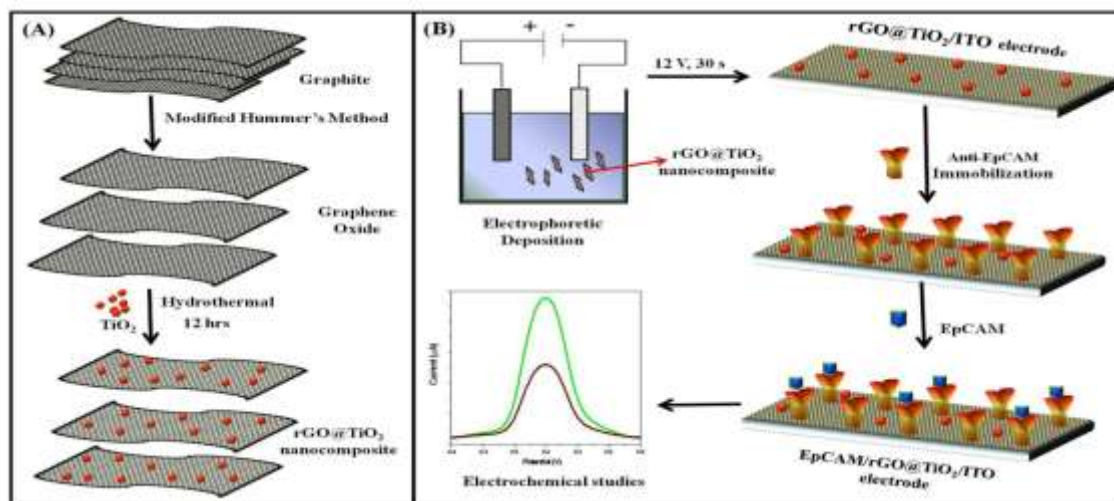


**Figure 3.1.** Schematic illustration for the (A) synthesis and electrophoretic deposition of  $\text{rGO@TiO}_2$  onto the ITO coated electrode and (B) subsequent biosensor fabrication

The above synthesized  $\text{GO@TiO}_2$  and 1.5 m mol L-cysteine were added into 80 mL DI water and transferred to 100 mL autoclave for hydrothermal reaction at  $120 \text{ }^\circ\text{C}$  for 12 h.

This process is used for the reduction of the GO. The product so obtained was centrifuged at 15,000 rpm and the precipitate was collected and washed with water/ethanol as shown in Fig. 3.1(A) [3].

### **3.2.3. Electrophoretic deposition (EPD) of rGO and rGO@TiO<sub>2</sub> nanocomposite**

The EPD of rGO and rGO@TiO<sub>2</sub> nanocomposite was carried out onto a pre-hydrolyzed ITO coated glass electrode using DC power supply. Pt electrode was used as the counter electrode in the cell assembly. A colloidal solution (5 mL) of rGO@TiO<sub>2</sub> nanocomposite (0.5 mg dL<sup>-1</sup>) was further diluted with 10 mL ethanol and then deposited cathodically onto the hydrolyzed ITO coated glass electrode at 12 V for 30 s. A magnesium nitrate (10<sup>-4</sup> M) solution was also added to the above colloidal solution for obtaining the adequate positive surface charge on the rGO@TiO<sub>2</sub> nanocomposite. Since, the Mg<sup>2+</sup> ions get absorbed onto the rGO sheets, so it gives positive charge. After the EPD, the electrode was taken out from the solution, washed with DI water, and then dried for further use [4].

### **3.2.4. Fabrication of rGO/ITO and rGO@TiO<sub>2</sub>/ITO based immunosensor**

The rGO/ITO and rGO@TiO<sub>2</sub>/ITO electrodes were treated with a mixture of 2 mM N-ethyl-N'-(3-dimethyl aminopropyl) carbodiimide (EDC) 10 $\mu$ L and 5 mM N-hydroxy succinimide (NHS) 10 $\mu$ L for 1h at room temperature to activate the functional groups like –COOH for the fabrication of immunosensor. Further, these treated electrodes were incubated with 20  $\mu$ L (50  $\mu$ g ml<sup>-1</sup>) of monoclonal antibodies, i.e., anti-EpCAM in the PBS buffer which contains 0.05% Tween-20. The anti-EpCAM/rGO@TiO<sub>2</sub>/ITO electrodes were treated with 1% BSA for 2 h to block the exposed binding sites of the electrode followed by washing with PBS three times to avoid non-specific antigen binding. The schematic representation of immunosensor fabrication has been depicted in Fig. 3.1(B). The characterization of rGO/ITO, rGO@TiO<sub>2</sub> nanocomposite and rGO@TiO<sub>2</sub>/ITO based immunosensor has been carried out by using various techniques and all the details are being reported in the following sections.

### 3. 3. Results and discussion

#### 3.3.1. Structural, morphological and elemental studies

The XRD of GO shows a peak at  $2\theta = 11.05^\circ$  which corresponds to an interlayer spacing of 7.99 Å [Fig. 3.2(A); inset] while the characteristic peak (002) for rGO can be seen around  $2\theta = 25.52^\circ$  [Fig. 3.2 (A); curve (i)]. The diffraction spectrum recorded for TiO<sub>2</sub> nanoparticles showed peaks at  $2\theta = 25.43^\circ$ ,  $38.02^\circ$ ,  $48.01^\circ$ ,  $53.85^\circ$ ,  $55.14^\circ$ , and  $62.54^\circ$ , corresponding to the (101), (103), (004), (112), (200), and (105) diffraction planes of TiO<sub>2</sub> nanoparticle (anatase; JCPDS no 841286), respectively [Fig. 3.2(B)]. While, the XRD spectrum for rGO@TiO<sub>2</sub> nanocomposite did not show any change from the diffraction peak of TiO<sub>2</sub> nanoparticle [Fig. 3.2(A); curve (ii)]. It has been observed that the broad diffraction peak of rGO disappeared in the composite spectrum which may be due to the overlapping of the TiO<sub>2</sub> (101) peak [5].

Figure 3.2(C) shows the TGA curves for the weight loss of graphite, TiO<sub>2</sub> nanoparticles, GO, rGO, and rGO@TiO<sub>2</sub> nanocomposite. The TGA for synthetic graphite [curve (v)] revealed excellent stability up to 900 °C, while the synthesized TiO<sub>2</sub> nanoparticles have overall excellent thermal stability with 2% weight loss at the temperature below 120 °C [curve (iv)]. The TGA thermogram of GO shows a drastic loss in its weight (around 44%) at a temperature of less than 400 °C. This loss in weight is perhaps due to the decomposition of labile oxygen containing groups (epoxy and hydroxyl) and also the removal of gases like H<sub>2</sub>O and CO<sub>2</sub> [curve (i)]. Further, a maximum loss of 78% was observed in the temperature range 400 - 900 °C, owing to the decomposition of the carbonyl group formed on the surface of GO. The TGA curve for rGO also shows a similar trend to that of GO, but in the case of rGO, the change was small (48%), as during the hydrothermal process majority of the oxygen containing functional groups in GO were reduced. For the rGO@TiO<sub>2</sub> nanocomposite, there was a weight loss of only 27% of the original weight revealing that the synthesized nanocomposite had some labile oxygen containing functional groups present on the surface of rGO@TiO<sub>2</sub> [6].

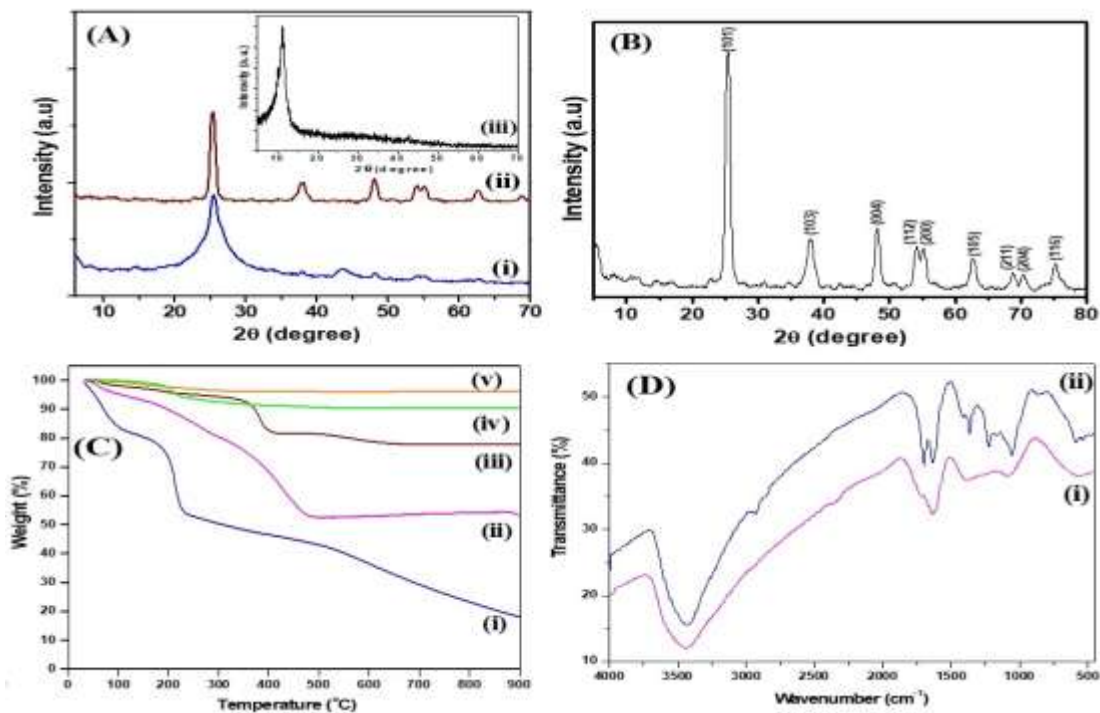


**Figure 3.2.** (A) X-ray diffraction patterns of (i) rGO (ii) rGO@TiO<sub>2</sub> nanocomposite, (iii) GO (inset) (B) XRD spectra of TiO<sub>2</sub> nanoparticles (C) TGA curve for (i) GO (ii) rGO (iii) rGO@TiO<sub>2</sub> nanocomposite (iv) TiO<sub>2</sub> nanoparticles (v) graphite in the temperature range of 25 to 900 °C at 10 °C/min heating rate in a nitrogen environment (D) FTIR spectra of (i) rGO@TiO<sub>2</sub> nanocomposite and (ii) GO in the frequency region of 500 - 4000 cm<sup>-1</sup>

The FTIR spectra of GO show a broad peak in the high frequency region, i.e., 3000–3700 cm<sup>-1</sup> with a sharp peak at 1634 cm<sup>-1</sup> due to the stretching and bending vibration of OH groups present in GO [Fig. 3.2(D); curve (ii)]. The intensities of the absorption peaks corresponding to the oxygen functionalities at 1703 cm<sup>-1</sup> (C=O stretching) and 1370 cm<sup>-1</sup> (O–H deformation) decreases significantly after the reduction of GO. There is a decrease in the peak intensities of the C–O (epoxy; 1068 cm<sup>-1</sup>) stretching vibration and the C–O (alkoxy; 1232 cm<sup>-1</sup>) stretching vibration of GO confirming the reduction of GO [Fig. 3.2(D); curve (i)] [5]. In addition to the peaks mentioned above, a low-frequency band around 650 cm<sup>-1</sup> has also been observed that corresponds to the presence of the Ti–O–Ti bond. It confirms that a strong chemical bond has been formed between GO and TiO<sub>2</sub>

nanoparticles during the hydrothermal process. After the immobilization of anti-EpCAM on rGO@TiO<sub>2</sub> electrode, the new peaks were observed at 3199 and 1560 cm<sup>-1</sup> which appear due to the stretching vibration of N–H and C=O, confirming the formation of peptide bonds.

The formation of GO from graphite was confirmed by using UV-visible spectroscopy. An absorption band at 229 nm due to the  $\pi$ - $\pi^*$  transition of aromatic C=C bonds and a shoulder around 300 nm due to the n- $\pi^*$  transition of aromatic C=O bonds were observed in the UV-Vis spectra of GO [Fig. 3.3 (A)]. The shoulder at 300 nm disappears gradually due to the oxygen removal and a peak at 229 nm gradually red-shifts to around 234 nm showing the formation of rGO as given in Fig. 3.3 (B).

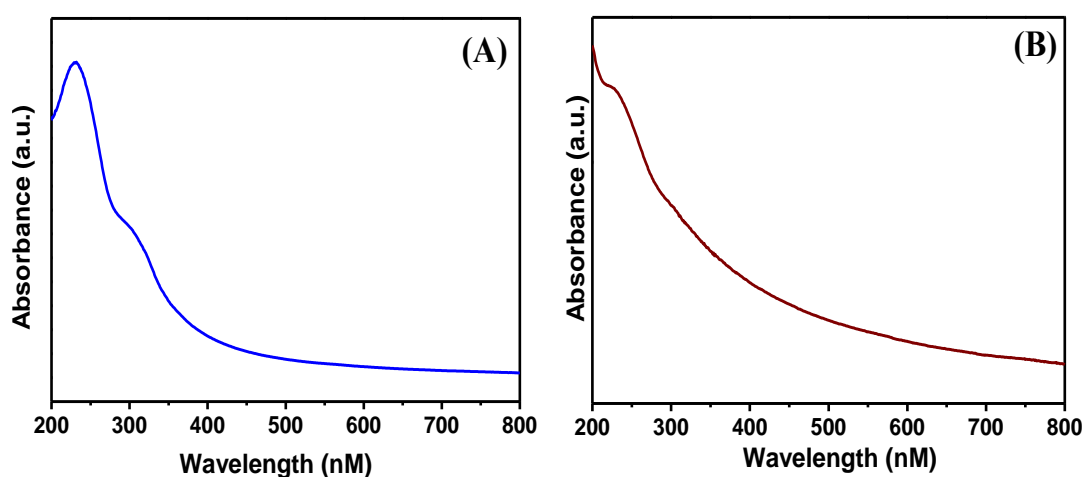


**Figure 3.3.** UV-visible spectra of (A) GO and (B) rGO

The TEM micrographs of GO sheet display a crumbled and re-stacked morphology as shown in Fig. 3.4 (A) with a large surface area. The large surface area is advantageous for the growth of TiO<sub>2</sub> nanoparticles on the GO surface. The spherically polycrystalline TiO<sub>2</sub> nanoparticles (30-40 nm) are evenly distributed in the GO sheet as seen in the TEM micrograph of nanocomposite presented in Fig. 3.4 (B). Thus, it is revealed that the GO may be used as an excellent platform for entrapping the TiO<sub>2</sub> nanoparticles.

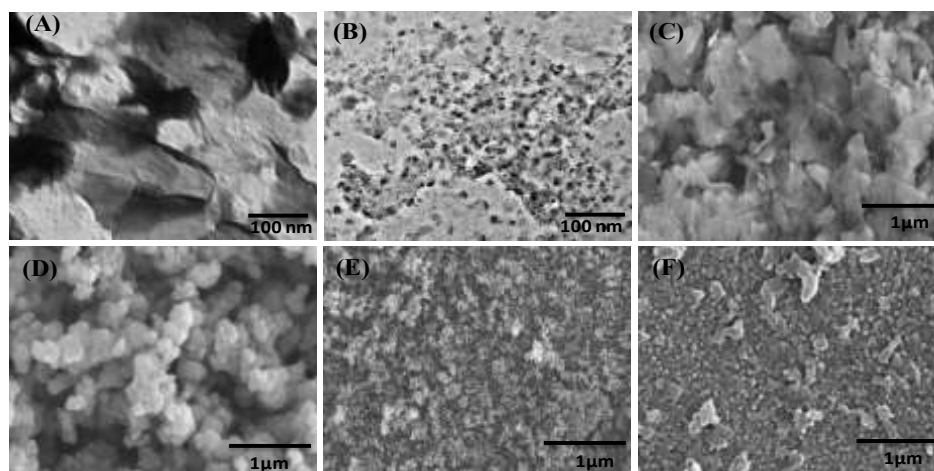


**Figure 3.4.** TEM micrographs of (A) GO and (B) rGO@TiO<sub>2</sub> nanocomposite; SEM micrographs of (C) rGO/ITO electrode (D) TiO<sub>2</sub>/ITO electrode (E) rGO@TiO<sub>2</sub>/ITO electrode and (F) anti-EPCAM/ rGO@TiO<sub>2</sub>/ITO electrode

### 3.3.2. Electrochemical characterization

The electrochemical studies on rGO/ITO, rGO@TiO<sub>2</sub>/ITO electrodes and anti-EpCAM/ rGO@TiO<sub>2</sub>/ITO bioelectrode have been carried out in PBS containing 5mM of [Fe(CN)<sub>6</sub>]<sup>3-/4-</sup> by using an electrochemical impedance spectroscopy (EIS) technique in the frequency range of 0.01-10<sup>5</sup> Hz. The characteristic Nyquist plots of the fabricated electrodes are shown in Fig. 3.5(A) along with the fitted Randles equivalent circuit [7]. The EIS curve of rGO/ITO electrode shows an R<sub>ct</sub> value of 1.35 kΩ [Fig. 3.4 (A)]; curve (ii), which is attributed due to the good conductivity of GO which helps fast electron transfer. Moreover, there was a decrease in the R<sub>ct</sub> value (1.12 kΩ) reported in case of the rGO@TiO<sub>2</sub>/ITO electrode as shown in Fig. 3.5(A) curve (i). This decrease in R<sub>ct</sub> could be attributed due to the synergistic effects of GO sheets and TiO<sub>2</sub> which enhances the electrochemical performance of rGO@TiO<sub>2</sub>/ITO electrodes. Further, an increase in the R<sub>ct</sub> value (1.68 kΩ) was reported after immobilization of anti-EpCAM onto rGO@TiO<sub>2</sub>/ITO electrode [Fig. 3.5 (A); curve (iii)], and on the blocking of exposed electrode site by using BSA. An increase in R<sub>ct</sub> is found perhaps due to the non conducting behaviour of the antibody which hinders the pathway for charge transfer. When, the target antigen was incubated to anti-



EpCAM/rGO@TiO<sub>2</sub>/ITO electrode, an antibody-antigen complex has been formed that creates a barrier for the electrochemical transduction process, thereby hindering the access of the redox probe to the electrode surface, and thus increasing the R<sub>ct</sub> (2.53 kΩ) [8]. The EIS spectra suggest that the reaction occurring at the electrode is governed by the electron transfer kinetics. The values of exchange current per geometric unit area ( $i_o = nRT/R_{ct}F$ ) in case of rGO/ITO electrode and rGO@TiO<sub>2</sub>/ITO electrode were found as  $7.60 \times 10^{-5} \text{ A/cm}^2$  and  $9.32 \times 10^{-5} \text{ A/cm}^2$ , respectively. The apparent electron transfer rate constant ( $k_{app}$ ) was also calculated for modified electrodes by using the equation:  $k_{app} = RT/n^2F^2AR_{ct}C$ . Where F is the Faraday constant, n the number of electrons transferred, R is the gas constant, T is the temperature, A is the area of electrode, and C the concentration of [Fe(CN)<sub>6</sub>]<sup>3-/4-</sup>. Using the above mentioned equation, the calculated values of  $k_{app}$  are found as  $1.57 \times 10^{-7}$  and  $1.93 \times 10^{-7} \text{ cm/s}$  for rGO/ITO and rGO@TiO<sub>2</sub>/ITO electrodes, respectively. Furthermore, it was also seen that the peak current is proportional to the square root of scan rate as shown in Fig. 3.5 (C). It suggests that the linear relationship between peak current and the scan rate. This indicates that the electron transfer from rGO/ITO and rGO@TiO<sub>2</sub>/ITO electrode is a surface controlled process [9]. Moreover, it is also seen that the oxidation peak drifts to a more positive value and the reduction peak towards more negative value when the scan rate ( $\nu$ ) was varied from 10 to 300 mV sec<sup>-1</sup>. This clearly infers that both the peak potentials are linearly related to the log  $\nu$  as shown in Fig. 3.5 (C). It gives two straight lines (Eq. 3.1, 3.2, 3.3 & 3.4) and the anodic and cathodic slopes are found to be  $2.303RT/(1-\alpha)nF$  and  $-2.303RT/\alpha nF$ , respectively.

$$E_p \text{ (V) [rGO@TiO}_2\text{/ITO]} = 0.124 \text{ (V)} + 0.067 \text{ (V)} \times \log [\text{scan rate (mV/s)}];$$

$$R^2 = 0.994 \quad \text{Eq. 3.1}$$

$$E_c \text{ (V) [rGO@TiO}_2\text{/ITO]} = 0.143 \text{ (V)} - 0.060 \text{ (V)} \times \log [\text{scan rate (mV/s)}];$$

$$R^2 = 0.994 \quad \text{Eq. 3.2}$$

$$E_p \text{ (V) [rGO/ITO]} = 0.115 \text{ (V)} + 0.067 \text{ (V)} \times \log [\text{scan rate (mV/s)}];$$

$$R^2 = 0.996 \quad \text{Eq. 3.3}$$

$$E_c \text{ (V) [rGO/ITO]} = 0.151 \text{ (V)} - 0.058 \text{ (V)} \times \log [\text{scan rate (mV/s)}];$$

$$R^2 = 0.987 \quad \text{Eq. 3.4}$$

Based on the above equations and plots,  $\alpha$  values are estimated to be 0.59 and 0.61 for rGO/ITO and rGO@TiO<sub>2</sub>/ITO electrodes, respectively. Further, the diffusion coefficient (D) has been calculated using the linear slope of the anodic peak currents on the square root scan rate (Eq. 3.5, 3.6, 3.7 & 3.8), and the Randle Sevcik equation:  $I_p = (2.99 \times 10^5) \alpha^{1/2} n^{3/2} ACD^{1/2} v^{1/2}$ .

$$I_{pa} \text{ (}\mu\text{A) [rGO@TiO}_2\text{/ITO]} = 19.09 \mu\text{A} + 86.04 \mu\text{A (s/mV)} \times \text{scan rate (mV/s)}$$

$$R^2=0.996 \quad \text{Eq. 3.5}$$

$$I_{pc} \text{ (}\mu\text{A) [rGO@TiO}_2\text{/ITO]} = -26.24 \mu\text{A} - 62.53 \mu\text{A (s/mV)} \times \text{scan rate (mV/s)}$$

$$R^2=0.992 \quad \text{Eq. 3.6}$$

$$I_{pa} \text{ (}\mu\text{A) [rGO/ITO]} = 49.11 \mu\text{A} + 82.56 \mu\text{A (s/mV)} \times \text{scan rate (mV/s)}$$

$$R^2=0.975 \quad \text{Eq. 3.7}$$

$$I_{pc} \text{ (}\mu\text{A) [rGO/ITO]} = -13.63 \mu\text{A} - 63.5 \mu\text{A (s/mV)} \times \text{scan rate (mV/s)}$$

$$R^2=0.987 \quad \text{Eq. 3.8}$$

Here  $I_p$  is the peak current, C is the molar concentration of  $[\text{Fe}(\text{CN})_6]^{3-/4-}$ , A is the area of the electrode (0.25 cm<sup>2</sup>), and  $v$  is the scan rate (30 mVs<sup>-1</sup>). The value of D calculated for rGO@TiO<sub>2</sub>/ITO electrode (1.07 x 10<sup>-12</sup> cm<sup>2</sup> s<sup>-1</sup>) is greater than that of rGO/ITO electrode (4.76 x 10<sup>-13</sup> cm<sup>2</sup> s<sup>-1</sup>), suggesting that the ITO electrode is well covered by rGO@TiO<sub>2</sub>.

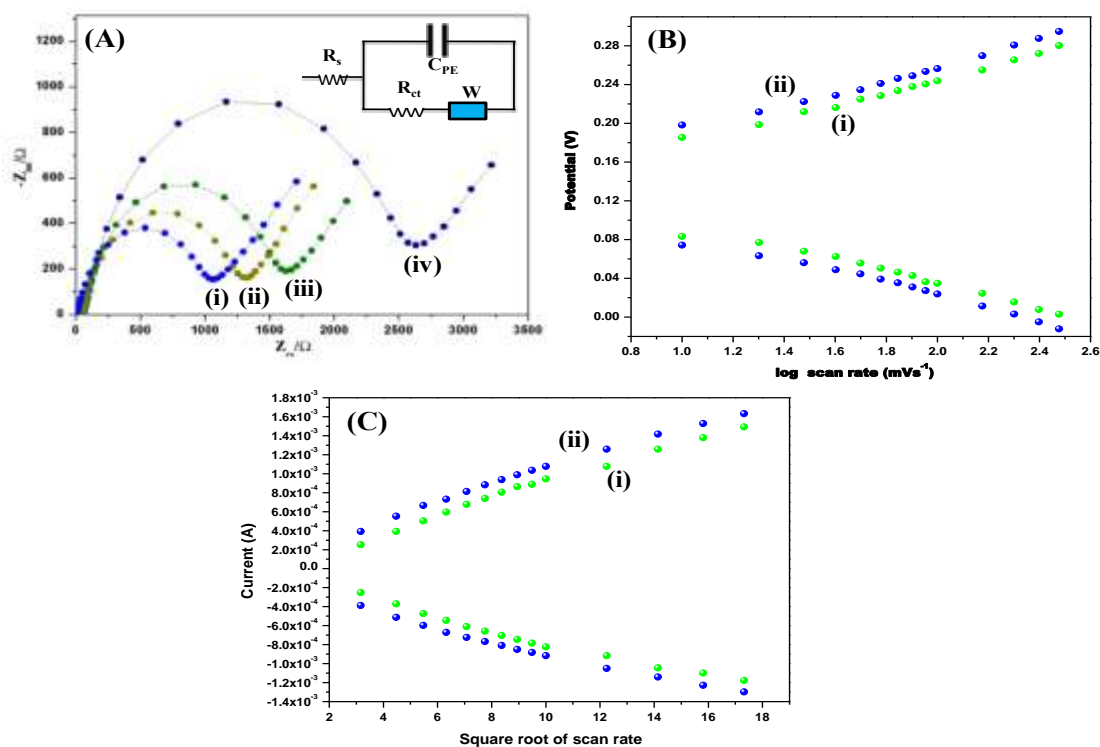


**Figure 3.5.** (A) Nyquist plot for Faradic impedance of (i) rGO@TiO<sub>2</sub>/ITO (ii) rGO/ITO (iii) anti-EPCAM/ rGO@TiO<sub>2</sub>/ITO electrode, and (iv) EpCAM immobilized on anti-EPCAM/ rGO@TiO<sub>2</sub>/ITO electrode data in PBS solution (pH 7.4) containing 5 mM [Fe(CN)<sub>6</sub>]<sup>3-/4-</sup>, in the frequency range of 10<sup>6</sup> to 10<sup>-2</sup> Hz. Cyclic voltammetric analysis showing the variation of (B) potential with log of scan rate and (C) current with (scan rate)<sup>1/2</sup> from 10-300 mV in case of (i) rGO@TiO<sub>2</sub>/ITO and (ii) rGO/ITO electrode.

### 3.3.3. Optimization studies

The optimization of anti-EpCAM concentration requirement for binding onto the surface of rGO@TiO<sub>2</sub>/ITO electrode using EDC-NHS chemistry was also done using DPV technique [Fig. 3.6 (A)]. The results indicate that the peak current rapidly increased in the concentration range of 10-50 μg mL<sup>-1</sup> and then reached a plateau at EpCAM concentration higher than 50 μg mL<sup>-1</sup> and got saturated. So, for the fabrication of the immunosensor, an optimized EpCAM concentration of 50 μg mL<sup>-1</sup> was used. The incubation time of the anti-EpCAM/rGO@TiO<sub>2</sub>/ITO electrode with the EpCAM (1 ng mL<sup>-1</sup>) antigen is also determined by varying the incubation time from 0 to 20 min [Fig. 3.6 (B)]. The DPV results indicate that the magnitude of current decreases from 0 to 10 min. After 10 min, it

gets saturated, and showing that the maximum binding of EpCAM with the antibodies has been achieved in 10 min.

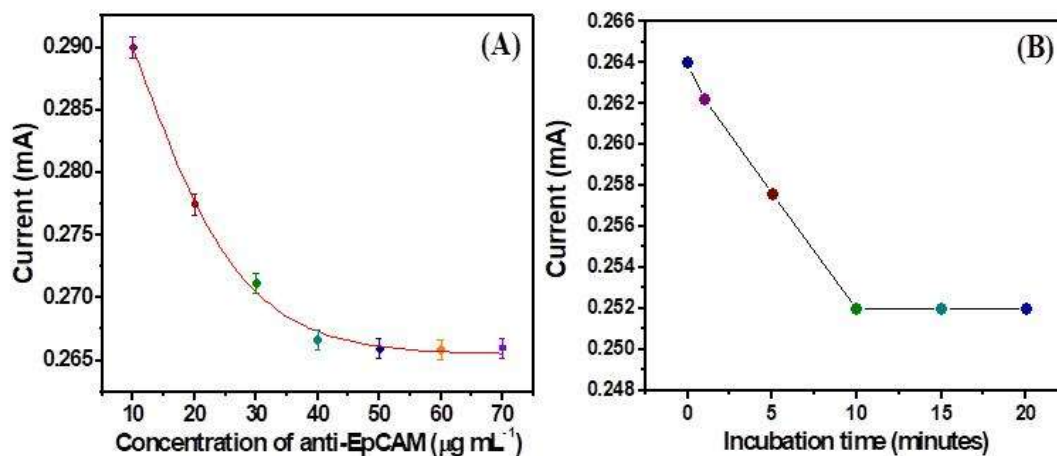


**Figure 3.6** (A) Optimization of the antibody concentration (10 to 70  $\mu\text{g mL}^{-1}$ ) after immobilization on rGO@TiO<sub>2</sub>/ITO electrodes and (B) Incubation time study of anti-EpCAM/rGO@TiO<sub>2</sub>/ITO electrode. Error bars: SD, n = 3

### 3.3.4. Electrochemical biosensing studies

The efficacy of the biosensor has been examined by electrochemical studies using DPV technique. These electrochemical studies of anti-EpCAM/rGO@TiO<sub>2</sub>/ITO electrode was carried out as a function of EpCAM in PBS containing 5 mM [Fe(CN)<sub>6</sub>]<sup>3-/4-</sup>. A continuous decrease in the anodic peak current was seen on treating the anti-EpCAM/rGO@TiO<sub>2</sub>/ITO electrode with the EpCAM concentration increase. The decrease in the anodic peak current is probably due to the interaction of EpCAM with anti-EpCAM on the surface of transducer. It results due to the formation of non conducting layer (antigen-antibody complex) on the electrode surface which seems to retard the electron transfer from bulk solution to electrode. Fig. 3.7 (B) shows the calibration curve for the change in the peak current magnitude of anti-EpCAM/rGO@TiO<sub>2</sub>/ITO electrode as a function of EpCAM concentration in the range of 0.01-60 ng mL<sup>-1</sup> by following the Eq. (3.9):

$$I_p = 0.025 (\mu\text{A}) - 0.814 (\mu\text{A/ng/mL}) \times \text{EpCAM conc. (ng/mL)} \quad \text{Eq. 3.9}$$

The sensitivity of anti-EpCAM/rGO@TiO<sub>2</sub>/ITO electrode was calculated by slope/surface

area which is found to be  $3.24 \mu\text{A mL ng}^{-1} \text{cm}^{-2}$  with a correlation coefficient of 0.997. The limit of detection (LOD) was calculated as  $3\sigma/\text{sensitivity}$ , where  $\sigma$  is the standard deviation of blank electrode. The LOD value of the fabricated biosensor is found as  $0.0065 \text{ ng mL}^{-1}$ . The anti-EpCAM/rGO@TiO<sub>2</sub>/ITO electrode with PBS solution was taken as a control signal in this case of all sensing observations. The imprecision of the data was found to be <3% as shown in the Fig. 3.7 (B). The fabricated rGO@TiO<sub>2</sub>/ITO electrode achieved a LOD of  $6.5 \text{ pg mL}^{-1}$  that is comparable to the other reported sensors. Moreover, our fabricated biosensor has the potential to be a simple, cheap, smooth operation, stable, and shows good selectivity [10]. The enhanced electrochemical performance of anti-EpCAM/rGO@TiO<sub>2</sub>/ITO electrode can be attributed to the good conductivity, stability, and biocompatibility of rGO@TiO<sub>2</sub> that improve the local topographic interactions with the EpCAM surface [11]. To determine the affinity of EpCAM towards anti-EpCAM/rGO@TiO<sub>2</sub>/ITO electrode, the association constant ( $K_a$ ) was calculated using Hanes–Wolf plot [12] and the higher is the value of  $K_a$ , the stronger is the affinity of EpCAM towards anti-EPCAM/rGO@TiO<sub>2</sub>/ITO electrode. The  $K_a$  value was estimated by plotting the curve between substrate concentrations versus substrate concentration/current and it is found to be  $4.86 \text{ mL ng}^{-1}$ . The current response of bare rGO@TiO<sub>2</sub>/ITO electrode towards different concentration of EpCAM was also evaluated by conducting the electrochemical studies which have been shown in Fig. 3.7 (C). These results clearly indicate that there was no significant change in the peak current. It reveals that there is no false signal generated and the electrochemical response was completely based on the interaction between the EpCAM and anti-EpCAM/rGO@TiO<sub>2</sub>/ITO electrode.

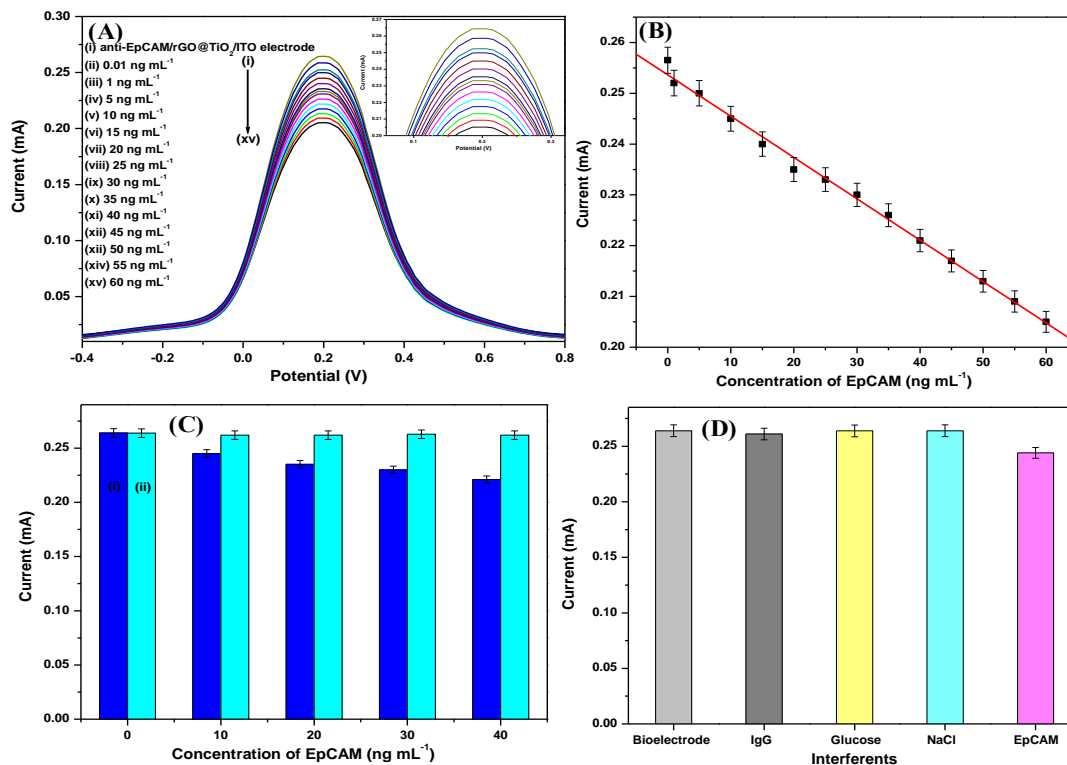


**Figure 3.7.** DPV electrochemical response of (A) anti-EpCAM/rGO@TiO<sub>2</sub>/ITO electrode against EpCAM concentration; the magnified view of oxidation peak current is also shown in the inset, (B) linearity plot with variation in the concentration of EpCAM (0.01-60 ng mL<sup>-1</sup>) (C) control experiment showing the DPV response of (i) anti-EpCAM/rGO@TiO<sub>2</sub>/ITO electrode (ii) rGO@TiO<sub>2</sub>/ITO electrode as a function of EpCAM (D) Specificity of anti-EpCAM/rGO@TiO<sub>2</sub>/ITO biosensor with IgG proteins and glucose as control. The potential was scanned from -0.4 to 0.8 V with amplitude of 50 mV in PBS solution containing 5 mM [Fe(CN)<sub>6</sub>]<sup>3-/4-</sup> at pH 7. Error bars: SD, n = 3

### 3.3.5. Electrode studies

DPV studies were carried to investigate the effect of electrode modification at various steps. These studies were carried out for ITO, rGO/ITO, rGO@TiO<sub>2</sub>/ITO and anti-EpCAM/rGO@TiO<sub>2</sub>/ITO electrodes in the potential range of -0.4 to +0.8 V as shown in Fig. 3.8. The electrochemical current magnitude of bare hydrolyzed ITO was found as 0.24 mA [curve (i)]. In contrast, the peak currents obtained for the rGO/ITO electrode and rGO@TiO<sub>2</sub>/ITO electrode were found to be 0.28 mA [curve (iii)] and 0.30 mA [curve (iv)], respectively. The increase in current for rGO@TiO<sub>2</sub>/ITO electrode compared to the

ITO electrode is probably due to the grafting of TiO<sub>2</sub> nanoparticles onto the two dimensional rGO sheets which leads to a better electron transfer pathway from bulk electrolyte solution to the ITO electrode. After the modification of the rGO@TiO<sub>2</sub>/ITO electrode with anti-EpCAM, the peak current decreases slightly [curve (ii; 0.26 mA)]. This decrease in the current corresponds to the formation of a macromolecular layer of antibodies on the rGO@TiO<sub>2</sub>/ITO electrode leading to reduced electron transfer [13].

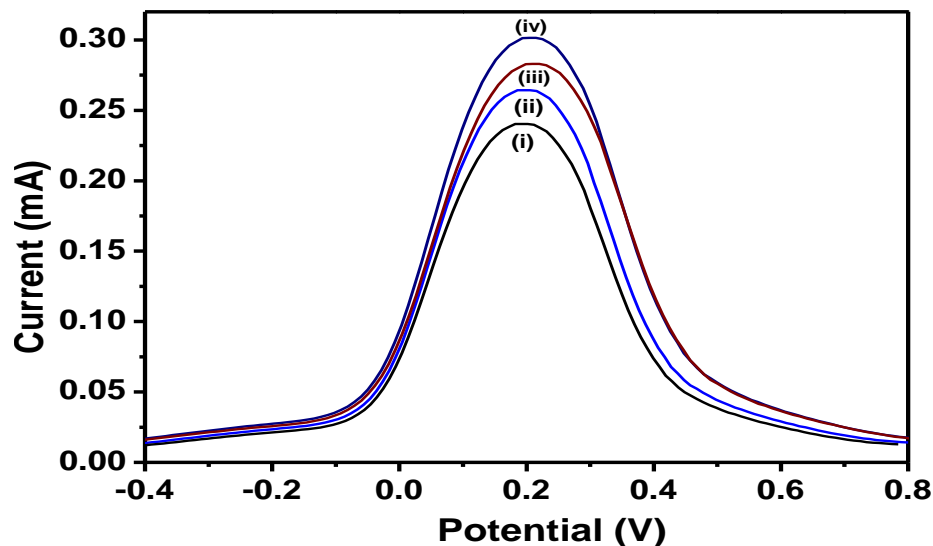


**Figure 3.8.** DPV electrochemical peak response of (i) ITO electrode (ii) anti-EpCAM/rGO@TiO<sub>2</sub>/ITO (iii) rGO/ITO and (iv) rGO@TiO<sub>2</sub>/ITO electrode. The potential sweeping taken from -0.4 to 0.8 V with 50 mV amplitude in PBS solution containing 5 mM [Fe(CN)<sub>6</sub>]<sup>3-/4-</sup> at pH 7.

### 3.3.6. Specificity and serum sample analysis

The specificity of the immunosensor was carried out by incubating the anti-EpCAM/rGO@TiO<sub>2</sub>/ITO bioelectrode with sodium chloride (NaCl), glucose, immunoglobulin G (IgG) and EpCAM in 15 ng mL<sup>-1</sup> concentration. The false signal was generated when the fabricated electrode was treated with glucose, IgG, and NaCl. It shows the good specificity of the biosensor for EpCAM detection. These results are clearly shown in the bar diagram [Fig. 3.7 (D)].

The performance of the fabricated biosensor was validated by using the electrochemical response studies of the anti-EpCAM/rGO@TiO<sub>2</sub>/ITO electrode with spiked human serum

sample at different concentrations such as 5, 10, 15, and 20 ng mL<sup>-1</sup>. The electrochemical response data have been reported in the Table 1. The spiked serum samples under investigation were prepared by adding 20 µL of EpCAM into 100 µL of serum. Our results exhibit acceptable recoveries (98–101%) with relative standard deviation (1.8–4.7%, n = 3) of EpCAM in serum samples. It suggests that this fabricated immunosensor may be used as an alternative technique for the detection of EpCAM in human serum.

**Table 3.1:** Comparison data showing the anodic peak current obtained for EpCAM antigen concentration in standard and spiked serum samples using anti-EpCAM/rGO@TiO<sub>2</sub>/ITO electrode

S No.	EpCAM concentration (ng·mL <sup>-1</sup> )	Peak current obtained for standard EpCAM samples (mA)	Peak current obtained with spiked serum samples (mA)	Relative Standard Deviation (RSD) % (n=3)
1	5	0.249	0.250	1.8
2	10	0.254	0.255	2.3
3	15	0.235	0.233	4.7
4	20	0.230	0.226	2.2

### 3.3.7. Stability and regeneration

The storage stability of the fabricated immunosensor was also tested by keeping the anti-EpCAM/rGO@TiO<sub>2</sub>/ITO electrode in a refrigerator at 4 °C and then measured its response towards EpCAM antigen at the interval of five days as shown in Fig. 3.9 (A). The current response value of the immunosensor remains 93.7 % only after 35 days. It clearly indicates that our immunosensor may have acceptable stability due to the conducive nature of rGO@TiO<sub>2</sub> which duly maintains the bioactivity of anti-EpCAM.



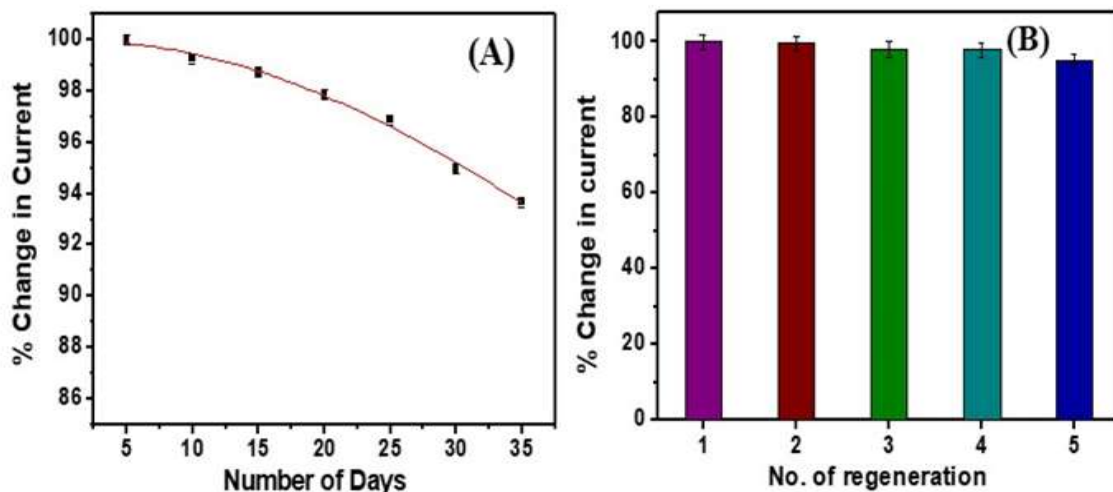


**Figure 3.9.** (A) Investigation of biosensor stability using DPV technique by recording the current response to EpCAM every 5 days upto 35 days (B) Regenerability of the biosensor for repeated detection of EpCAM over five cycles. Error bars: SD, n = 3

The regeneration step was performed by immersion of the working electrode in glycine-HCl buffer (0.1 M, pH = 2.2) for 10 min and washed with PBS solution to interrupt the antigen-antibody immune complexes [14]. Fig. 3.9 (B) shows a gradual decrease in the peak current after each regeneration cycle. This may be due to gradual shelling and denaturation of EpCAM or the structure of rGO@TiO<sub>2</sub> during continuous processing by a glycine-HCl buffer and cleaning with increased regeneration times [15]. The results demonstrate that this immunosensor may be regenerated and reused at least 5 times with a relative standard deviation of 6.6% with good precision and high reproducibility.

### 3.4. Conclusion

A highly sensitive label-free electrochemical biosensor was fabricated in the present study for the detection of cancer biomarkers by using rGO@TiO<sub>2</sub> nanocomposite. In this study, an environment friendly route was used for the synthesis of the nanocomposite. It shows excellent electrochemical properties like selectivity and also performs as an appropriate sensing layer. The rGO@TiO<sub>2</sub>/ITO electrode shows improved electron transfer kinetics with electron transfer rate constant as  $1.93 \times 10^{-7} \text{ cm s}^{-1}$  and a diffusion coefficient as 1.07

$\times 10^{-12} \text{ cm}^2 \text{ s}^{-1}$ . The rGO@TiO<sub>2</sub>/ITO electrodes were used to covalently immobilize monoclonal EpCAM antibodies. Label-free detection of EpCAM cancer biomarker is achieved by this fabricated biosensor using differential pulse voltammetry with high sensitivity ( $3.24 \mu\text{A mL ng}^{-1} \text{ cm}^{-2}$ ) and low detection limit ( $0.006 \text{ ng mL}^{-1}$ ). The GO-based substrate provides an excellent platform for the growth of TiO<sub>2</sub> nanoparticles. With covalent conjugation of anti-EpCAM antibody, a broader detection range of 0.01-60 ng mL<sup>-1</sup> and a much lower detection limit as  $0.0065 \text{ ng mL}^{-1}$  towards EpCAM cancer biomarker detection have been achieved. This biosensor was validated with spiked serum samples and shows the promising results for detection of cancer biomarkers in serum sample efficiently.

*The results of present study have been published in "Microchimica Acta (2020), 187(5), 275.*

## References

- [1] L Shahriary, AA Athawale, Graphene oxide synthesized by using modified hummers approach, *Int J Renew Energy Environ Eng*, 2(2014) 58-63.
- [2] SD Perera, RG Mariano, K Vu, N Nour, O Seitz, Y Chabal, et al., Hydrothermal synthesis of graphene-TiO<sub>2</sub> nanotube composites with enhanced photocatalytic activity, *Acs Catalysis*, 2(2012) 949-56.
- [3] CM Pandey, I Tiwari, VN Singh, K Sood, G Sumana, BD Malhotra, Highly sensitive electrochemical immunosensor based on graphene-wrapped copper oxide-cysteine hierarchical structure for detection of pathogenic bacteria, *Sensors and Actuators B: Chemical*, 238(2017) 1060-9.
- [4] S Srivastava, V Kumar, MA Ali, PR Solanki, A Srivastava, G Sumana, et al., Electrophoretically deposited reduced graphene oxide platform for food toxin detection, *Nanoscale*, 5(2013) 3043-51.
- [5] P Wang, J Wang, X Wang, H Yu, J Yu, M Lei, et al., One-step synthesis of easy-recycling TiO<sub>2</sub>-rGO nanocomposite photocatalysts with enhanced photocatalytic activity, *Applied Catalysis B: Environmental*, 132(2013) 452-9.
- [6] BYS Chang, NM Huang, MN An'amt, AR Marlinda, Y Norazriena, MR Muhamad, et al., Facile hydrothermal preparation of titanium dioxide decorated reduced graphene oxide nanocomposite, *International Journal of Nanomedicine*, 7(2012) 3379.
- [7] J-B Jorcin, ME Orazem, N Pébère, B Tribollet, CPE analysis by local electrochemical impedance spectroscopy, *Electrochimica Acta*, 51(2006) 1473-9.
- [8] Y Xie, A Chen, D Du, Y Lin, Graphene-based immunosensor for electrochemical quantification of phosphorylated p53 (S15), *Analytica chimica acta*, 699(2011) 44-8.
- [9] CM Pandey, G Sumana, I Tiwari, Copper oxide assisted cysteine hierarchical structures for immunosensor application, *Applied Physics Letters*, 105(2014) 103706.
- [10] L Tao, K Zhang, Y Sun, B Jin, Z Zhang, K Yang, Anti-epithelial cell adhesion molecule monoclonal antibody conjugated fluorescent nanoparticle biosensor for sensitive

detection of colon cancer cells, *Biosensors and Bioelectronics*, 35(2012) 186-92.

[11] M He, AE Herr, Automated microfluidic protein immunoblotting, *Nature protocols*, 5(2010) 1844-56.

[12] S Augustine, AG Joshi, BK Yadav, A Mehta, P Kumar, V Renugopalakrishanan, et al., An emerging nanostructured molybdenum trioxide-based biocompatible sensor platform for breast cancer biomarker detection, *MRS Communications*, 8(2018) 668-79.

[13] S Augustine, P Kumar, BD Malhotra, Amine-functionalized MoO<sub>3</sub>@ RGO nanohybrid-based biosensor for breast cancer detection, *ACS Applied Bio Materials*, 2(2019) 5366-78.

[14] V Kandimalla, N Neeta, N Karanth, M Thakur, K Roshini, BA Rani, et al., Regeneration of ethyl parathion antibodies for repeated use in immunosensor: a study on dissociation of antigens from antibodies, *Biosensors and bioelectronics*, 20(2004) 903-6.

[15] W Yi, W Liang, P Li, S Li, Z Zhang, M Yang, et al., Application of a Fab fragment of monoclonal antibody specific to N-terminal pro-brain natriuretic peptide for the detection based on regeneration-free electrochemical immunosensor, *Biotechnology letters*, 33(2011) 1539-43.

**CHAPTER 4**  
*Molybdenum disulfide grafted reduced graphene oxide  
nanohybrid based electrochemical biosensor for cancer biomarker  
detection*

---

#### **4.1. Introduction**

In this chapter, an ultrasensitive, electrochemical biosensor based on anti-EpCAM conjugated molybdenum disulfide grafted reduced graphene oxide ( $\text{MoS}_2@\text{rGO}$ ) nanohybrid as a sensing platform has been reported. The biomolecular assisted synthetic method was used for the synthesis of  $\text{MoS}_2@\text{rGO}$  nanohybrid, where L-cys is reducing the GO and Mo precursor. The following sections present all the details pertaining to the synthesis of  $\text{MoS}_2@\text{rGO}$  nanohybrid and all the characterization results.

#### **4.2. Experimental section**

##### **4.2.1. Synthesis of GO and rGO**

The synthesis of GO from graphite has already been discussed in chapter 3 [1, 2]. The synthesized GO was reduced by adding 0.6 g of L-cys into 40 mL of GO aqueous solution ( $0.5 \text{ mg mL}^{-1}$ ) and the solution was stirred for 10 h ( $27^\circ \text{C}$ ) [3]. The black colour product (rGO) so obtained was separated by centrifuging the solution at 9000 rpm. The product was washed 3-4 times with DI water to remove the excess of L-cys. The rGO product was then dried at  $100^\circ \text{C}$  in a vacuum oven for 12 h. The rGO was stored finally in a desiccator at room temperature for further use.

##### **4.2.2. Synthesis, and functionalization of $\text{MoS}_2@\text{rGO}$ nanohybrid**

The biomolecular-assisted synthetic route has been used for synthesizing the  $\text{MoS}_2@\text{rGO}$  nanohybrid [4]. The GO was added in 60 mL of DI water and then 0.5 g of  $(\text{NH}_4)_6\text{Mo}_7\text{O}_{24}\cdot 4\text{H}_2\text{O}$  was also added to the same. This solution has been ultrasonicated and stirred for 45 min. The pH of the solution was maintained at 6.5 by the addition of 0.1M NaOH to this solution. Further, 2 g L-cys was added to the solution and then kept it in a Teflon-lined stainless steel autoclave of 100 mL capacity and heated at  $240^\circ \text{C}$  for 12 h. The autoclave was allowed to cool after 12 h and obtained a black colour product. It was

centrifuged to separate, washed using DI water and ethanol (2:1), and then vacuum dried at 90 °C for 12 h in the oven. A schematic description for the synthesis of MoS<sub>2</sub>@rGO nanohybrid is shown in **Fig. 4.1 (A)**.

#### **4.2.3. Electrophoretic deposition of MoS<sub>2</sub>@rGO nanohybrid and biosensor fabrication**

MoS<sub>2</sub>@rGO nanohybrid as synthesized in the above 4.2.2 section was deposited electrophoretically on a pre-cleaned ITO coated glass electrode. The platinum counter electrode was kept 0.5 cm apart from the ITO coated glass electrode during the electrophoretic deposition. The MoS<sub>2</sub>@rGO nanohybrid colloidal suspension has been sonicated in a mixture solution of DI water and ethanol (1:5) before electrophoretic deposition. The electrophoretic deposition was then carried out for 25 sec by applying a potential (DC 15 V). Magnesium nitrate (10<sup>-4</sup> M) solution was used for smooth deposition, which gets absorbed onto the MoS<sub>2</sub>@rGO nanohybrid, thus creating a positive surface charge [5]. Further, the MoS<sub>2</sub>@rGO/ITO electrodes were incubated for 1 h in a mixture of 5 mM NHS (15μL) and 2 mM EDC (15μL) for the immobilization of antibodies and then stored at room temperature (25 °C). The 20 μL (60 μg mL<sup>-1</sup>) of monoclonal anti-EpCAM was then drop-casted onto the biosensor. All the steps/stages followed in the fabrication of EpCAM based biosensor have been shown in **Fig. 4.1 (B)**.

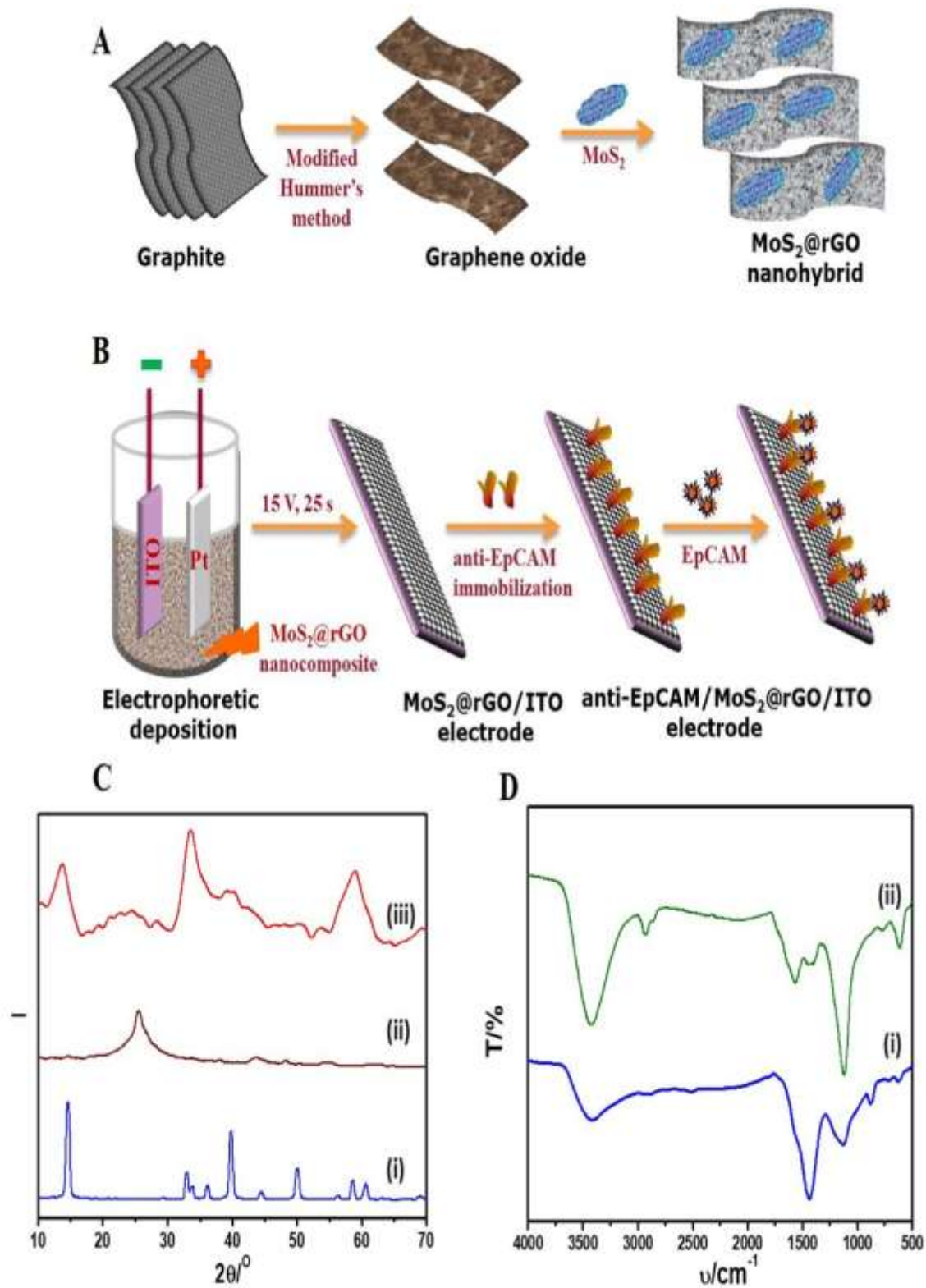


**Figure 4.1.** Scheme for (A) MoS<sub>2</sub>@rGO nanohybrid synthesis (B) fabrication of rGO@MoS<sub>2</sub>/ITO based biosensor (C) XRD curves of (i) MoS<sub>2</sub>, (ii) rGO (iii) MoS<sub>2</sub>@rGO nanohybrid (D) FTIR spectra of (i) rGO (ii) MoS<sub>2</sub>@rGO nanohybrid

### 4. 3. Results and discussion

#### 4.3.1. Characterization of MoS<sub>2</sub>@rGO nanohybrid

The XRD plot of bulk MoS<sub>2</sub> exhibits sharp and strong peaks and the corresponding planes at  $2\theta = 14.35^\circ$  (002),  $32.67^\circ$  (100),  $39.66^\circ$  (103),  $49.74^\circ$  (105), and  $58.60^\circ$  (110) [Fig.4.1 (C), curve i] [6]. The diffraction peaks at  $14.35^\circ$ ,  $32.67^\circ$ , and  $58.60^\circ$  have been observed in the diffraction pattern of MoS<sub>2</sub>@rGO nanohybrid which shows the poor crystalline nature of MoS<sub>2</sub> (curve iii). The poor crystalline behaviour of MoS<sub>2</sub> is found due to the integration of rGO which prevents the layered growth of MoS<sub>2</sub> occurred during the hydrothermal process. The peaks at  $14.25^\circ$ ,  $39.66^\circ$ , and  $49.74^\circ$  have been disappeared after the MoS<sub>2</sub>@rGO nanohybrid formation. Although, the intensity of the peak at  $14.25^\circ$  corresponds to the (002) diffraction plane was decreased drastically in MoS<sub>2</sub>@rGO nanohybrid as shown in (curve ii). This intensity decrease is perhaps due to the rGO presence which hinders the MoS<sub>2</sub> crystal layer growth. From the XRD results, it can be assumed that during the hydrothermal process, L-cys reduced the Mo precursor to MoS<sub>2</sub>, and GO was *in-situ* reduced to rGO [7]. The diffraction peak at  $2\theta \approx 25^\circ$  was hardly observed, showing that the graphene nanosheets were not stacked together [8]. This could be due to the layered MoS<sub>2</sub> which inhibits the rGO stacking.

A broad peak at  $3412\text{ cm}^{-1}$  has been observed in the FTIR spectra of GO which is attributed due to the stretching mode of O-H bond. A characteristic peak at  $1704\text{ cm}^{-1}$  also attributed due to the presence of carboxyl group in the graphene. The peak at  $1634\text{ cm}^{-1}$  may be assigned to the stretching and bending vibrational mode of water molecules. The peak at  $1373\text{ cm}^{-1}$  is due to the presence of the C-OH group, while the other peaks at  $1221$ , and  $1064\text{ cm}^{-1}$  correspond to the stretching and vibrational mode of the C-O group, respectively [9, 10] [Fig. 4.2 (A)]. It is observed from the Fig. 4.1 (D); curve (i) that there is a sharp decline in the peak intensity of oxygen rich functional groups on GO reduction and MoS<sub>2</sub>@rGO nanohybrid formation suggesting the successful reduction of Mo precursor to MoS<sub>2</sub> and GO to rGO. The peak observed at  $603\text{ cm}^{-1}$  in the spectra of



MoS<sub>2</sub>@rGO nanohybrid is attributed due to the Mo–S vibration as shown in Fig. 4.1 (D); curve (ii) [10].

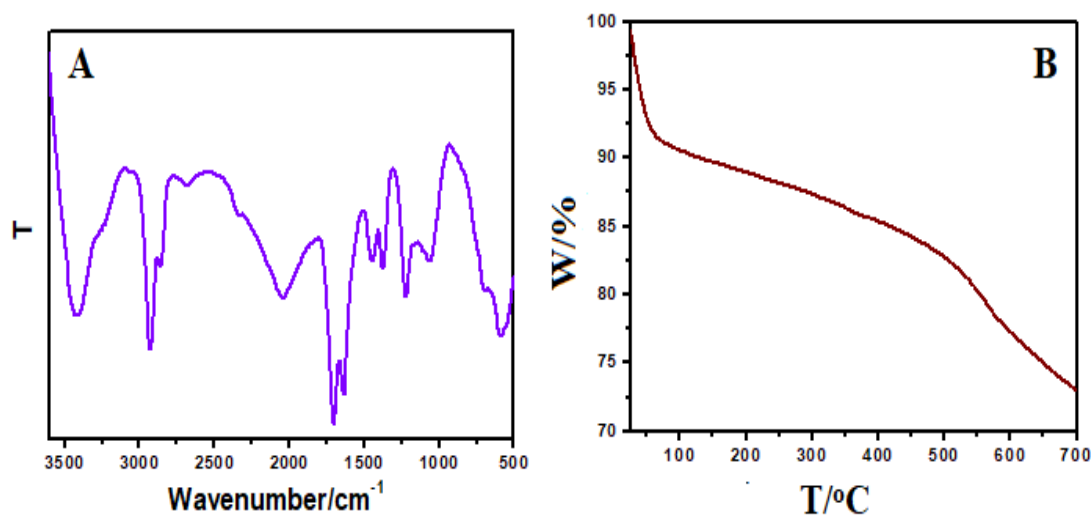


**Figure 4.2.** (A) FTIR spectra of GO and (B) TGA curve for MoS<sub>2</sub>@rGO nanohybrid

The thermal stability of MoS<sub>2</sub>@rGO was carried out using TGA technique at a heating rate of 10 °C/min in an inert environment by purging the N<sub>2</sub> gas. The TGA thermogram has been depicted in the Fig. 4.2 (B). A continuous weight loss from initial temperature with three decomposition stages has been observed in TG curves of MoS<sub>2</sub>@rGO nanohybrid. The weight loss at around 100 °C in the first stage is observed due to the evaporation of water molecules. The weight loss was also found around 350 °C due to the thermal decomposition probably caused by the oxidation of MoS<sub>2</sub> to MoO<sub>3</sub>. A drastic weight loss was observed at 500 °C due to the oxidation of MoS<sub>2</sub>. There was a gradual decrease in the TG curve after 700 °C showing the decrease in the stability of the nanohybrid [11].

#### 4.3.2. Microscopic studies

TEM analysis of rGO and MoS<sub>2</sub>@rGO nanohybrid was conducted to study the surface morphology of these samples. The TEM micrograph of rGO shows the crumpled morphology. It is seen from the Fig. 4.3 (A) that the lateral size of the individual graphene sheets is quite large. The SEM micrograph of rGO/ITO is given in the Fig. 4.3 (B).

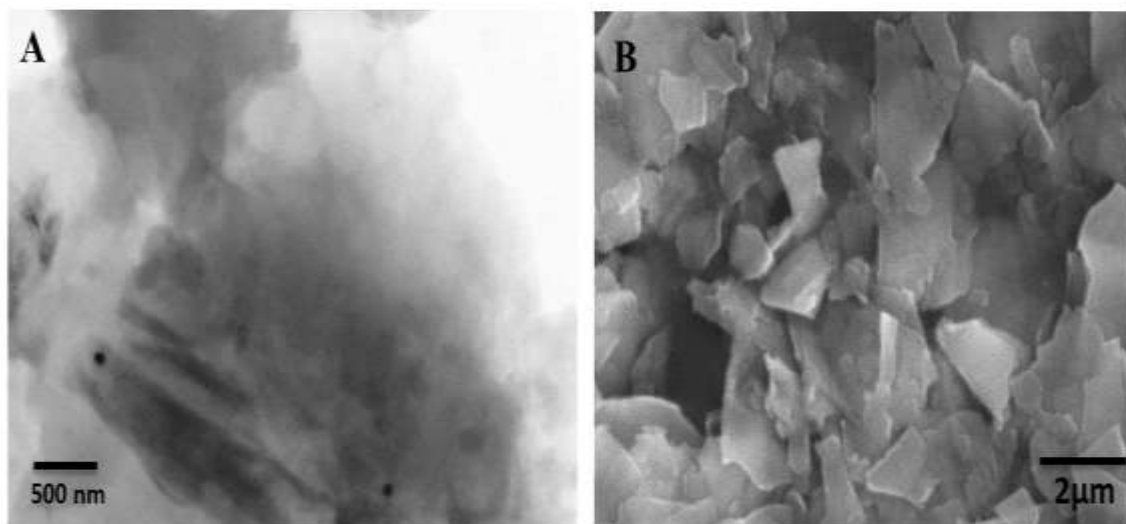


**Figure 4.3.** (A) TEM image of rGO and (B) SEM image of rGO/ITO electrode

The TEM image of  $\text{MoS}_2@\text{rGO}$  nanohybrid exhibits a flower-like architecture constituted by exfoliated nanosheets, where the  $\text{MoS}_2$  nanostructures are well adhered on the rGO surface [Fig. 4.4 (A)] [7]. The thickness and diameter of petal like  $\text{MoS}_2$  nano-sheets are found to be  $\sim 20$  nm and 200–300 nm range, respectively as shown in Fig. 4.4 (B). A lattice fringe with an inter-planar spacing of 0.61 nm corresponds to the  $\text{MoS}_2$  plane 002 may also be noticed in the HRTEM of  $\text{MoS}_2$  as depicted in Fig.4.4 (B), inset.

The SEM micrograph of rGO/ITO electrode reveals an uneven distribution of rGO sheets on the electrode surface as shown in Fig. 4.3 (B). However, the SEM micrograph of  $\text{MoS}_2@\text{rGO}$  nanohybrid shows the 3D hierarchical structures as depicted in Fig. 4.4 (C). It is revealed that the  $\text{MoS}_2$  nanoflower like morphology is made up of  $\text{MoS}_2$  nanosheets anchored on rGO resulting in the formation of three dimensional hierarchical assembly. The structural morphology of the nanohybrid has been changed after immobilizing anti-EpCAM on the  $\text{MoS}_2@\text{rGO}/\text{ITO}$  electrode reveals that the  $\text{MoS}_2@\text{rGO}/\text{ITO}$  electrode surface was covered by anti-EpCAM molecules as shown in Fig. 4.4 (D).

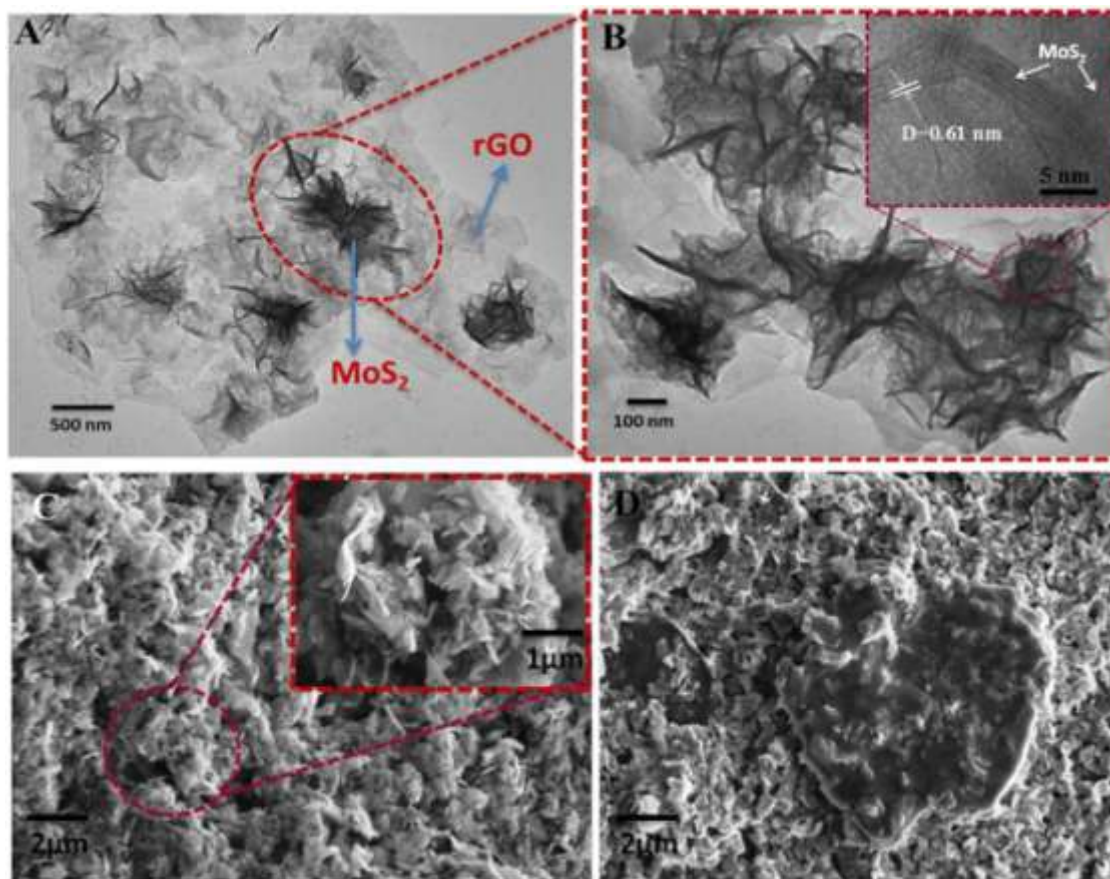


**Figure 4.4.** TEM micrograph of (A & B) MoS<sub>2</sub>@rGO nanohybrid and SEM micrographs of (C) MoS<sub>2</sub>@rGO/ITO electrode and (D) anti-EpCAM/ MoS<sub>2</sub>@rGO/ITO electrode

### 4.3.3. Electrochemical characterization

Electrochemical impedance spectroscopy (EIS; frequency range 0.01-10<sup>5</sup> Hz) was used to study the electrochemical properties of the different modified electrodes [Fig. 4.5 (A)] [12]. The  $R_{ct}$  value of MoS<sub>2</sub>@rGO/ITO electrode was found to be [curve (i); 660.21  $\Omega \pm 1.2$ ] lower in comparison to the rGO/ITO electrode [curve (iii); 1306.16  $\Omega \pm 2.8$ ]. It is attributed due to the synergetic effect of MoS<sub>2</sub> and graphene oxide which improves the electrochemical performance of MoS<sub>2</sub>@rGO/ITO electrode. Further, the  $R_{ct}$  value of MoS<sub>2</sub>@rGO/ITO electrode [996.86  $\Omega \pm 1.7$ ; curve (ii)] was found to increase after immobilization of anti-EpCAM. This increase is reported due to the charge transfer inhibition caused by the non-conducting nature of antibodies. After the incubation of the EpCAM to anti-EpCAM/MoS<sub>2</sub>@rGO/ITO electrode, the  $R_{ct}$  was further increased [curve (iv); 1589.29  $\Omega \pm 2.6$ ] due to the formation of antibody-antigen complex that acts as a barrier by hindering the diffusion of the [Fe(CN)<sub>6</sub>]<sup>3-/4-</sup> to the anti-EpCAM/

MoS<sub>2</sub>@rGO/ITO electrode [13]. The exchange current per geometric unit area ( $i_o$ ) and apparent electron transfer rate constant ( $K_{app}$ ) values have been calculated for different electrodes from the  $R_{ct}$  values by using the equations such as  $i_o = nRT/R_{ct} F$  and  $K_{app} = RT/n^2F^2AR_{ct} C$ , respectively with their appropriate meanings of all symbols used.

The  $i_o$  value for MoS<sub>2</sub>@rGO/ITO electrode was found to be  $15.294 \times 10^{-5} \text{ A cm}^{-2}$ . This  $i_o$  value decreases to  $10.134 \times 10^{-5} \text{ A cm}^{-2}$  after anti-EpCAM immobilization. Similarly, the  $K_{app}$  values for both MoS<sub>2</sub>@rGO/ITO and anti-EpCAM/MoS<sub>2</sub>@rGO/ITO electrodes were calculated as  $4.032 \times 10^{-7} \text{ cm s}^{-1}$  and  $2.135 \times 10^{-7} \text{ cm s}^{-1}$ , respectively. A decrease in  $i_o$  and  $K_{app}$  values is observed for the anti-EpCAM immobilized MoS<sub>2</sub>@rGO/ITO electrode mainly due to the sluggish diffusion of redox ions through the electrode interface.

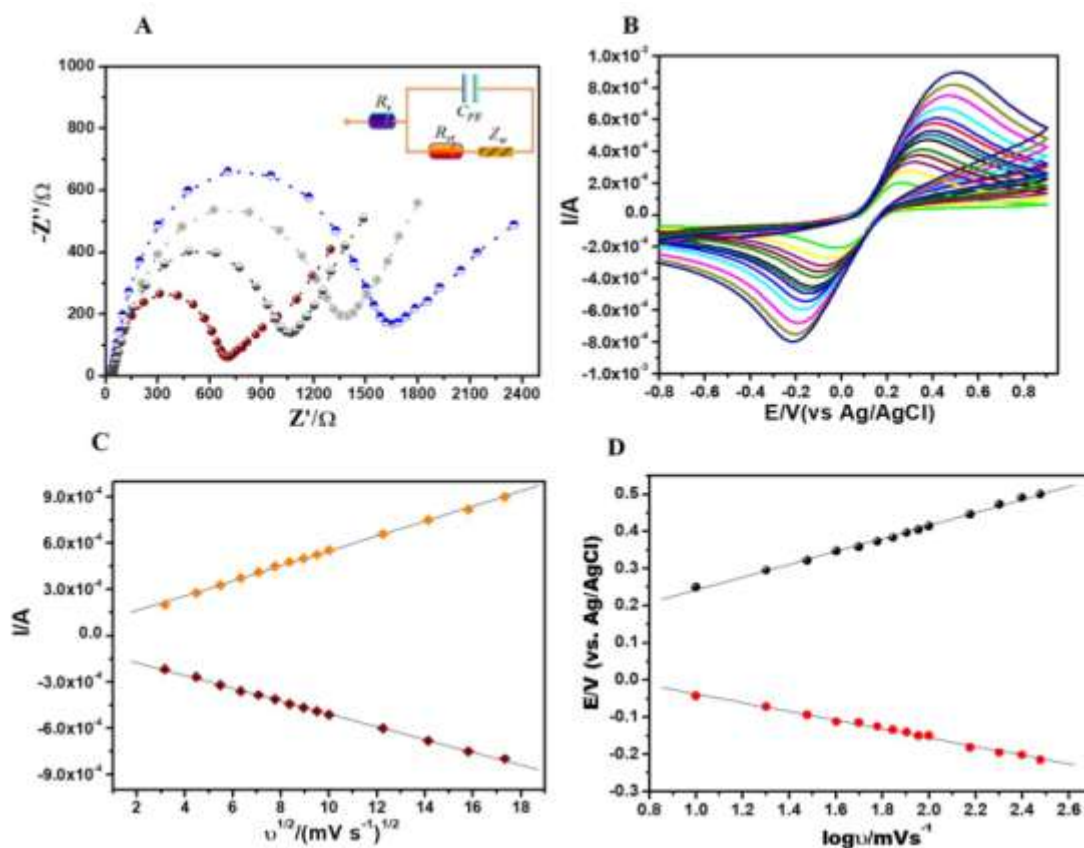


**Figure 4.5.** (A) EIS data of (i) MoS<sub>2</sub>@rGO/ITO (ii) anti-EpCAM/MoS<sub>2</sub>@rGO/ITO (iii) rGO/ITO and (iv) EpCAM treated anti-EpCAM/MoS<sub>2</sub>@rGO/ITO (B) Cyclic voltammogram of MoS<sub>2</sub>@rGO/ITO electrode with scan rate (10-300 mV). Plots of (C)  $I_{pa}$ ,  $I_{pc}$  against square root of scan rate and (D) potential against log of scan rate for MoS<sub>2</sub>@rGO/ITO electrode

Cyclic voltammetry (CV) studies have been carried out in PBS containing 5 mM  $[\text{Fe}(\text{CN})_6]^{3-/4-}$  by changing the scan rate ( $v$ ) from 10-300  $\text{mV s}^{-1}$  [Fig. 4.5 (B)]. These

results reveal that there is a linear relationship between peak current and the square root of scan rate for MoS<sub>2</sub>@rGO/ITO electrode. It is clearly showing that the electron transfer in MoS<sub>2</sub>@rGO/ITO electrode is a surface-controlled process which follows equations 4.1 & 4.2 [Fig. 4.5 (C)]. It was also reported that there was an increase in the oxidation and reduction peaks when  $v$  (10-300 mV sec<sup>-1</sup>) was increases. It indicates the linear dependence of peak potentials on log  $v$  (Eq. 4.3 & 4.4) [Fig. 4.5 (D)].

$$I_{pa}[\text{MoS}_2@\text{rGO}/\text{ITO}] = 65.707 \mu\text{A} + 48.370 \mu\text{A} (s/mV) \times v (mV/s); R^2 = 0.9992 \quad \text{Eq. 4.1}$$

$$I_{pc}[\text{MoS}_2@\text{rGO}/\text{ITO}] = -93.250 \mu\text{A} - 41.406 \mu\text{A} (s/mV) \times v (mV/s); R^2 = 0.9995 \quad \text{Eq. 4.2}$$

$$E_{pa}[\text{MoS}_2@\text{rGO}/\text{ITO}] = 0.0685 (V) + 0.1734 (V) \times \log [v (mV/s)]; R^2 = 0.9982 \quad \text{Eq. 4.3}$$

$$E_{pc}[\text{rGO}@MoS_2/\text{ITO}] = 0.0806 (V) - 0.1178 (V) \times \log [v (mV/s)]; R^2 = 0.9968 \quad \text{Eq. 4.4}$$

Based on the above linearity curves and Randle Sevcik equation such as  $I_p = (2.99 \times 10^5) \alpha^{1/2} n^{3/2} ACD^{1/2}v^{1/2}$ , the diffusion coefficient (D) was calculated for the MoS<sub>2</sub>@rGO/ITO electrode as  $3.19 \times 10^{-6} \text{ cm}^2 \text{ s}^{-1}$ .

#### 4.3.4. Optimization of biosensing parameters for efficient bioelectrode response

The various biosensing parameters have been optimized for the optimal bioelectrode response. This response governs an efficient detection of EpCAM. The optimal concentration requirement for binding the anti-EpCAM on MoS<sub>2</sub>@rGO/ITO was estimated by using DPV. The different concentrations of anti-EpCAM were covalently immobilized on the MoS<sub>2</sub>@rGO/ITO by using EDC-NHS as a linker. It is observed that there was a decrease in DPV peak current on subsequent addition of anti-EpCAM in the concentration range of 10-80  $\mu\text{g mL}^{-1}$  and reached to a plateau at EpCAM concentration at 60  $\mu\text{g mL}^{-1}$  [Fig 4.6 (A)]. Thus, 60  $\mu\text{g mL}^{-1}$  of anti-EpCAM concentration has been used for the fabrication of the immunosensor. The pH of the electrolytic solution also affects the performance of the biosensor. Therefore, the DPV studies of anti-EpCAM/MoS<sub>2</sub>@rGO/ITO electrode towards 10  $\text{ng mL}^{-1}$  have been carried out at different pH values from 5.4 to 9.4. The highest current response was measured at pH 7.4 which

shows an ideal pH for these biosensing studies [Fig 4.6 (B)] in the present work. Furthermore, the time for EpCAM incubation on the surface of anti-EpCAM/MoS<sub>2</sub>@rGO/ITO electrode was studied by changing the incubation time from 0 to 15 min [Fig 4.6 (C)]. It was seen that the DPV current saturates after 10 min. It reveals that the maximum binding has been achieved during this period.

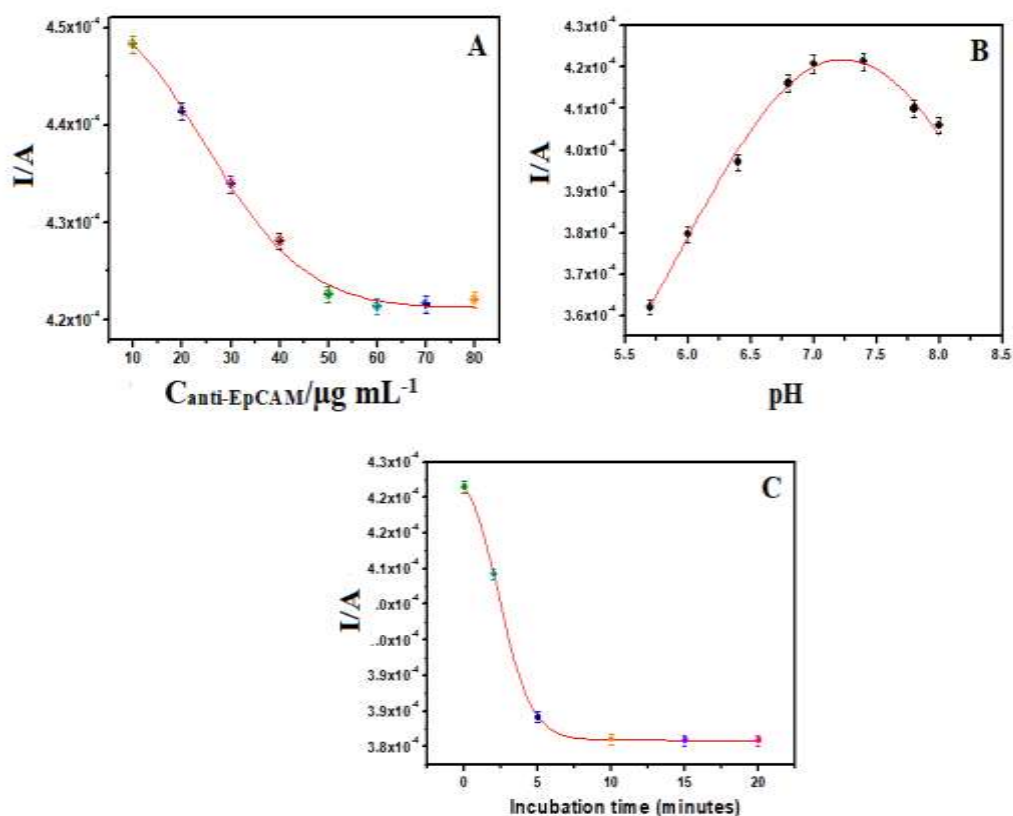


**Figure 4.6.** Optimization of the (A) anti-EpCAM ( $10$  to  $80 \mu\text{g}\cdot\text{mL}^{-1}$ ) concentration, (B) incubation time of EpCAM and (C) pH condition for efficient detection of EpCAM.

#### 4.3.5. Electrochemical response studies

The biosensing studies of anti-EpCAM/MoS<sub>2</sub>@rGO/ITO electrode have been carried out at different concentrations of EpCAM antigen ranging from  $0.001$  to  $20 \text{ ng mL}^{-1}$ . Fig. 4.7 (A) indicates that the anodic peak current decreases in a linear manner when the EpCAM concentration was increased in the range of  $0.001$  to  $20 \text{ ng mL}^{-1}$ . An increase in EpCAM concentration on the anti-EpCAM/MoS<sub>2</sub>@rGO/ITO electrode surface shows a decrease in peak current. This decrease in peak current is found due to the development of insulating layers which hinder the electrons transport. Fig. 4.7 (B) shows a good linear relationship of

the current response with different EpCAM concentrations. It is revealed based on the slope obtained from the calibration plot against the EpCAM concentration. The sensitivity of the biosensor was calculated as slope/surface area by using the regression equation which is represented as  $I_p = 0.412 \text{ mA} - 0.026 \text{ mA/ng/mL} \times \text{EpCAM concentration ng/mL}$ . The sensitivity value is found to be  $0.104 \text{ mA ng}^{-1} \text{ mL cm}^{-2}$  with  $R^2$  of 0.9985. The LOD was estimated to be  $44.22 \pm 0.21 \text{ fM}$  using the equation  $3\sigma/S$ , where  $\sigma$  is the standard deviation of the bioelectrode and  $S$  is the sensitivity obtained from the slope of the calibration curve [14]. This low value may be due to the hierarchical structure of  $\text{MoS}_2@\text{rGO}$  nanohybrid. It provides the higher surface area which improves the electronic and electrochemical properties. Further, the enhanced sensing results of this biosensor are due to the synergetic effects of the robust hybrid structure of  $\text{MoS}_2$  and rGO. The presence of rGO acts as an efficient electron promoter, while the  $\text{MoS}_2$  has increased the loading of anti-EpCAM, leading to the increased interaction between EpCAM and the antibodies [15].



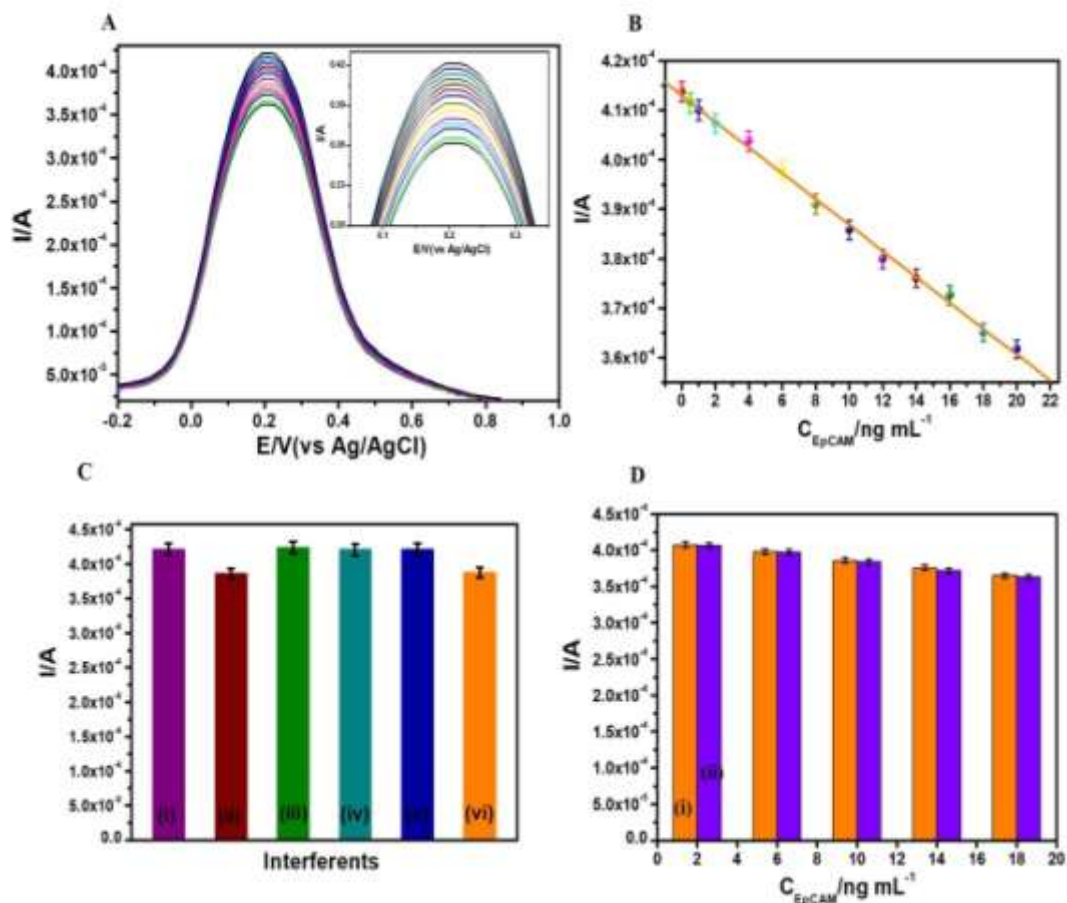


**Figure 4.7.** DPV studies response of (A) anti-EpCAM/MoS<sub>2</sub>@rGO/ITO as a function of EpCAM concentration; inset is the magnified view of oxidation peak current (B) Calibration plot between the magnitudes of current recorded and EpCAM concentration (0.001-20 ng mL<sup>-1</sup>) (C) Specificity studies of the fabricated biosensor with (i) EpCAM (ii) glucose (iii) NaCl (iv) IgG (v) EpCAM + other interferences (D) Electrochemical response of the biosensor in (i) buffer sample and (ii) spiked human serum sample.

#### 4.3.6. Selectivity, reusability and shelf life studies of the biosensor

The cross-reactivity of the biosensor against exposure to other biomolecules present with EpCAM was estimated by analyzing its electrochemical performance. These electrochemical performances were carried out in the presence of sodium chloride (NaCl), glucose, immunoglobulin G (IgG), and the mixture of interferences as shown in Fig 4.7 (C). When the biosensor was incubated with glucose, IgG and NaCl, a negligible change in peak current was observed. While, it shows a current decrease when the bioelectrode was exposed to a mixture of EpCAM and other analytes. This peak current was found similar to the case of EpCAM interaction with anti-EpCAM/MoS<sub>2</sub>@rGO/ITO electrode. The



selectivity coefficient ( $K_{sel}$ ) was also calculated to study the interference effect using the following Eq. 4.5. The  $K_{sel}$  value has been found  $\sim 1$  [16] for all the interferents.

$$K_{sel} = \frac{Signal_{interferent}}{Signal_{EpCAM}} \quad (4.5)$$

#### 4.3.7. Validation of biosensor with human serum samples

The application and validation of MoS<sub>2</sub>@rGO/ITO based biosensor were studied in biological samples like human serum, urine, and saliva by spiking them with EpCAM. The 300  $\mu$ L of biological samples (50%) were spiked with 10 ng mL<sup>-1</sup> of EpCAM antigen (20  $\mu$ L). Also, the human biological samples were diluted with the buffer prior to the analysis. A decrease in peak current was reported when the biosensor was incubated with spiked biological samples. However, for the blank biological samples (non-spiked), the peak current observed was nearly similar to that of anti-EpCAM/MoS<sub>2</sub>@rGO/ITO electrode [17]. The % recoveries for the spiked samples were calculated which is found to be in the range of 91.2 to 99.8 %, with RSD of <8.7% (n=3). These various data are presented in the Table 4.1.

**Table 4.1:** Recoveries of EpCAM spiked to different samples

Sample	EpCAM added (ng mL <sup>-1</sup> )	EpCAM found (ng mL <sup>-1</sup> )	Recovery (%)	Relative Standard Deviation (RSD) %
Buffer	10	9.98	99.8	4.2
Saliva	10	9.12	91.2	8.7
Serum	10	9.58	95.8	6.5
Urine	10	9.62	96.2	5.4

The electrochemical response has been measured with spiked human serum samples with different EpCAM concentrations ranging from 2-18 ng mL<sup>-1</sup> to determine the potential of anti-EpCAM/MoS<sub>2</sub>@rGO/ITO electrode in clinical applications. Fig. 4.7 (D) shows a continuous decrease in the response current on increasing the EpCAM concentration. The recoveries have also been measured with the spiked human serum samples with RSD <5.4% (n=3) and presented in Table 4.2.

**Table 4.2.** Different EpCAM concentrations data found in spiked serum samples

S No.	Spiked EpCAM concentration (ng·mL <sup>-1</sup> )	Recovered EpCAM concentration (ng·mL <sup>-1</sup> )	% Recovery	Relative Standard Deviation (RSD) % (n=3)
1	2	1.98	99.00	1.2
2	6	5.89	98.17	1.8
3	10	9.71	97.10	5.2
4	14	13.84	98.86	2.5
5	18	17.49	97.17	5.4

#### 4.3.8. Reusability and shelf-life

The shelf-life and reusability of the biosensor are two essential parameters to determine its performance in the real biological samples. The reusability parameter was investigated by dipping the electrode in 5 M urea solution at 37 °C for 5 min and then rinsed it with Tris-HCl buffer. The results were obtained for the different regeneration cycles as shown in Fig. 4.8 (A). These results reveal that the biosensor shows an excellent regenerability and it can be reused over 4 times. The shelf-life of the biosensor was measured by using the DPV response of bioelectrodes (3 sets) towards EpCAM (10 ng mL<sup>-1</sup>) with an interval of 5 days as shown in Fig. 4.8 (B). It is observed that there is a negligible change in the current response once compared to the original current response (RSD < 4.2% (n=3)). It shows the good stability of the biosensor up to 45 days when it was stored at 4 °C.

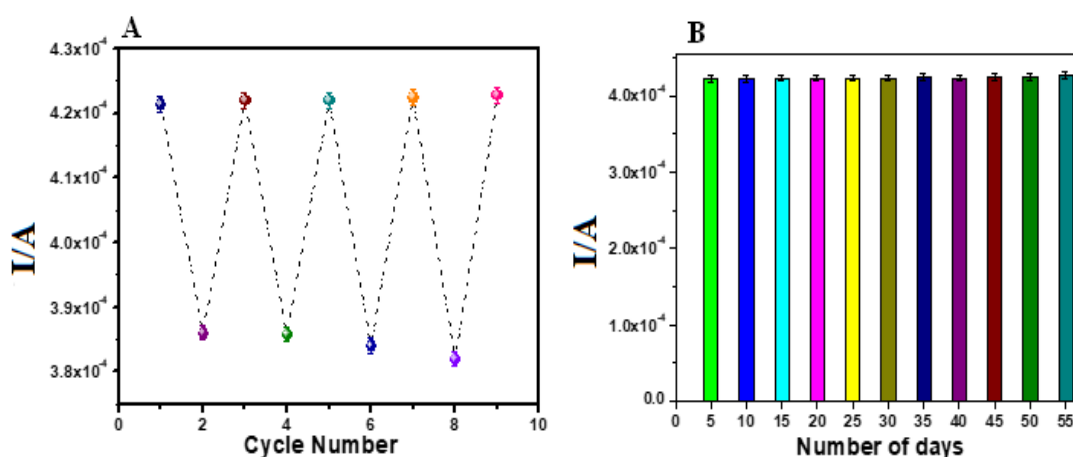


**Figure 4.8.** (A) Regeneration studies of the biosensor for EpCAM detection (B) Variation of anti-EpCAM/MoS<sub>2</sub>@rGO/ITO electrode response towards EpCAM over a period of 55 days.

#### 4.4. Conclusion

A facile and environment-friendly route has been reported for the synthesis of MoS<sub>2</sub>@rGO nanohybrid using an amino acid assisted solution-phase method in this chapter. This MoS<sub>2</sub>@rGO nanohybrid exhibits an improved electrochemical performance. Further, the label-free detection of EpCAM has been carried out by covalently immobilization of epithelial cell adhesion molecule antibodies (specific to cancer biomarker) on the MoS<sub>2</sub>@rGO/ITO electrodes. It is revealed from the electrochemical results that the anti-EpCAM/MoS<sub>2</sub>@rGO/ITO biosensor detects EpCAM in 0.001-20 ng mL<sup>-1</sup> concentration range with a detection limit of 44.22 fg mL<sup>-1</sup> (S/N=3). This excellent performance is attributed due to the efficient immobilization of antibodies on MoS<sub>2</sub>@rGO surface. This MoS<sub>2</sub>@rGO nanohybrid based novel sensing platform shows a reasonable detection limit, stability and reusability. Further, a successful detection of EpCAM antigen in spiked samples like human saliva, serum and urine promotes this platform as an alternate method for an early screening of the cancer biomarkers.

*The results of present study have been published in Bioelectrochemistry (2021), 138, 107733.*

## References

- [1] WS Hummers Jr, RE Offeman, Preparation of graphitic oxide, *Journal of American Chemical Society*, 80(1958) 1339-.
- [2] J Chen, B Yao, C Li, G Shi, An improved Hummers method for eco-friendly synthesis of graphene oxide, *Carbon*, 64(2013) 225-9.
- [3] D Chen, L Li, L Guo, An environment-friendly preparation of reduced graphene oxide nanosheets via amino acid, *Nanotechnology*, 22(2011) 325601.
- [4] K Chang, W Chen, L-cysteine-assisted synthesis of layered MoS<sub>2</sub>/graphene composites with excellent electrochemical performances for lithium ion batteries, *ACS nano*, 5(2011) 4720-8.
- [5] O Jalil, CM Pandey, D Kumar, Electrochemical biosensor for the epithelial cancer biomarker EpCAM based on reduced graphene oxide modified with nanostructured titanium dioxide, *Microchimica Acta*, 187(2020) 1-9.
- [6] L Zheng, D Ye, L Xiong, J Xu, K Tao, Z Zou, et al., Preparation of cobalt-tetraphenylporphyrin/reduced graphene oxide nanocomposite and its application on hydrogen peroxide biosensor, *Analytica chimica acta*, 768(2013) 69-75.
- [7] J He, P Li, W Lv, K Wen, Y Chen, W Zhang, et al., Three-dimensional hierarchically structured aerogels constructed with layered MoS<sub>2</sub>/graphene nanosheets as free-standing anodes for high-performance lithium ion batteries, *Electrochimica Acta*, 215(2016) 12-8.
- [8] Y Liu, Y Zhao, L Jiao, J Chen, A graphene-like MoS<sub>2</sub>/graphene nanocomposite as a highperformance anode for lithium ion batteries, *Journal of Materials Chemistry A*, 2(2014) 13109-15.
- [9] K Chang, W Chen, Single-layer MoS<sub>2</sub>/graphene dispersed in amorphous carbon: towards high electrochemical performances in rechargeable lithium ion batteries, *Journal of Materials Chemistry*, 21(2011) 17175-84.
- [10] R Vinoth, IM Patil, A Pandikumar, BA Kakade, NM Huang, DD Dionysios, et al., Synergistically enhanced electrocatalytic performance of an N-doped graphene quantum

dot-decorated 3D MoS<sub>2</sub>-graphene nanohybrid for oxygen reduction reaction, *Acs Omega*, 1(2016) 971-80.

[11] A Bahuguna, S Kumar, V Sharma, KL Reddy, K Bhattacharyya, P Ravikumar, et al., Nanocomposite of MoS<sub>2</sub>-rGO as facile, heterogeneous, recyclable, and highly efficient green catalyst for one-pot synthesis of indole alkaloids, *ACS Sustainable Chemistry & Engineering*, 5(2017) 8551-67.

[12] J-B Jorcin, ME Orazem, N Pébère, B Tribollet, CPE analysis by local electrochemical impedance spectroscopy, *Electrochimica Acta*, 51(2006) 1473-9.

[13] Y Xie, A Chen, D Du, Y Lin, Graphene-based immunosensor for electrochemical quantification of phosphorylated p53 (S15), *Analytica chimica acta*, 699(2011) 44-8.

[14] J Shi, J Lyu, F Tian, M Yang, A fluorescence turn-on biosensor based on graphene quantum dots (GQDs) and molybdenum disulfide (MoS<sub>2</sub>) nanosheets for epithelial cell adhesion molecule (EpCAM) detection, *Biosensors and Bioelectronics*, 93(2017) 182-8.

[15] S Augustine, P Kumar, BD Malhotra, Amine-functionalized MoO<sub>3</sub>@rGO nanohybrid-based biosensor for breast cancer detection, *ACS Applied Bio Materials*, 2(2019) 5366-78.

[16] S Verma, P Arya, A Singh, J Kaswan, A Shukla, HR Kushwaha, et al., ZnO-rGO nanocomposite based bioelectrode for sensitive and ultrafast detection of dopamine in human serum, *Biosensors and Bioelectronics*, 165(2020) 112347.

[17] Q Chen, W Hu, B Shang, J Wei, L Chen, X Guo, et al., Ultrasensitive amperometric aptasensor for the epithelial cell adhesion molecule by using target-driven toehold-mediated DNA recycling amplification, *Microchimica Acta*, 185(2018) 1-8.

*CHAPTER 5*  
*TiO<sub>2</sub> Grafted MoS<sub>2</sub>@GO-Based Biosensor for Cancer  
biomarker detection*

---

## **5.1. Introduction**

Nanostructured titanium dioxide (TiO<sub>2</sub>) is one of the most valued n-type semiconductors. It is extensively used in biomedical applications due to its biocompatibility, photocatalytic activity and good mechanical properties. However, to improve the sensing performance of TiO<sub>2</sub>, strategic solutions are being done to form hybrid materials of TiO<sub>2</sub> with a variety of materials to serve better its functional characteristics [1]. The integration of TiO<sub>2</sub> with semiconducting materials such as CuO, Fe<sub>2</sub>O<sub>3</sub>, MoS<sub>2</sub> etc. leads to a narrow band gap and offers better interfacial charge transfer leading to an improvement in conducting behaviour of the material [2, 3]. Recently, MoS<sub>2</sub>/rGO/TiO<sub>2</sub> hybrids have also been used as anodic material for sodium ion batteries, in photocatalysis and adsorption applications. It is believed that heterojunction formed between TiO<sub>2</sub> and MoS<sub>2</sub> onto rGO can accelerate the electron transfer [4, 5].

In this Chapter, we have presented the synthesis, characterization and application of TiO<sub>2</sub> grafted MoS<sub>2</sub>@GO nanohybrid for cancer biomarker detection. The electrodes have been fabricated by electrophoretically depositing TiO<sub>2</sub>/MoS<sub>2</sub>@GO nanohybrid onto ITO coated glass substrate followed by covalent immobilization of anti-EpCAM. The reproducibility, repeatability, linear working range, detection limit, and stability of anti-EpCAM/TiO<sub>2</sub>/MoS<sub>2</sub>@GO/ITO electrode for the detection of EpCAM were examined thoroughly and reported in the following sections.

## **5.2. Experimental section**

### **5.2.1. Synthesis, of TiO<sub>2</sub>/MoS<sub>2</sub>@GO nanohybrid**

The synthesis of GO from graphite and its reduction has already been discussed in Chapter III and IV. The TiO<sub>2</sub> nanoparticles were synthesized as reported earlier, and discussed in Chapter III. For the synthesis of TiO<sub>2</sub>/MoS<sub>2</sub>@GO nanohybrid, 80 mg of GO was taken in

40 mL of DI water and then ultrasonicated for 30 min.  $\text{TiO}_2$  nanoparticles (2 mg) along with 0.64 g of  $\text{Na}_2\text{MoO}_4 \cdot 2\text{H}_2\text{O}$  have been added to the above mentioned solution which again ultrasonicated followed by stirring for 30 min. This resulting solution was put into the 100 mL capacity Teflon-lined stainless steel autoclave and heated at  $200\text{ }^\circ\text{C}$  for 20 h. After cooling this solution, it was centrifuged, filtered and collected the precipitate. The precipitate so obtained was washed with DI water and ethanol and then dried it in a vacuum oven at  $100\text{ }^\circ\text{C}$  for 18 h. The different steps involved in the fabrication of  $\text{TiO}_2/\text{MoS}_2@\text{GO}$  nanohybrid based biosensor have also been shown in **Fig. 5.1**.

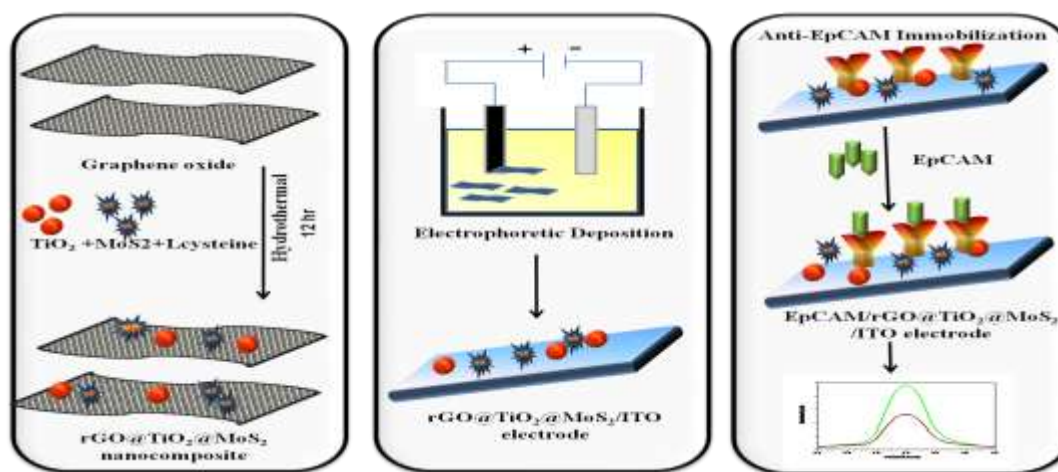


**Figure 5.1.** Scheme showing the synthesis and fabrication of  $\text{TiO}_2/\text{MoS}_2@\text{GO}$  nanohybrid based biosensor for cancer biomarker detection

### 5.2.2. Fabrication of the bioelectrode

EPD technique has been used to deposit the synthesized nanohybrids onto a pre-cleaned ITO coated glass substrate. The colloidal solution of  $\text{TiO}_2/\text{MoS}_2@\text{GO}$  nanohybrid in DI water was taken in 25 mL beaker. The solution was further diluted with ethanol and then electrophoretic deposition was carried out for 10 sec by applying a DC potential (10 V). For the preparation of the bioelectrode,  $\text{TiO}_2/\text{MoS}_2@\text{GO}/\text{ITO}$  electrode was incubated with EDC ( $10\mu\text{L}$ , 5mM) and NHS ( $10\mu\text{L}$ , 5mM) and then kept at room temperature for 2 h. Further,  $20\mu\text{L}$  of monoclonal anti-EpCAM was drop-casted onto the  $\text{TiO}_2/\text{MoS}_2@\text{GO}/\text{ITO}$  electrode and then kept overnight in a humid chamber.

## 5. 3. Results and discussion

### 5.3.1. Characterization of hybrid nanocomposite

The XRD pattern of GO, MoS<sub>2</sub> and TiO<sub>2</sub> has already been discussed in Chapter III and IV. The XRD data of TiO<sub>2</sub>/MoS<sub>2</sub>@GO nanohybrid illustrate the characteristics peaks of TiO<sub>2</sub> at 25°, 38°, 48°, 53.5°, 55°, 62.7°, 69°, 70°, and 75°, which correspond to 101, 004, 200, 105, 211, 204, 110, 200, 215 and 224 planes, respectively [6]. Whereas, the diffraction peaks at 14.4°, 32.7°, 39°, 44°, 49.8° and 60.48° correspond to 002, 100, 103, 006, 105 and 110 planes of MoS<sub>2</sub> [7]. However, the diffraction peak at 10° corresponding to 111 plane of GO is not prominent which signifies that GO has been successfully reduced to rGO as shown in **Fig 5.2 (A)**.

As we know that the Raman spectroscopy provides the evidence of the inelastic-Raman scattering of a molecule irradiated by a monochromatic light generally a laser. The Raman spectra of GO reveal two bands, i.e., D and G which signifies the disorder bands and the tangential bands, respectively [**Fig 5.2 (B); curve i**]. In the spectra of GO, D vibration band is obtained from photons of A<sub>1g</sub> symmetry, which can be observed at 1348.84 and 1355.48 cm<sup>-1</sup> for GO and rGO, respectively. However, the G vibration bands of E<sub>2g</sub> phonons by sp<sup>2</sup> hybridized carbon atoms were observed at 1602.15 for GO and 1582.92 cm<sup>-1</sup> for rGO. The intense bands observed at 146.59, 199.89, 280.66 and 666.39 cm<sup>-1</sup> are characteristics for TiO<sub>2</sub> nanoparticles [8]. The other bands observed at 816.24 and 993.88 cm<sup>-1</sup> correspond to MoS<sub>2</sub> as shown in **Fig 5.2 (B); curve (ii)** [9].

TGA was performed to confirm the effect of temperature on the synthesized nanohybrids. It has been observed that each curve displays multiple stages of decomposition. It is showing that MoS<sub>2</sub>@GO degraded [**Fig 5.2 (C); curve (i)**] more steeply as compared to TiO<sub>2</sub>/MoS<sub>2</sub>@GO nanohybrid [**Fig 5.2 ©; curve (ii)**], confirming that the TiO<sub>2</sub>/MoS<sub>2</sub>@GO nanohybrid is more stable than MoS<sub>2</sub>@GO. The TGA curve of TiO<sub>2</sub>/MoS<sub>2</sub>@GO nanohybrid shows an initial mass loss around 100°C because of the removal of water/moisture. In the second stage, these results reveal that the weight loss at 100-300°C



might attribute to thermal decomposition of the organic surface groups.

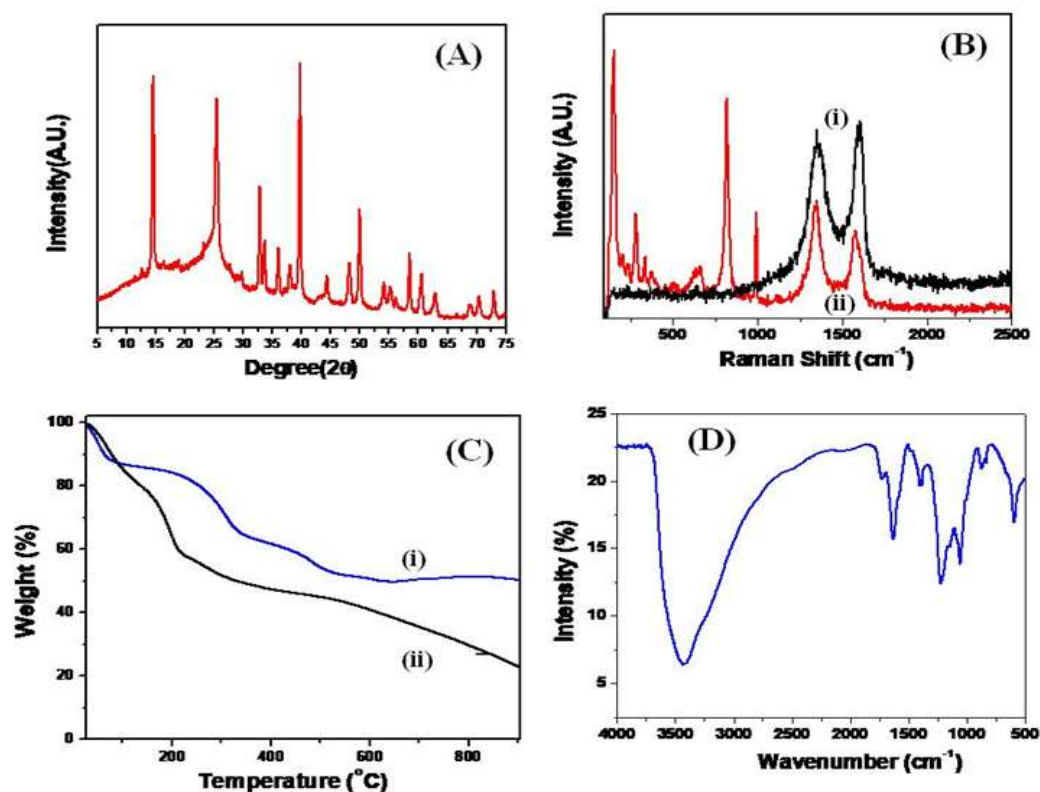


**Figure 5.2.** (A) XRD pattern of TiO<sub>2</sub>/MoS<sub>2</sub>@GO nanohybrid (B) Raman spectra of (i) rGO (ii) TiO<sub>2</sub>/MoS<sub>2</sub>@GO nanohybrid (C) TGA plot of (i) TiO<sub>2</sub>/MoS<sub>2</sub>@GO nanohybrid and (ii) MoS<sub>2</sub>@GO nanohybrid (D) FTIR spectra of TiO<sub>2</sub>/MoS<sub>2</sub>@GO nanohybrid

The FTIR spectra of TiO<sub>2</sub>/MoS<sub>2</sub>@GO nanohybrid show that the GO is successfully reduced to rGO. Most of the oxygen containing functional groups of GO are weakened or completely disappeared in the spectra proving the same inference. The wide absorption peak appearing at about 600 cm<sup>-1</sup>, attributed due to the vibration of Ti–O–Ti of TiO<sub>2</sub> [10]. In addition, the absorption peak indexed at 930 cm<sup>-1</sup> is the representative absorption peak of MoS<sub>2</sub> attributing to the vibration of the Mo-S band [11].

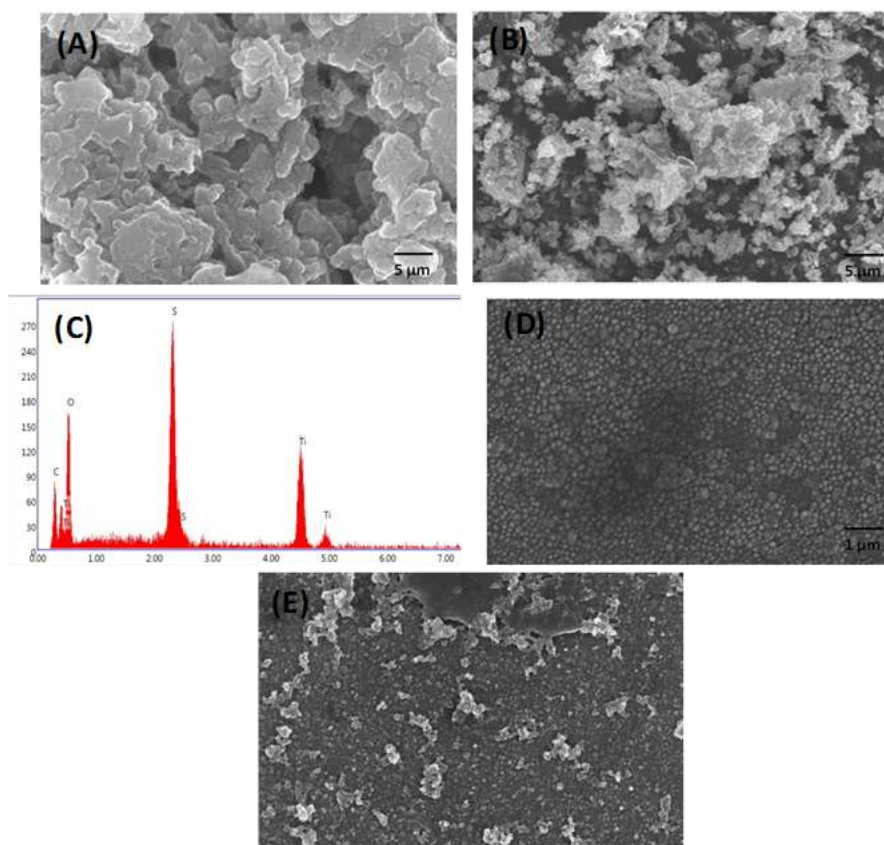


**Figure 5.3.** SEM image of (A) MoS<sub>2</sub>@GO nanohybrid (B) TiO<sub>2</sub>/MoS<sub>2</sub>@GO nanohybrid (C) EDX of TiO<sub>2</sub>/MoS<sub>2</sub>@GO nanohybrid. SEM image of (D) TiO<sub>2</sub>/MoS<sub>2</sub>@GO/ITO electrode and (E) anti-EPCAM/TiO<sub>2</sub>/MoS<sub>2</sub>@GO/ITO electrode

The field emission scanning electron microscopy (FE-SEM) images of the MoS<sub>2</sub>@GO nanohybrid show a thin layer of wrinkled GO while the MoS<sub>2</sub> was observed as aggregates in between the GO sheets [Fig.5.3.(A)]. Moreover, MoS<sub>2</sub> is well dispersed on the GO due to the large surface of GO suggesting that the MoS<sub>2</sub> nanosheets are anchored on the rGO and formed a hierarchical structure. The SEM micrograph of TiO<sub>2</sub>/MoS<sub>2</sub>@GO nanohybrid is shown in Fig. 5.3 (B). It can be revealed from the image that TiO<sub>2</sub> nanoparticles are completely and uniformly wrapped by the network-like MoS<sub>2</sub>@GO [Fig.5.3.(B)].

The energy dispersive x-ray spectroscopy (EDAX or EDS) analysis shows that C, O, Ti, Mo, and S elements are indexed without any impurity or elements only which indicates that the high purity level of the our sample. The EDS element mapping of TiO<sub>2</sub>/MoS<sub>2</sub>@GO nanohybrid also shows [Fig. 5.3. (C)] that the C, O, Ti, Mo and S elements are uniformly distributed thoroughly in the composite. It demonstrates that the

TiO<sub>2</sub>/MoS<sub>2</sub>@GO nanohybrid has been successfully synthesized via hydrothermal process. Further, the SEM image of TiO<sub>2</sub>/MoS<sub>2</sub>@GO/ITO electrode shows the even deposition of the synthesized nanohybrid onto the ITO electrode [Fig. 5.3. (D)]. Globular structures have been observed when the electrode was incubated with anti-EpCAM antibodies, showing that the biomolecule has adhered completely on the surface of the TiO<sub>2</sub>/MoS<sub>2</sub>@GO/ITO electrode [Fig. 5.3. (E)].

### 5.3.2 Electrochemical characterization of fabricated electrodes

CV studies have been carried out to understand the electron transfer process in the fabricated TiO<sub>2</sub>/MoS<sub>2</sub>@GO/ITO electrode and anti-EpCAM/TiO<sub>2</sub>/MoS<sub>2</sub>@GO/ITO electrode. These studies were carried out by varying the scan rate from 10 to 300 mV sec<sup>-1</sup>. The results show that the current is proportional to the square root of scan rate [Fig. 5.4 (A)], revealing the linear dependence of peak currents to the scan rate indicating the electron transfer on MoS<sub>2</sub>@TiO<sub>2</sub>/GO/ITO electrode is a surface controlled process [12].

$$I_{pa} (\mu A) [\text{TiO}_2/\text{MoS}_2@\text{GO}/\text{ITO}] = 112.01 \mu A + 68.5 \mu A (\text{s/mV}) \times \text{scan rate (mV/s)},$$

$$R^2=0.997 \quad \text{Eq. 5.1}$$

$$I_{pc} (\mu A) [\text{TiO}_2/\text{MoS}_2@\text{GO}/\text{ITO}] = -142.80 \mu A - 48.07 \mu A (\text{s/mV}) \times \text{scan rate (mV/s)},$$

$$R^2=0.994 \quad \text{Eq. 5.2}$$

$$I_{pa} (\mu A) [\text{anti-EpCAM}/\text{TiO}_2/\text{MoS}_2@\text{GO}/\text{ITO}] = 96.25 \mu A + 58.75 \mu A (\text{s/mV}) \times \text{scan rate (mV/s)},$$

$$R^2=0.997 \quad \text{Eq. 5.3}$$

$$I_{pc} (\mu A) [\text{anti-EpCAM}/\text{TiO}_2/\text{MoS}_2@\text{GO}/\text{ITO}] = -130.84 \mu A - 41.40 \mu A (\text{s/mV}) \times \text{scan rate (mV/s)},$$

$$R^2=0.992 \quad \text{Eq. 5.4}$$

When scan rate ( $\nu$ ) was varied from 10 to 300 mV sec<sup>-1</sup>, the oxidation peak drifts to a more positive value while the reduction peak towards the more negative value. It shows clearly that the both peak potentials are linearly dependent on  $\log \nu$  as shown in Fig. 5.4 (B). There are two straight lines (Eq. 5.3 & 5.4) obtained giving anodic and cathodic slopes of  $2.303RT/(1-\alpha)nF$  and  $-2.303RT/\alpha nF$ , respectively.

$$E_p (\text{V}) [\text{TiO}_2/\text{MoS}_2@\text{GO}/\text{ITO}] = 0.133 (\text{V}) + 0.0667 (\text{V}) \times \log [\text{scan rate (mV/s)}];$$

$$R^2 = 0.980 \quad \text{Eq. 5.5}$$

$$E_c \text{ (V) [TiO}_2\text{/MoS}_2\text{@GO/ITO]} = 0.130\text{(V)} - 0.052 \text{ (V)} \times \log [\text{scan rate (mV/s)}];$$

$$R^2 = 0.994 \quad \text{Eq. 5.6}$$

$$E_p \text{ (V) [anti-EpCAM/TiO}_2\text{/MoS}_2\text{@GO/ITO]} = 0.132 \text{ (V)} + 0.061 \text{ (V)} \times \log [\text{scan rate (mV/s)}]; R^2 = 0.994 \quad \text{Eq. 5.7}$$

$$E_c \text{ (V) [anti-EpCAM/TiO}_2\text{/MoS}_2\text{@GO/ITO]} = 0.140 \text{ (V)} - 0.054 \text{ (V)} \times \log [\text{scan rate (mV/s)}]; R^2 = 0.994 \quad \text{Eq. 5.8}$$

The values of  $\alpha$  are estimated as 0.89 for TiO<sub>2</sub>/MoS<sub>2</sub>@GO/ITO electrode and 0.87 for anti-EpCAM/TiO<sub>2</sub>/MoS<sub>2</sub>@GO/ITO electrode using the above equations and their plot. Further, the diffusion coefficient (D) has been calculated using the linear slope of the anodic peak currents on the square root scan rate (Eq. 5.3 and 5.4), and the Randle Sevcik equation [13]. The value of D calculated for TiO<sub>2</sub>/MoS<sub>2</sub>@GO/ITO and anti-EpCAM/TiO<sub>2</sub>/MoS<sub>2</sub>@GO/ITO electrode was found to be 81.09 x 10<sup>-12</sup> cm<sup>2</sup> s<sup>-1</sup> and 63.36 x 10<sup>-12</sup> cm<sup>2</sup> s<sup>-1</sup>, respectively.

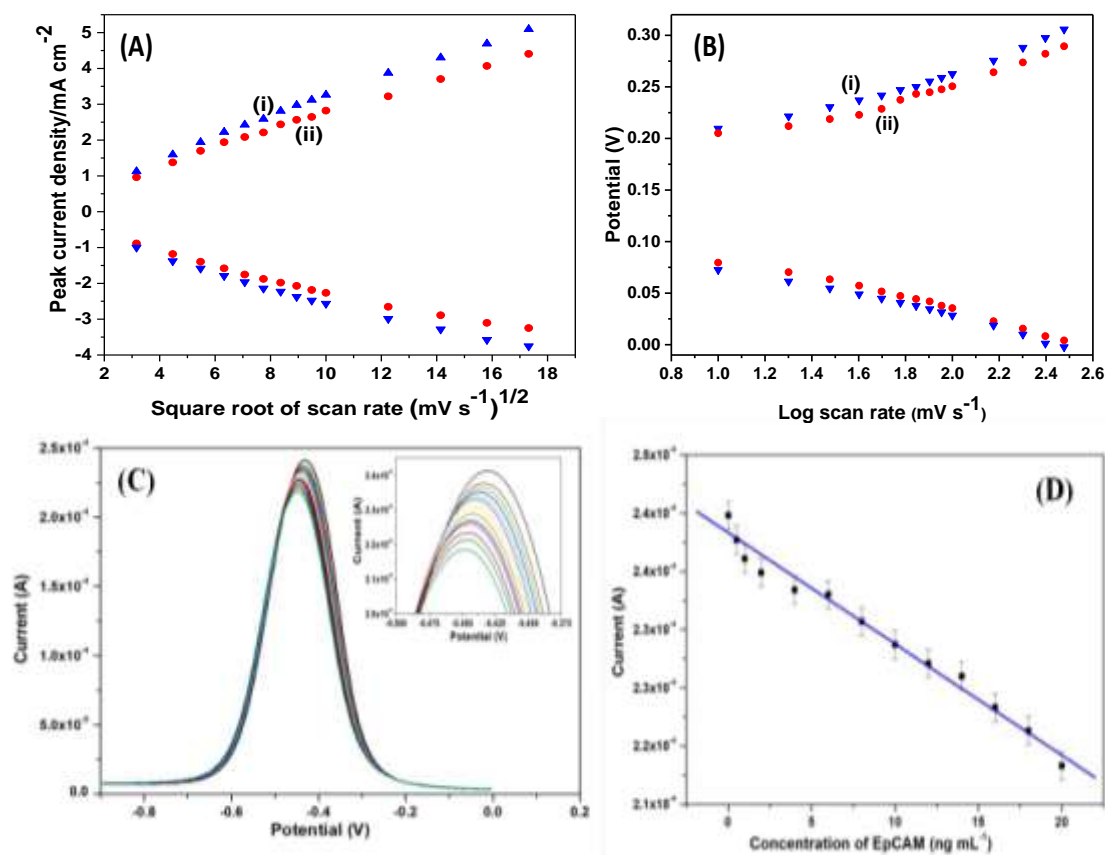


**Figure 5.4.** (A)  $I_{pa}$ ,  $I_{pc}$ , vs. square root of scan rate plot of (i)  $TiO_2/MoS_2@GO/ITO$  and (ii) anti-EpCAM/ $TiO_2/MoS_2@GO/ITO$  electrode (B) Plot of potential with log of scan rate for (i)  $TiO_2/MoS_2@GO/ITO$  and (ii) anti-EpCAM/ $TiO_2/MoS_2@GO/ITO$  electrode. (C) DPV studies response of the anti-EpCAM/ $TiO_2/MoS_2@GO/ITO$  electrode against EpCAM concentration; The magnified view of oxidation peak current is given in inset (D) Calibration plot between the current magnitudes and EpCAM concentration (0.0001-20 ng mL<sup>-1</sup>).

### 5.3.2.1 Electrochemical biosensing response of EpCAM using electrode

DPV technique was used to study the biosensing performance of fabricated anti-EpCAM/ $TiO_2/MoS_2@GO/ITO$  electrode towards EpCAM concentrations. In order to study the efficacy of modified electrodes towards EpCAM detection, the biosensing studies were carried out by incubating anti-EpCAM/ $TiO_2/MoS_2@GO/ITO$  electrode with different concentrations of EpCAM (0.0001–20 ng mL<sup>-1</sup>) and the data are shown in the **Fig. 5.4 (C)**. A continuous decrease has been observed in the anodic peak current when the anti-EpCAM/ $TiO_2/MoS_2@GO/ITO$  electrode was treated with EpCAM in an increasing order of concentration as seen in **Fig. 5.4. ©**. This decrease in current response may be attributed due to the interaction of EpCAM with anti-EpCAM resulting (antigen-antibody complex) in the formation of non conducting layer on the electrode surface which retards the electron transfer from bulk solution to electrode. The calibration plot [**Fig. 5.4. (D)**] between the magnitudes of current and concentration of EpCAM is electron which follows the below mentioned equation:

$$I_p = 2.38 (\mu A) - 95.6 (\mu A/ng/mL) \times \text{EpCAM concentration (ng/mL)} \quad \text{Eq. 5.9}$$

The LOD calculated for the fabricated biosensor has been found to be 0.00001 ng mL<sup>-1</sup>. The better conductivity, synergistic effects and topographic interactions at surface of fabricated electrode make it suitable for a better sensing platform.

### 5.3.3 Interference and shelf-life studies

The specific detection of EpCAM using fabricated electrode was carried out by incubating the anti-EpCAM/ $TiO_2/MoS_2@GO/ITO$  electrode with other interfering analytes, i.e., glucose, sodium chloride and immunoglobulin IG (IgG) separately and along with

EpCAM antigen.

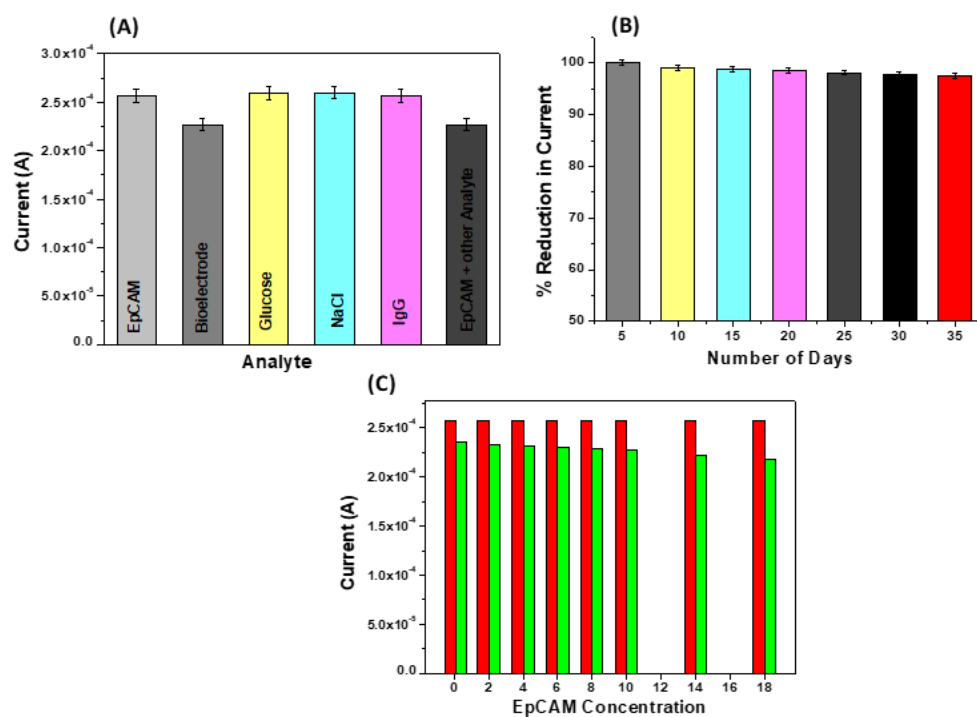


**Figure 5.5.** (A) Interference study of the fabricated biosensor (B) Bar graph showing the stability of the biosensors (C) Performance of the biosensor with different concentrations of EpCAM spiked serum samples

These analytes are supposed to be interfering agents that are found in human plasma. The bar graph [Fig. 5.5 (A)] clearly depicts the absence of false signal that could have been produced by using the interfering analytes other than EpCAM. The selectivity has also been confirmed, by validating the biosensor with the mixture of another analyte and EpCAM antigen. The fabricated biosensor was able to detect the cancer biomarker even in the presence of other analytes. The stability of biosensor was tested for 35 days and it was observed that the current response reduced to 97.5% which signifies an excellent stability of the fabricated electrode [Fig. 5.5 (B)].

### 5.3.4 Real sample analysis

The validation of the fabricated biosensor for detection of EpCAM in spiked serum sample has been carried out by incubating the anti-EpCAM/TiO<sub>2</sub>/MoS<sub>2</sub>@GO/ITO electrode with different concentrations of EpCAM. The electrochemical data clearly show the ability of biosensor to detect the EpCAM in serum samples and the results obtained were similar to

the response obtained with EpCAM inoculated in buffer with an RSD of 2.2-4.8 % [Fig. 5.5 (C)]. The results suggest that TiO<sub>2</sub>/MoS<sub>2</sub>@GO nanohybrid based biosensor is reliable for detecting the cancer biomarker in human serum samples.

#### 5.4 Conclusion

The work reported in this chapter deals with the facile synthesis of TiO<sub>2</sub>/MoS<sub>2</sub>@GO nanohybrid using hydrothermal method. Different ratio of the TiO<sub>2</sub> nanoparticles was grafted with MoS<sub>2</sub>@GO. It was observed that the increase of TiO<sub>2</sub> nanoparticles increases the electrochemical properties of the electrode. The biosensor fabricated using TiO<sub>2</sub>/MoS<sub>2</sub>@GO nanohybrid shows a good linearity in the concentration range of 0.0001–20 ng mL<sup>-1</sup> and an excellent limit of detection 0.00001 ng mL<sup>-1</sup>. This biosensor was found to be specific for the detection of the cancer biomarker and does not show any interference with other analytes. Validity of the biosensor with spiked serum samples also shows its applicability for point-of-care diagnostics.

## References

- [1] F.A. Harraz, M. Faisal, A.A. Ismail, S.A. Al-Sayari, A.E. Al-Salami, A. Al-Hajry, M.S. Al-Assiri, TiO<sub>2</sub>/reduced graphene oxide nanocomposite as efficient ascorbic acid amperometric sensor, *Journal of Electroanalytical Chemistry*, 832 (2019) 225-232.
- [2] Y. Gao, Y. Zheng, J. Chai, J. Tian, T. Jing, D. Zhang, J. Cheng, H. Peng, B. Liu, G. Zheng, Highly effective photocatalytic performance of {001}-TiO<sub>2</sub>/MoS<sub>2</sub>/RGO hybrid heterostructures for the reduction of Rh B, *RSC advances*, 9 (2019) 15033-15041.
- [3] M. Mirza-Aghayan, M. Saeedi, R. Boukherroub, An efficient CuO/rGO/TiO<sub>2</sub> photocatalyst for the synthesis of benzopyranopyrimidine compounds under visible light irradiation, *New Journal of Chemistry*, 46 (2022) 3817-3830.
- [4] Y. Zhang, H. Qi, L. Zhang, Y. Wang, L. Zhong, Y. Zheng, X. Wen, X. Zhang, J. Xue, A RGO aerogel/TiO<sub>2</sub>/MoS<sub>2</sub> composite photocatalyst for the removal of organic dyes by the cooperative action of adsorption and photocatalysis, *Environmental Science and Pollution Research*, 29 (2022) 8980-8995.
- [5] J. Ma, M. Xing, L. Yin, K. San Hui, K.N. Hui, Porous hierarchical TiO<sub>2</sub>/MoS<sub>2</sub>/RGO nanoflowers as anode material for sodium ion batteries with high capacity and stability, *Applied Surface Science*, 536 (2021) 147735.
- [6] S. Nipane, S.-W. Lee, G. Gokavi, A. Kadam, In situ one pot synthesis of nanoscale TiO<sub>2</sub>-anchored reduced graphene oxide (RGO) for improved photodegradation of 5-fluorouracil drug, *Journal of Materials Science: Materials in Electronics*, 29 (2018).
- [7] M. Mandal, D. Ghosh, S. Kalra, C. Das, High Performance Supercapacitor Electrode Material based on Flower like MoS<sub>2</sub>/Reduced Graphene Oxide Nanocomposite, *International Journal of Latest Research in Science And Technology (IJLRST)*, 3 (2014).
- [8] G. Thien, A. Pandikumar, H. Ming, H. Lim, Highly Exposed {001} Facets of Titanium Dioxide Modified with Reduced Graphene Oxide for Dopamine Sensing, *Scientific reports*, 4 (2014) 5044.
- [9] J. Chen, Y. Xia, J. Yang, B. Chen, Fabrication of monolayer MoS<sub>2</sub>/rGO hybrids with



excellent tribological performances through a surfactant-assisted hydrothermal route, *Applied Physics A*, 124 (2018).

[10] P. Benjwal, M. Kumar, P. Chamoli, K. Kar, Enhanced photocatalytic degradation of methylene blue and adsorption of arsenic(III) by reduced graphene oxide (rGO)–metal oxide (TiO<sub>2</sub>/Fe<sub>3</sub>O<sub>4</sub>) based nanocomposites, *RSC Advances*, 5 (2015) 73249-73260.

[11] R. Vinoth, I. Patil, A. Pandikumar, B. Kakade, Nay, H. Ming, D. Dionysiou, B. Neppolian, Synergistically Enhanced Electrocatalytic Performance of an N-Doped Graphene Quantum Dot-Decorated 3D MoS<sub>2</sub> –Graphene Nanohybrid for Oxygen Reduction Reaction, *ACS Omega*, 1 (2016) 971–980.

[12] C.M. Pandey, G. Sumana, I. Tiwari, Copper oxide assisted cysteine hierarchical structures for immunosensor application, *Applied Physics Letters*, 105 (2014) 103706.

[13] O. Jalil, C.M. Pandey, D. Kumar, Highly sensitive electrochemical detection of cancer biomarker based on anti-EpCAM conjugated molybdenum disulfide grafted reduced graphene oxide nanohybrid, *Bioelectrochemistry (Amsterdam, Netherlands)*, 138 (2021) 107733.

## CHAPTER 6

### *Conclusion and future prospects*

---

This work reveals the structural, morphological, electrical, compositional, and electrochemical properties of graphene oxide and its nanocomposites with nanomaterials such as TiO<sub>2</sub> and MoS<sub>2</sub> as well as their utility for biosensing application. A highly sensitive label-free electrochemical biosensor has been fabricated for the detection of cancer biomarkers. The environment friendly route was used for the synthesis of the nanocomposite, which shows the excellent electrochemical properties, selectivity, and performs as an appropriate sensing layer. The fabricated rGO@TiO<sub>2</sub>/ITO electrode shows improved electron transfer kinetics with an electron transfer rate constant of  $1.93 \times 10^{-7}$  cm s<sup>-1</sup> and a diffusion coefficient of  $1.07 \times 10^{-12}$  cm<sup>2</sup> s<sup>-1</sup>. Further, the rGO@TiO<sub>2</sub>/ITO electrodes were used to covalently immobilize monoclonal EpCAM antibodies. Label-free detection of EpCAM cancer biomarker by this fabricated biosensor is achieved by differential pulse voltammetry with high sensitivity ( $3.24 \mu\text{A mL ng}^{-1} \text{cm}^{-2}$ ) and low detection limit ( $0.006 \text{ ng mL}^{-1}$ ). The GO-based substrate provides an excellent platform for the growth of TiO<sub>2</sub> nanoparticles. With covalent conjugation of anti-EpCAM antibody, a broader detection range ( $0.01\text{-}60 \text{ ng mL}^{-1}$ ) and a much lower detection limit ( $0.0065 \text{ ng mL}^{-1}$ ) towards EpCAM cancer biomarker detection have been achieved. This fabricated biosensor was validated with spiked serum samples and shows the promising results for efficiently detecting cancer biomarkers in the serum sample. Thus, the fabricated platform has the potential to be used for the sensitive and selective detection of EpCAM, which would be transformative in the diagnosis of cancer.

A facile and environment-friendly route for synthesizing MoS<sub>2</sub>@rGO nanohybrid, using the amino acid assisted solution-phase method has been reported in this chapter. The MoS<sub>2</sub>@rGO nanohybrid exhibits improved electrochemical performance when it has been electrophoretically deposited onto the indium tin oxide (ITO) coated glass substrate.

Further, epithelial cell adhesion molecule antibodies (anti-EpCAM) specific to cancer biomarker have been covalently immobilized on the MoS<sub>2</sub>@rGO/ITO electrodes for label-free detection of EpCAM. Electrochemical results confirm that anti-EpCAM/MoS<sub>2</sub>@rGO/ITO based biosensor can detect EpCAM in the concentration range of 0.001-20 ng mL<sup>-1</sup> with a detection limit of 44.22 fg mL<sup>-1</sup> (S/N=3). An excellent analytical performance of the biosensor is attributed due to the efficient immobilization of antibodies on the MoS<sub>2</sub>@rGO surface, which results in high specificity for EpCAM. The fabricated biosensor shows the good selectivity, reproducibility, and stability. The successful detection of EpCAM antigen in spiked samples like human saliva, serum and urine makes this platform an alternative method for early screening of cancer biomarkers. This work also reports the facile synthesis of TiO<sub>2</sub>/MoS<sub>2</sub>@GO nanohybrid using hydrothermal method. Different ratio of the TiO<sub>2</sub> nanoparticles were grafted with MoS<sub>2</sub>@GO and the result shows that with an increase in the TiO<sub>2</sub> nanoparticles there was an improvement in the electrochemical properties of the electrode. Further, biosensor fabricated using TiO<sub>2</sub>/MoS<sub>2</sub>@GO nanohybrid shows a good linearity in the concentration range (0.0001–20 ng mL<sup>-1</sup>) and excellent limit of detection 0.00001 ng mL<sup>-1</sup>. The biosensor was found to be specific for the detection of the cancer biomarker and does not show any interference with other analytes. Validity of the biosensor with spiked serum samples shows its applicability for the point-of-care diagnostics.

## **Future prospects**

- Despite the fact that cancer biomarkers have been successfully used for the detection of Anti-EpCAM, there is still a great deal of uncertainty surrounding their usage because no single cancer biomarker meets every criterion for an ideal cancer biomarker. As a result, it is necessary to create a multiple markers detection technique using a combination of existing and novel cancer biomarkers that can aid in proper and early clinical decision-making.
- The idea of combining different nanostructures with graphene oxide can be used to create very sensitive devices for applications in early diagnosis.
- Future advancements in biosensor technology could focus on sensitivity and selectivity improvement and the detection of various cancer biomarkers with the support of electrochemistry.

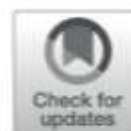
## **PUBLICATIONS**

- O. Jalil, C.M. Pandey, D. Kumar, Electrochemical biosensor for the epithelial cancer biomarker EpCAM based on reduced graphene oxide modified with nanostructured titanium dioxide, *Microchimica Acta*, 187 (2020) 275.
- O. Jalil, C.M. Pandey, D. Kumar, Highly sensitive electrochemical detection of cancer biomarker based on anti-EpCAM conjugated molybdenum disulfide grafted reduced graphene oxide nanohybrid, *Bioelectrochemistry*, 138 (2021) 107733.
- G. Paul, S. Verma, O. Jalil, D. Thakur, C.M. Pandey, D. Kumar, PEDOT: PSS- grafted graphene oxide-titanium dioxide nanohybrid-based conducting paper for glucose detection, *Polymers for Advanced Technologies*, 32 (2021) 1774-1782.
- O. Jalil, C.M. Pandey, D. Kumar, Electrochemical biosensor based on TiO<sub>2</sub>/rGO/MoS<sub>2</sub> nanohybrid for ultrasensitive detection of cancer biomarkers. (Manuscript under preparation)

## **CONFERENCE/SEMINAR/WORKSHOP ATTENDED**

- Presented Poster at the National Conference on Nano-Structured Materials and Device Technologies (NCNSMDT–2018), during December 21-22, 2018. Organized by Faculty of Science Aggarwal College Ballabgarh, Faridabad (Haryana), India.
- Presented Poster at an International Conference on Advanced Materials (ICAM- 2019) organized by Centre for Nanoscience and Nanotechnology, Jamia Millia Islamia, New Delhi, India on March 6-7, 2019.
- Presented Poster at an International Conference on Atomic, Molecular, Optical, and Nano Physics with Applications (CAMNP-2019), held at Delhi Technological University, Delhi, India, during 18 – 20 December 2019.
- Presented Poster in the virtual International Conference on Surface Chemistry SUCH-2020, 27-28 august 2020 in the Department of Chemistry Annamalai university (a state university-accredited with a grade by NAAC) Annamalai Nagar-608002, Tamil Nadu, India.
- An active participant in the National Workshop titled "ADVANCES IN POLYMER MATERIALS" Under the DST-PURSE program and organized by the Department of Applied Chemistry, ZHCET, AMU, Aligarh (September 21st-22nd, 2013).
- Participated successfully in the National seminar on "Applications of Radio-isotopes and Radiation in Food Technology, Environment & Healthcare Industries" organized by the Global Centre for Nuclear Energy Partnership (GCNEP), Department of Atomic Energy (DAE) & Shri Ram Institute for Industrial Research (August 8th-9th 2016).
- Participated in National Workshop on "Intellectual Property Rights: Culmination of Research" supported by: Ministry of Micro, Small and Medium Enterprises, (Government of India) at Bhaskaracharya College of Applied Sciences (September 23rd – 24th, 2016).

- Attended 2nd International Conference on "Advanced Production & Industrial Engineering (ICAPIE-2017)" organized by Centre for Advance Production & Industrial Engineering (CAPIER) Delhi Technological University held in New Delhi, India (October 6th -7th 2017).
- Completed One-day joint workshop on Patent Filing Procedure jointly conducted by Rajiv Gandhi National Institute of Intellectual Property Management (RGNIPM), Nagpur, and Delhi Technological University, Delhi on 28 May 2018.
- Attended 1st International Conference on New Frontiers in Engineering Science, and Technology (NFEST-2018), held in Delhi Technological University, New Delhi, India from January 8th – 12th, 2018.
- Worked as an organizing team member in the TEQIP-III sponsored one-week faculty development program on “Polymer Analysis and Applications: Current Scenario” from 4th-8th June 2018, organized by the Department of Applied Chemistry, Delhi Technological University, Delhi.
- Participated in the Young Scientist Conference organized from 22-12-2020 to 24-12-2020 as a part of India International Science Festival-2020 organized by the Ministry of Science and Technology, Ministry of Earth Sciences, and Ministry of Health and Family welfare, Govt. of India in collaboration with Vijnana Bharati (VIBHA). The event has been coordinated by the Council of Scientific and Industrial Research (CSIR) on the virtual platform.
- One-Day virtual Workshop on “Accelerators/Incubation - Opportunities for Students & Faculties - Early-Stage Entrepreneurs”, recommended by the Institute Innovation Council (IIC) of DTU as per the mandate of Innovation Cell, Ministry of Education (MoE) GOI, organized by Department of Applied Chemistry, Delhi Technological University on Saturday, 19th June 2021.



# Electrochemical biosensor for the epithelial cancer biomarker EpCAM based on reduced graphene oxide modified with nanostructured titanium dioxide

Owais Jalil<sup>1</sup> · Chandra Mouli Pandey<sup>1</sup> · Devendra Kumar<sup>1</sup>

Received: 30 August 2019 / Accepted: 23 March 2020  
© Springer-Verlag GmbH Austria, part of Springer Nature 2020

## Abstract

An electrochemical immunosensor has been fabricated for the early determination of epithelial cell adhesion molecules (EpCAM, tumor biomarker) antigen using reduced graphene oxide (rGO) modified with nanostructured titanium dioxide (TiO<sub>2</sub>). The hydrothermally synthesized rGO@TiO<sub>2</sub> nanocomposite has been electrophoretically deposited on indium tin oxide (ITO) coated glass substrate, and the deposition was confirmed using various spectroscopic, microscopic, and electrochemical techniques. The fabricated rGO@TiO<sub>2</sub>/ITO electrode shows improved electron transfer kinetics with an electron transfer rate constant of  $1.93 \times 10^{-7} \text{ cm}^2 \text{ s}^{-1}$ . Furthermore, the rGO@TiO<sub>2</sub>/ITO electrodes were used for the covalent immobilization of monoclonal EpCAM antibodies. Electrochemical determination of the EpCAM cancer biomarker is achieved using differential pulse voltammetry by scanning the potential from  $-0.4$  to  $0.8$  V with an amplitude of  $50$  mV. The rGO@TiO<sub>2</sub>-based biosensor shows high sensitivity ( $3.24 \mu\text{A mL}^{-1} \text{ ng}^{-1} \text{ cm}^2$ ), wide detection range ( $0.01 \text{ ng mL}^{-1}$  to  $60 \text{ ng mL}^{-1}$ ), and low detection limit ( $0.0065 \text{ ng mL}^{-1}$ ,  $S/N = 3$ ). The fabricated biosensor is highly stable and regenerable and has been successfully applied to the determination of EpCAM in spiked human serum samples.

**Keywords** Biomarker · Cancer · Epithelial cell adhesion molecules · Electrophoretic deposition · Electrochemical biosensor · Graphene oxide · Titanium dioxide

## Introduction

The early detection and quantification of cancer biomarkers provide an efficient pathway to observe tumor progression and relate them to specific cancer types. In this context, epithelial cell adhesion molecules (EpCAM) have been considered a prognostic tumor biomarker for cancer diagnosis [1–3]. EpCAM is a glycosylated transmembrane protein,

which is expressed on the surface of circulating tumor cells, and the overexpression of EpCAM has generally been found in the carcinomas of the breast, stomach, colon, rectum, prostate, biliary tract, pancreas, etc. [4, 5]. For the detection of EpCAM, techniques such as cytometry, enzyme-linked immunosorbent assays, and polymerase chain reaction have been widely used [6, 7]. However, these methods are usually expensive, complicated, time-consuming, and even require highly skilled human resources [8]. Therefore, there is an urgency for the development of an effective alternative method for early, sensitive, affordable, and reliable determination of EpCAM.

Some immunosensor based on electrochemical [9], fluorescence [10, 11], surface plasmon resonance [12], and colorimetric techniques have been reported for the detection of EpCAM. Shiddiky et al. have successfully functionalized 2D graphene oxide (GO) nanosheets with quantum dots and antibodies and demonstrated that these bionanoconjugates are highly sensitive and specific for the electrochemical detection of EpCAM [13]. A

**Electronic supplementary material** The online version of this article (<https://doi.org/10.1007/s00604-020-04233-7>) contains supplementary material, which is available to authorized users.

✉ Chandra Mouli Pandey  
cmp.npl@gmail.com

✉ Devendra Kumar  
dkumar@dce.ac.in

<sup>1</sup> Department of Applied Chemistry, Delhi Technological University, Delhi 110042, India



# Highly sensitive electrochemical detection of cancer biomarker based on anti-EpCAM conjugated molybdenum disulfide grafted reduced graphene oxide nano hybrid



Owais Jalil, Chandra Mouli Pandey\*, Devendra Kumar\*

Department of Applied Chemistry, Delhi Technological University, Delhi 110042, India

## ARTICLE INFO

### Article history:

Received 24 August 2020

Received in revised form 19 November 2020

Accepted 23 December 2020

Available online 29 December 2020

### Keywords:

Cancer

Biomarkers

Biosensor

EpCAM

Graphene oxide

Molybdenum disulfide

## ABSTRACT

An ultrasensitive, electrochemical biosensor has been fabricated by utilizing molybdenum disulfide ( $\text{MoS}_2$ ) grafted reduced graphene oxide ( $\text{MoS}_2/\text{rGO}$ ) nano hybrid as a sensing platform. Biomolecular-assisted synthetic method was adopted to synthesize  $\text{MoS}_2/\text{rGO}$  nano hybrid, where L-cys was used to reduce GO. The  $\text{MoS}_2/\text{rGO}$  nano hybrid exhibits improved electrochemical performance when it has been electrochemically deposited onto the indium tin oxide (ITO) coated glass substrate. Further, epithelial cell adhesion molecule antibodies (anti-EpCAM) specific to cancer biomarker has been covalently immobilized on the  $\text{MoS}_2/\text{rGO}/\text{ITO}$  electrodes for label-free detection of EpCAM. Electrochemical results confirm that anti-EpCAM/ $\text{MoS}_2/\text{rGO}/\text{ITO}$  based biosensor can detect EpCAM in the concentration range of 0.001–20  $\text{ng mL}^{-1}$  with a detection limit of 44.22  $\text{fg mL}^{-1}$  (S/N = 3). The biosensor's excellent analytical performance has been attributed to the efficient immobilization of EpCAM antibodies on the  $\text{MoS}_2/\text{rGO}$  surface, which results in high specificity for EpCAM antigen. The fabricated biosensor showed good selectivity, reproducibility, and stability. The successful detection of EpCAM antigen in spiked samples (human saliva, serum and urine) makes this platform an alternative method for early screening of cancer biomarker.

© 2020 Elsevier B.V. All rights reserved.

## 1. Introduction

Cancer has been considered the second-largest disease with a high mortality rate where patient's survival is uncertain because of limited cancer diagnostic techniques [1]. The traditional techniques for detecting cancer mainly rely on the cell morphology detected using staining and microscopy, which is not sensitive enough [2]. However, accurate and effective methods are urgently needed for the successful detection and clinical diagnosis of cancer [3]. Recently, biomarker-based cancer diagnosis has shown significant potential in detecting and monitoring cancer patients [4]. These immunoassays are being widely used for sensitive and selective detection of cancer biomarkers, although they are time-consuming, expensive, and not sensitive enough to detect a lower concentration of biomarkers in the initial stages of cancer [5]. Moreover, being manual, these methods for biomarker detection are slow and consume expensive reagents in every assay [6]. Therefore, there is an urgency for sensitive and rapid technology,

which will help in providing better healthcare by increasing sensitivity and reducing the waiting time.

Nowadays, biosensors play a critical role in determining cancer biomarkers as they are portable, easy to use, and can analyze in real-time [7,8]. Among the various biomarkers, epithelial cell adhesion molecule (EpCAM; glycosylated membrane protein) has been considered a prognostic tumor biomarker expressed in most cancer cells [9,10]. EpCAM has been found to be strongly expressed in carcinomas of various origins, such as breast, colorectal, lung, prostate, etc., and have critical clinical significance in the early monitoring of tumors, mainly in determining the different stages of cancer [11,12]. The detection of EpCAM using fluorescent, surface Plasmon resonance, and calorimetric based biosensor has shown promising results [6,13–15]. Moreover, a cost-effective biosensor with higher sensitivity and selectivity for timely and reliable detection of EpCAM is still required. In this context, electrochemical biosensors have shown huge potential because of its accuracy, ease of preparation, smooth operation, high sensing ability and selectivity [16]. However, when the concentration of the target molecule is very low, the signal generated during the biochemical reaction is too weak and may not be detected by the conventional electrode [17,18]. So, electrode material should be designed in such a way

\* Corresponding authors.

E-mail addresses: [cmpanp@gmail.com](mailto:cmpanp@gmail.com) (C.M. Pandey), [dkumar@dcu.ac.in](mailto:dkumar@dcu.ac.in) (D. Kumar).



# Owais Jalil

(+91) 7417927817

✉ info.owaisjalil@gmail.com

PhD

📍 2/15-C, Anona House, Civil Lines,  
Aligarh, UP-202001

## Research Interest

Synthesis and characterization of Polymers and nanomaterials, Graphene based nanocomposite, electrochemical applications of these nanomaterials/nanocomposites in detection & quantification of various novel biomarker and fabrication of biosensor.

## Academic Qualification

- 2017 Phd Course Work in Applied chemistry and Polymer Technology from Delhi Technological University, Delhi, India (SGPA: 7.85)
- 2015 M.Sc in Polymer Science & Technology from Aligarh Muslim University, Aligarh, India (70 %)
- 2013 B.Sc (Hons.) Industrial Chemistry from Aligarh Muslim University, Aligarh, India (67 %)
- 2009 Intermediate from Aligarh Muslim University, Aligarh, India (61 %)

## Instrumental Skills

Potentiostat/Galvanostat: Cyclic Voltammetry (CV), Differential Voltammetry(DPV), Electrochemical Impedance Spectroscopy(EIS), X-Ray Diffraction (XRD), FT-IR, UV-VIS spectrophotometer, Electrical measurement setup (Four Probe), Differential Scanning Calorimetry (DSC), Thermogravimetric Analysis (TGA).

## Project Undertaken

M.Sc. (Polymer Science) project work at Department of Applied Chemistry, (ZHCET) AMU Aligarh on the topic of "Synthesis and Characterization of PANI-Epoxy composites".

## Awards

- 4th Research Excellence award presented for excellence in research to published a paper "Electrochemical biosensor for the epithelial cancer biomarker EpCAM based on reduced graphene oxide modified with nanostructured titanium dioxide" by Delhi Technological University on February 15, 2021.
- 5th Research Excellence award presented for excellence in research to published a paper "Highly sensitive electrochemical detection of cancer biomarker based on anti-EpCAM conjugated molybdenum disulfide grafted reduced graphene oxide nanohybrid" by Delhi Technological University on March 3, 2022.

## Research Publications

- Published -3, Paper presented in Conference-4

## Personal Details

**Fathers Name :** Mr. Jalil Ahmad Khan

**Date of Birth :** 16 August 1990

**Nationality :** Indian

**Sex/Marital Status :** Male/Unmarried

**Languages Known :** English, Hindi and Urdu